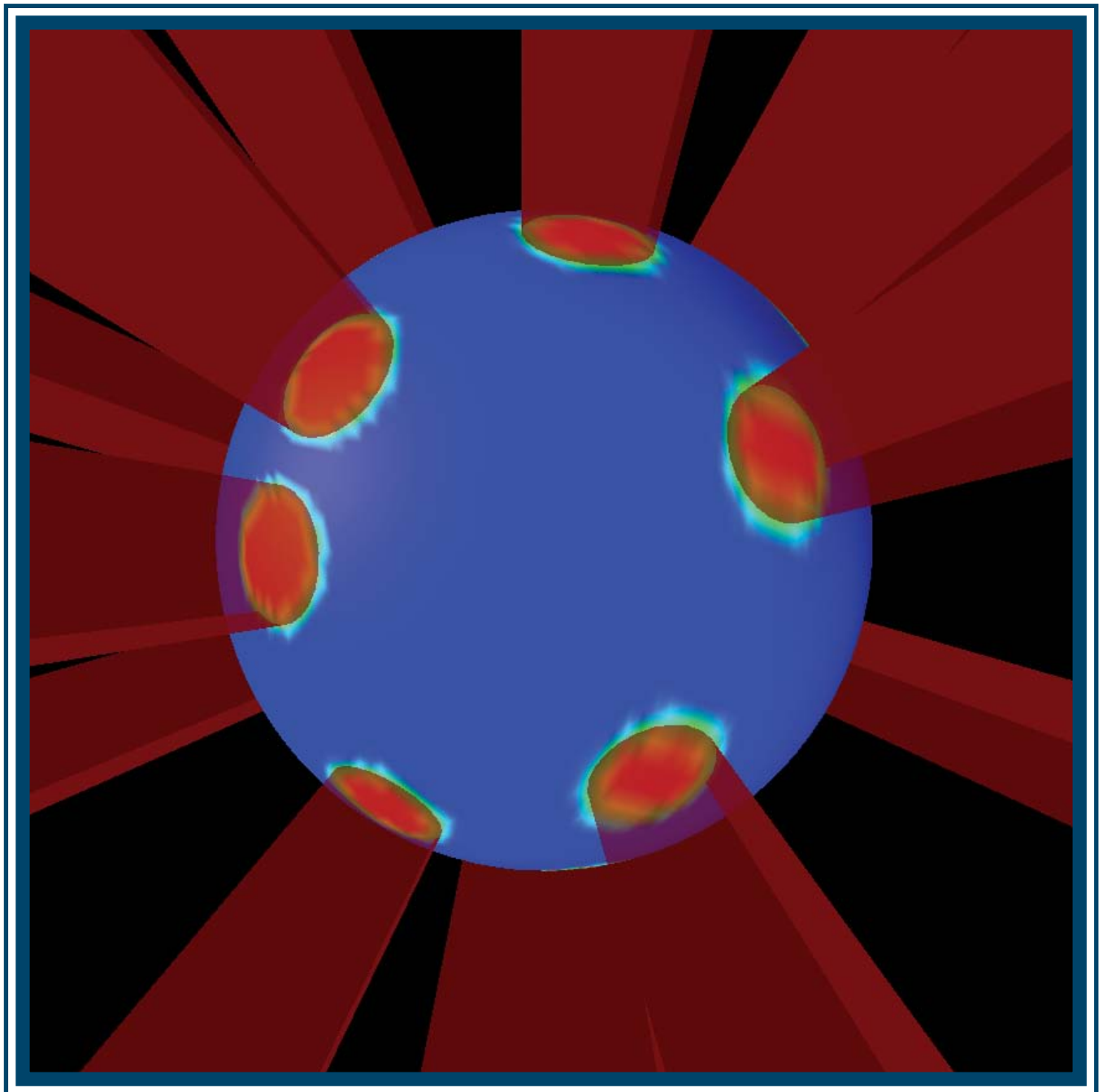


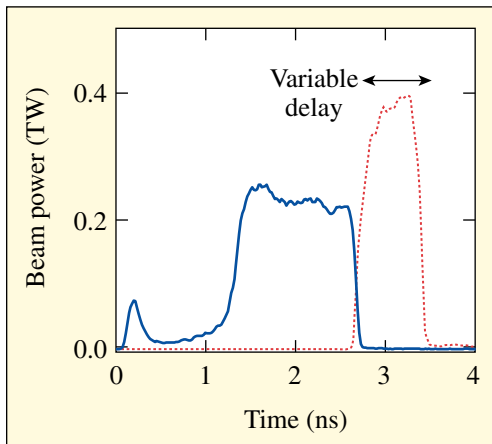
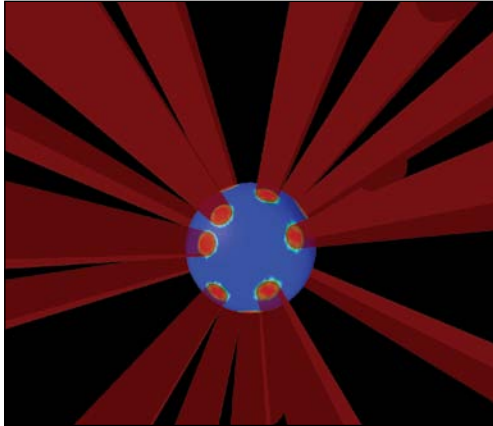
LLE Review

Quarterly Report



About the Cover:

The VISRAD simulation of a shock-ignition experiment seen on the cover of this review shows the placement of 20 OMEGA laser beams tightly focused on the critical surface of an imploding spherical target to launch an ignitor shock wave. In the shock-



ignition concept for inertial confinement fusion, fuel assembly and ignition are separated. In the fuel-assembly step, targets are first imploded by lasers with a pulse designed to compress the target to a large areal-density core. In the ignition step, a strong shock wave is launched into the target using high-intensity laser light. This ignitor shock heats the hot spot and ignites the target. The final result is ignition with a lower energy threshold or significantly larger gains for the same laser energy than the conventional direct-drive-ignition concept.

For the experiments described in the feature article (see **Shock-Ignition Experiments on OMEGA at NIF-Relevant Intensities**, p. 117), the ignitor spike beams were tightly focused on the compressed core to achieve intensities of up to 1×10^{16} W/cm² to drive a strong shock. Good coupling of the shock-beam energy was observed in these experiments, leading up to an $\sim 20\times$ increase in neutron yield. The intense ignitor beams were also observed to produce fast electrons via laser-plasma interaction, which, due to their short mean free path, should be stopped in the target shell, further augmenting the ignitor shock. The enhanced neutron yields and beneficial effect of fast electrons are very encouraging for the shock-ignition concept and research into it continues at LLE.

The drive for these shock-ignition experiments was provided by 40 OMEGA laser beams using the low-adiabat ($\alpha \sim 1.5$) shaped pulse (solid line) with an ~ 100 -ps picket preceding a shaped main-drive portion, which consisted of a low-power foot and a moderate-power plateau with a total duration of 2.6 ns. The delayed 20 ignitor beams used an ~ 600 -ps FWHM square pulse shape (dashed curve) and were tightly focused on the shell without polarization smoothing or phase plates to maximize intensity.

This report was prepared as an account of work conducted by the Laboratory for Laser Energetics and sponsored by New York State Energy Research and Development Authority, the University of Rochester, the U.S. Department of Energy, and other agencies. Neither the above named sponsors, nor any of their employees, makes any warranty, expressed or implied, or assumes any legal liability or responsibility for the accuracy, completeness, or usefulness of any information, apparatus, product, or process disclosed, or represents that its use would not infringe privately owned rights. Reference herein to any specific commercial product, process, or service by trade name, mark, manufacturer, or otherwise, does not necessarily constitute or

imply its endorsement, recommendation, or favoring by the United States Government or any agency thereof or any other sponsor. Results reported in the LLE Review should not be taken as necessarily final results as they represent active research. The views and opinions of authors expressed herein do not necessarily state or reflect those of any of the above sponsoring entities.

The work described in this volume includes current research at the Laboratory for Laser Energetics, which is supported by New York State Energy Research and Development Authority, the University of Rochester, the U.S. Department of Energy Office of Inertial Confinement Fusion under Cooperative Agreement No. DE-FC52-08NA28302, and other agencies.

For questions or comments, contact Dana H. Edgell, Editor, Laboratory for Laser Energetics, 250 East River Road, Rochester, NY 14623-1299, (585) 275-0277.

Worldwide-Web Home Page: <http://www.lle.rochester.edu/>
(Color online)

Printed in the United States of America

Available from

National Technical Information Services

U.S. Department of Commerce

5285 Port Royal Road

Springfield, VA 22161

Price codes: Printed Copy A04

Microfiche A01

LLE Review

Quarterly Report



Contents

In Brief	iii
Shock-Ignition Experiments on OMEGA at NIF-Relevant Intensities	117
Laser-Driven Magnetic-Flux Compression in High-Energy-Density Plasmas.....	123
Lorentz Mapping of Magnetic Fields in Hot, Dense Plasmas	129
Characterization and Optimization of Yb-Doped Photonic-Crystal Fiber Rod Amplifiers Using Spatially Resolved Spectral Interferometry	134
Optical Differentiation and Multimillijoule ~150-ps Pulse Generation in a Regenerative Amplifier with a Temperature-Tuned Intracavity Volume Bragg Grating.....	141
Slow Crack Growth During Radiative Cooling of LHG8 and BK7 Plates	145
Finite Element Simulation of Metal–Semiconductor–Metal Photoconductor	154
Publications and Conference Presentations	

In Brief

This volume of the LLE Review, covering April–June 2009, features “Shock-Ignition Experiments on OMEGA at NIF-Relevant Intensities” by W. Theobald, R. Betti, K. S. Anderson, O. V. Gotchev, D. D. Meyerhofer, C. Ren, A. A. Solodov, and C. Stoeckl (LLE and Fusion Science Center for Extreme States of Matter and Fast Ignition Physics); V. A. Smalyuk, J. A. Delettrez, V. Yu. Glebov, F. J. Marshall, J. F. Myatt, T. C. Sangster, W. Seka, and B. Yaakobi (LLE); and J. A. Frenje and R. D. Petrasso (Plasma Science and Fusion Center, MIT). In this article (p. 117), the authors discuss shock-ignition experiments that have been performed with peak shock-generating laser intensities of $\sim 1 \times 10^{16}$ W/cm². Shock ignition is a two-step inertial confinement fusion (ICF) concept in which a strong shock wave is launched at the end of the laser drive pulse to ignite the compressed core, relaxing the driver requirements and promising high gains. In the experiments described in this article, room-temperature plastic shells filled with D₂ gas were compressed on a low adiabat by 40 beams of the 60-beam OMEGA Laser System. The remaining 20 beams were delayed and tightly focused onto the target to drive a strong shock into the compressed core. Good coupling of the shock-beam energy was observed in these experiments, leading up to an $\sim 20\times$ increase in neutron yield. The authors observed significant stimulated Raman backscattering of laser energy; however, fast-electron measurements showed a relatively cold energy distribution. These fast electrons are actually beneficial for shock ignition since they have short mean-free-paths and are stopped in the thin outer layer of the imploding target, augmenting the strong hydrodynamic shock.

Additional highlights of recent research presented in this issue include the following:

- O. V. Gotchev, D. D. Meyerhofer, O. Polomarov, and R. Betti (LLE and Fusion Science Center for Extreme States of Matter and Fast Ignition Physics); P. Y. Chang and J. P. Knauer (LLE); J. A. Frenje, C. K. Li, M. J.-E. Manuel, R. D. Petrasso, and F. H. Séguin (Plasma Science and Fusion Center, MIT); and J. R. Rygg (LLNL) discuss laser-driven magnetic-flux compression in high-energy-density plasma experiments (p. 123). The authors demonstrated for the first time magnetic-field compression to many tens of megagauss (MG) in cylindrical implosions of inertial confinement fusion targets. The very high magnetic-flux compression was achieved using the ablative pressure of the OMEGA laser to drive a cylindrical shell at high-implosion velocity, trapping and compressing an embedded external field to tens of MG, high enough to magnetize the hot-spot plasma. The magnetic fields in the compressed core were probed via proton deflectometry using the fusion products from an imploding D³He target. Line-averaged magnetic fields between 30 and 40 MG were observed.
- R. D. Petrasso, C. K. Li, F. H. Séguin, J. R. Rygg, and J. A. Frenje (Plasma Science and Fusion Center, MIT); R. Betti, J. P. Knauer, and D. D. Meyerhofer (LLE); and P. A. Amendt, D. H. Froula, O. L. Landen, P. K. Patel, J. S. Ross, and R. P. J. Town (LLNL) show that monoenergetic proton radiography combined with Lorentz mapping can be used to uniquely detect and discriminate magnetic and electric fields (p. 129). Protons were used to image two identical expanding plasma bubbles, formed on opposite sides of a 5- μ m-thick plastic (CH) foil by two 1-ns-long laser-interaction beams. The second bubble reverses the sign of any magnetic fields relative to the first bubble by the protons, while keeping the electric fields the same. Field-induced deflections of the monoenergetic 14.9-MeV probe protons passing through the two bubbles, measured quantitatively with proton radiography, were combined with Lorentz mapping to provide separate measurements of magnetic and electric fields. The authors’ results provided absolute identification and measurement of a toroidal magnetic field around each bubble and determined that any electric field component parallel to the foil was below measurement uncertainties.

- J. Bromage, C. Dorrer, J. R. Marciante, and J. D. Zuegel use a spatially resolved spectral interferometry technique, known as S^2 imaging, to measure for the first time, higher-order-mode content of a large-mode-area amplifier at full power (p. 134). The technique was adapted for the short-fiber amplifier at full power and revealed a small amount of a co-polarized LP_{11} mode. This mode's power, relative to the fundamental LP_{01} mode, depends on the alignment of the input signal at injection to the rod amplifier, and ranged from -18 dB, for optimized alignment, to -13 dB when the injection alignment was offset along the LP_{11} axis by $15 \mu\text{m}$ (30% of the $55\text{-}\mu\text{m}$ mode-field diameter). The increase in LP_{11} contributed to the M^2 degradation that was measured when the injection was misaligned.
- A. V. Okishev demonstrates for the first time optical differentiation in a regenerative amplifier (RA) with temperature-tuned volume Bragg grating (VBG) as an intracavity spectral filter (p. 141). The VBG as a spectrally selective resonator mirror works as an optical differentiator when the VBG reflection peak is detuned from the central laser wavelength. A simple, reliable laser system that produces multi-millijoule ~ 150 -ps pulses without mode-locking, using an RA with VBG as an optical differentiator, is described.
- J. C. Lambropoulos and H. Liu (Department of Mechanical Engineering, U. of Rochester) discuss crack growth in brittle glass plates using known finite element modeling to determine the maximum allowable initial crack size in plates undergoing radiative cooling (p. 145). In these simulations both BK7 borosilicate crown and LHG8 phosphate glass were slowly cooled in vacuum from 200°C down to room temperature. The authors used finite elements and incorporated available experimental results on crack growth in BK7 and LHG8. Numerical simulation showed that the heaviest stressed locations were the midpoints of the plate's long edges, where any crack growth was likely to originate. This article outlines a procedure to estimate the deepest-allowable surface flaw to prevent fracture. Fracture is analyzed in terms of strength, fracture toughness, or slow crack growth. Merits of these approaches are discussed, and an extensive comparison of cracking in BK7 versus LHG8 is presented.
- G. Guarino, W. R. Donaldson, and R. Sobolewski (LLE); M. Mikulics and M. Marso (Institute of Bio- and Nanosystems, Research Centre of Jülich); and P. Kordoš (Institute of Electrical Engineering, Slovak Academy of Sciences) apply finite element analysis to ultrafast photoconductive switches of the metal–semiconductor–metal (MSM) type to explain why MSM devices with alloyed electrodes show improved photoresponse efficiency compared to devices with surface contact electrodes (p. 154). The alloyed device, despite having a somewhat larger capacitance, has an active region of lower resistance with a more-uniform and deeper-penetrating electric field and carrier transport current. The authors use the latter to explain the experimentally observed faster response of the alloyed device in terms of the equivalent lumped parameters. They also use the model to predict improved responsivity, based on electrode spacing and antireflective coating.

Dana H. Edgell
Editor

Shock-Ignition Experiments on OMEGA at NIF-Relevant Intensities

Shock ignition is a two-step inertial confinement fusion (ICF) concept in which a strong shock wave is launched at the end of the laser pulse to ignite the compressed core of a low-velocity implosion.¹ Two-step processes separate fuel assembly and ignition, relaxing driver requirements and promising high gains.^{1,2} The gain of an ICF implosion can be significantly enhanced by launching a strong spherically convergent shock at the end of the compression (or assembly) pulse.^{1,3–5} Another advanced-ignition concept is fast ignition,⁶ which relies on a high-intensity, short-pulse laser generating an energetic beam of particles to trigger ignition. Shock ignition relies on highly shaped laser pulses, which might be produced by the pulse-shaping capabilities of the already operating National Ignition Facility (NIF).⁷ Recent two-dimensional (2-D) simulations⁴ have described shock-ignition designs with as low as 250 kJ of total laser energy. Proof-of-principle experiments^{1,8} could be carried out at the NIF. The spherically convergent shock wave (ignitor shock) propagates through the shell during the coasting phase of the implosion and enhances the hot-spot compression, significantly improving the ignition conditions. The ignitor shock is launched at the end of the laser pulse by a spike with intensity in the range of 3×10^{15} to 10^{16} W/cm². This shock collides with the return shock near the inner shell surface. The return shock is the shock wave driven by the hot-spot pressure and propagating outward through the shell. After the ignitor and return shock collide, a third shock wave, resulting from the collision, propagates inward, leading to further compression of the hot spot. The final fuel assembly develops a centrally peaked pressure profile. Such non-isobaric assemblies exhibit a lower ignition threshold than standard isobaric assemblies. This mechanism is effective only in thick-shell implosions, where the ignitor shock wave significantly increases in strength as it propagates through the converging shell.¹

Previous shock-ignition experiments⁹ on OMEGA¹⁰ studied fuel assembly with 60-beam symmetric implosions with 18 kJ of UV laser energy using 40- μ m-thick, 0.9-mm-diam, warm surrogate plastic shells filled with deuterium gas of various pressures. The shock wave was launched by a spike in the

laser power at the end of the pulse. The maximum intensity on target during the late power spike was $\sim 8 \times 10^{14}$ W/cm², and the resulting shock wave was relatively weak (the shock pressure was only 20 Mbar higher than the unshocked plasma pressure). These experiments showed a significant improvement in the performance of low-adiabat, low-velocity implosions compared to conventional implosions without a late spike in the laser pulse shape and showed that shock-wave timing is crucial to optimizing implosion performance. This shock-ignition campaign achieved the highest areal density ever measured on OMEGA (a neutron-rate-averaged areal density of 0.22 g/cm² and a peak areal density exceeding 0.3 g/cm²) and neutron yields 4 \times larger than in conventional implosions.⁹

Parametric plasma instabilities¹¹ such as stimulated Brillouin scattering (SBS), stimulated Raman scattering (SRS), and two-plasmon-decay (TPD) instability are of concern in an ignition target design with spike-pulse intensities in the range of 10^{15} to 10^{16} W/cm² and full width at half maximum (FWHM) pulse durations of several hundred picoseconds. The instabilities increase the back-reflection of the laser light from the target, degrading the laser energy coupling to the capsule. They increase the fraction of the laser energy transferred to suprathermal electrons, a potential source of preheat that reduces the final core compression. In contrast to conventional hot-spot ignition, low-energy hot electrons generated during the power spike may have a positive effect on the implosions for shock ignition. The areal density increases rapidly during the final stages of the implosion. If the range of the hot electrons generated during the intensity spike is less than the shell thickness, they are stopped in the shell and augment the hydrodynamically driven shock wave. The effect of hot electrons on a shock-ignition target¹² was modeled in 1-D for a marginal igniting target using a multigroup diffusion model¹³ for the hot electrons. The ignition window for a shock-launching time is considerably wider when the effects of moderate-energy hot electrons (a NIF-scale target can efficiently stop up to 150-keV electrons) are included, showing that hot electrons can indeed be beneficial for the shock-ignition scheme as long as their range is shorter than the shell's thickness.

This work provides the first measurements of parametric instability and preheat for conditions relevant for shock ignition (spherical target, long density scale length, and intensities above 2×10^{15} W/cm²). Important physics issues including the hot-electron energy content, the hot-electron temperature, and laser backscattering for various intensities and time delays between fuel assembly and shock generation are studied. Switching from a 60-beam to a 40- plus 20-beam configuration with dual pulse shapes makes it possible to use tightly focused beams that generate a stronger shock compared to previous experiments. The data will help validate the shock-ignition target concepts at ignition-relevant intensities of $\sim 5 \times 10^{15}$ W/cm².

Figure 119.1 shows a schematic of the experiments described here. The compression pulse consisted of a shaped, low-adiabat laser pulse using 40 beams of OMEGA.¹⁰ A late shock was driven by the remaining 20 beams that were delayed and focused on the compressed core to achieve intensities at the critical surface ranging from $\sim 2 \times 10^{15}$ to $\sim 8 \times 10^{15}$ W/cm². Plasma instabilities in density regions of up to quarter-critical density led to the generation of energetic electrons. Some of the fast electrons streamed into the hot core, heating it.

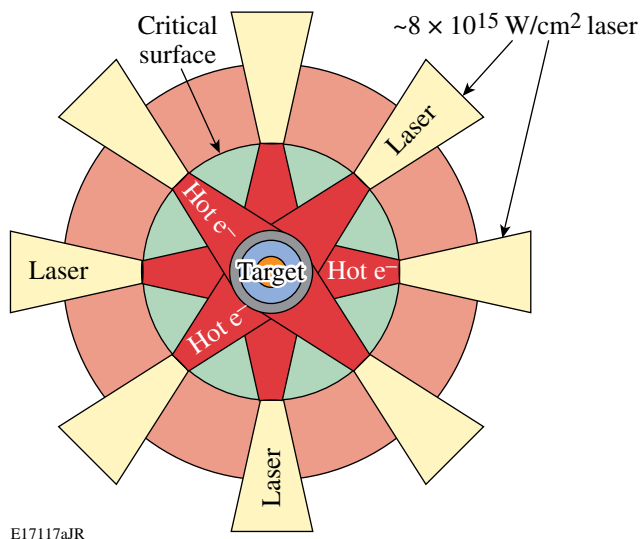
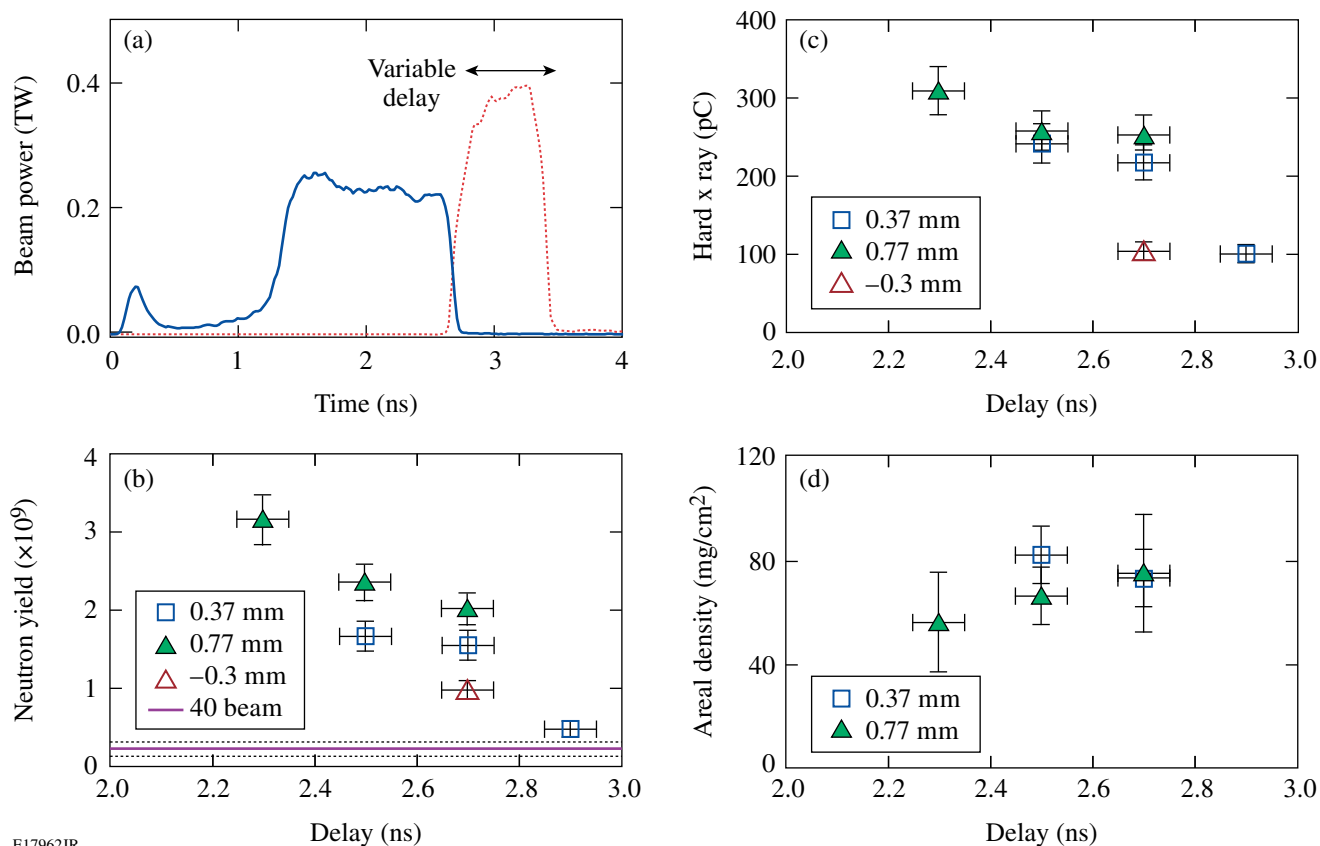


Figure 119.1 Schematic of the setup for studying laser–plasma interactions and preheating at high laser intensities relevant to shock ignition. Forty of the OMEGA laser beams implode the capsule at low intensities. Twenty delayed beams are tightly focused onto the critical density surface, where plasma instabilities lead to the generation of energetic electrons. Some of them will stream into the dense core.

The targets were 36- μ m-thick, 430- μ m-outer-radius, deuterated plastic (CD) shells coated outside with a 0.1- μ m layer of aluminum and filled with D₂ gas with a pressure of ~ 30 atm. The capsules were imploded by 40 beams using a low-adiabat ($\alpha \sim 1.5$) pulse shape¹⁴ at ~ 13.6 kJ of UV laser energy. The adiabat α is defined as the ratio of the plasma pressure to the Fermi pressure of a degenerate electron gas.¹⁵ The solid curve in Fig. 119.2(a) shows the drive pulse shape comprising an ~ 100 -ps (FWHM) Gaussian picket pulse preceding a shaped main-drive portion that consisted of a low-power foot and a moderate-power plateau with a total duration of 2.6 ns. The 351-nm-wavelength laser light of the 40 beams was smoothed with polarization smoothing¹⁶ and distributed phase plates.¹⁷ The delayed 20 beams (~ 4.6 kJ) that used an ~ 600 -ps FWHM square pulse shape (dotted curve) were tightly focused on the shell without polarization smoothing or phase plates.

The experimental observables were the neutron yield,¹⁸ the backscattered laser energy,¹⁹ the hard x-ray signal,²⁰ and the neutron-rate–averaged areal density.²¹ The laser light reflected back from the imploded capsule was measured from two beam ports [a shock-beam port (#25) and a drive-beam port (#30)], which were equipped with a full-aperture backscatter station (FABS).¹⁹ The FABS measured the light backscattered into the final focusing lens aperture by down-collimating the reflection off the front surface of a full-aperture, uncoated glass wedge in the beamline onto a diagnostics table. Time-resolved spectra were recorded by two streaked spectrometers covering the wavelength ranges of 351 ± 3 nm for SBS and 450 to 700 nm for SRS. The total backscattered energy in either of these spectral ranges was measured by calorimeters with an uncertainty of $\pm 10\%$. The hard x-ray (HXR) signals (with photon energies > 20 keV) were measured by the HXR detector with four channels measuring x rays > 20 , > 40 , > 60 , and > 80 keV, respectively.²⁰ Areal densities (ρR) were inferred from secondary proton spectra.²¹

The delay time defined by the onset of the high-intensity beams with respect to the start of the drive pulse was varied from 2.3 to 2.9 ns. The effect on neutron and HXR yield is shown in Figs. 119.2(b) and 119.2(c) and on ρR in Fig. 119.2(d). The different symbols represent various focus conditions, where the number refers to the focus position in vacuum with respect to the shell’s center. A negative number means that the focus is in front of the target toward the laser. The neutron yield increases by a factor of ~ 7 from 5×10^8 to $\sim 3.5 \times 10^9$ for the shortest time delay. Two reference implusions with only the 40 drive beams produced neutron yields of 1.4×10^8 and 3.7×10^8 ; the solid line in Fig. 119.2(b) represents the average of both yields. The HXR yield’s dependence on delay time is



E17962JR

Figure 119.2

(a) Drive-pulse shape (solid) and high-intensity pulse (dotted), [(b)–(d)] measured neutron yield, hard x-ray yield, and neutron-rate-averaged areal density, respectively. The different symbols represent various focus positions with respect to the critical-density surface. The solid line in (b) is the average yield for 40-beam implosions and the dotted lines represent the error range. The 40-beam implosions produced no measurable HXR signal, and neutron yields were too low to obtain a ρR measurement.

similar. Figure 119.2(c) shows that signals measured by the >40 -keV channel increase with shorter delay.

The HXR signal provided information on the hot-electron energy and temperature. Based on a calibration²² of the hard x-ray detector, $\sim 16 \pm 6\%$ (~ 310 -pC HXR signal) to $\sim 5 \pm 2\%$ of the shock-beam energy was converted into hot electrons. The conversion efficiency was highest for short delays when there was a partial overlap between the drive and shock pulses [Fig. 119.2(c)]. The hot-electron temperature was determined by fitting estimated values from the convolution of an exponentially decaying hard x-ray spectrum with the sensitivity of the different channels of the HXR detector to the measured four channels.²³ The inferred temperature was ~ 40 to 45 keV for all the shots, independent of laser intensity.

The implosions were nonuniform with a dominant $\ell = 2$ mode, which was caused by an unbalanced target illumina-

tion. The power imbalance was $\sim 10.6\%$, given as the root-mean-square variation of the laser power on target. A typical value for a 60-beam symmetrical illumination on a spherical target is $\sim 2\%$ power imbalance.²⁴ The nonuniformity of the implosion is clearly seen in the x-ray pinhole camera image [Fig. 119.3(a)], which shows a strongly perturbed core with a 40-beam implosion. The core distortion was reduced when the 20 delayed, tightly focused beams were coupled into the target [Fig. 119.3(b)]. Figure 119.3(c) shows pinhole images from a symmetric implosion with a low-adiabat pulse shape and a similar target at a higher laser energy. Figures 119.2(b) and 119.2(c) show that despite large target illumination nonuniformity, a significant amount of the high-intensity pulse energy was coupled into the capsule, producing up to $\sim 20\times$ more neutrons and a strong HXR signal. The correlation of increasing neutron yield with a higher HXR signal suggests that the increased yield was partially due to hot electrons coupled into the outer regions of the compressing target. The late shock

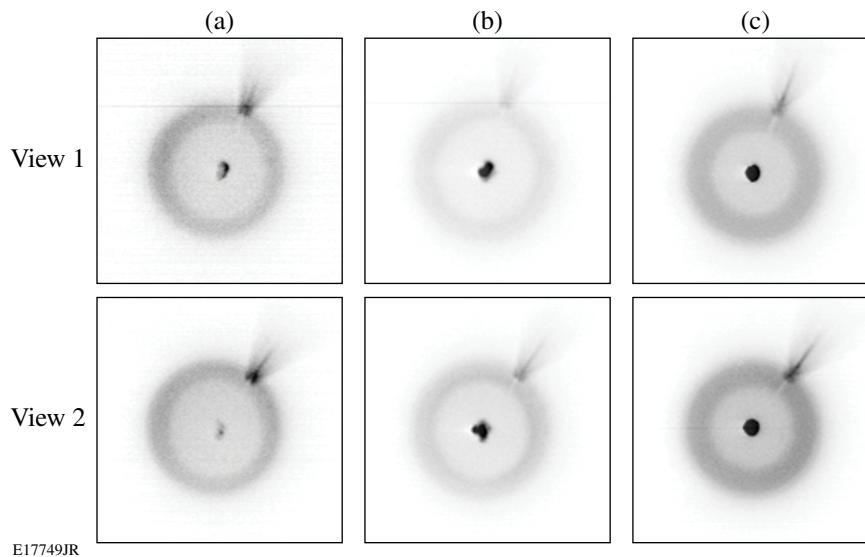


Figure 119.3

X-ray pinhole camera images from three different implosions. (a) Reference implosion with 40 drive beams, (b) 40- plus 20-beam implosion for a 0.77-mm focus position and a 2.3-ns time delay, (c) 60-beam uniform illumination. The feature at the upper right edge is due to the target stalk.

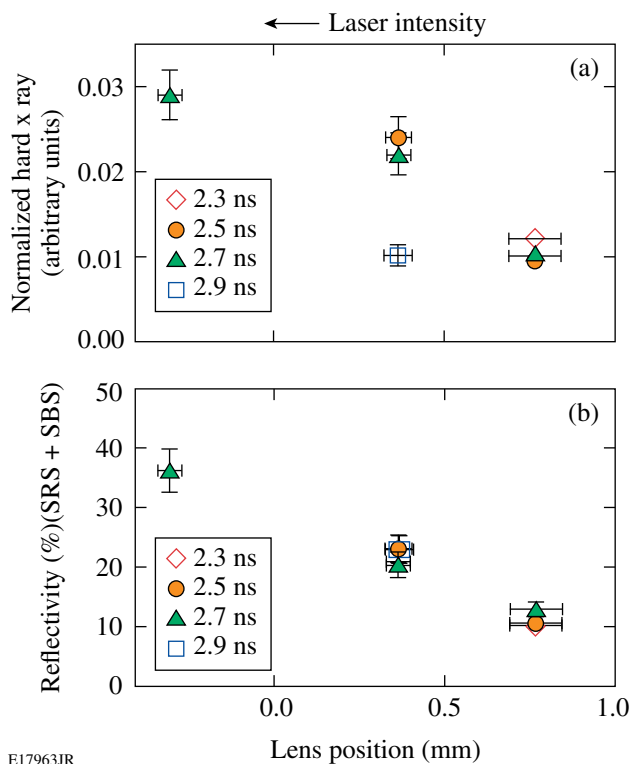
appears to be driven by a combination of the standard ablative and hot-electron drives.

The areal density does not change significantly with delay. The measured maximum ρR is 82 ± 11 mg/cm², which is the average of four lines of sight, and the error bar is the standard deviation. This is $\sim 30\%$ lower than the expected ~ 115 mg/cm², which is scaled down from the measured 130 ± 17 mg/cm² (Ref. 14) that was obtained with a more-uniform 60-beam implosion with the same fill pressure, the same adiabat, and an energy of 20 kJ and using the scaling of ρR with the laser energy to the power 1/3 (Ref. 14). For these shots, the standard deviation of the measured ρR varies from 15% to 35% of the mean ρR value, showing a large fluctuation of the areal density. The ρR degradation is most likely due to the strongly nonuniform implosion. Neutron yields from the 40-beam implosions were too low to obtain a ρR measurement.

The plasma reflectivity and HXR production from hot electrons were measured for various laser intensities. This was achieved through an intensity scan by shifting the focus of the 20 shock-driving beams relative to the shell's center. The nominal (in vacuum) laser intensity is quoted for the location of the critical-density plasma surface calculated by a 1-D hydrodynamic simulation.¹³ The distance from the critical density to the capsule center was ~ 0.3 mm at 2.7 ns. For the lens position at -0.3 mm, the 20 beams were tightly focused on the critical-

density location. The focus diameter of the 20 shock beams is estimated with ~ 80 μ m, which gives a best-focus intensity up to $\sim 8 \times 10^{15}$ W/cm² for the shock beams in vacuum. The foci of the 20 shock beams did not overlap at the critical density for all lens positions used. No overlapped-beam effects²⁰ were expected and the HXR signal was dominated by single-beam interaction with the target.

Figure 119.4(a) shows the measured hard x-ray signal normalized to the estimated laser focus area versus lens position. The x-ray signal and consequently the hot-electron production increase with laser intensity presumably because of a larger growth in laser-plasma instabilities such as SRS and TPD, the primary sources of hot electrons.²⁰ Figure 119.4(b) shows the measured amount of laser backscatter energy of one shock beam (25) versus laser intensity. It increases from $\sim 10\%$ at $\sim 2 \times 10^{15}$ W/cm² to $\sim 36\%$ at $\sim 8 \times 10^{15}$ W/cm². The contribution from the SRS signal increases moderately from $\sim 7\%$ to 12%, while the SRS signal grows by almost a factor of ~ 5 from 5% to 24% and dominates the backscattering energy at the highest intensity. The simultaneously measured back-reflection through a neighboring drive-beam port (30) remained constant at the level of the implosions without the 20 shock beams for all beam delays and lens positions. This shows that the light from the shock beams was scattered back in a narrow cone and did not spill over into adjacent ports. No measurable signal of the 3/2 harmonic of the laser wavelength was measured for all inten-



E17963JR

Figure 119.4

Measured (a) hard x-ray signal normalized to nominal beam focus area and (b) backscattered light versus lens focus position with respect to the shell's center. The laser intensity at the critical density is highest for the negative lens position corresponding to an intensity of $\sim 8 \times 10^{15}$ W/cm². The various symbols represent different time delays.

sities. The half-harmonic signal decreased by more than two orders of magnitude with higher intensities. At the maximum intensity, the half-harmonic signal was below the detection threshold, indicating no significant contribution of TPD to the hot-electron production. These experiments measured higher backscattering levels than other experiments at comparable laser intensities but different plasma conditions.²⁵ Measurements of parametric instabilities for indirect-drive-relevant ignition-plasma conditions with millimeter-density scale length and 15% critical-density targets report backscatter at 5×10^{15} W/cm² of up to 10%.²⁵ The absorbed energy rather than the backscattered light is the key issue. If 36% of the laser light is backscattered and 64% is absorbed, it represents a higher absorption fraction than the prediction of collisional absorption at these intensities ($\sim 40\%$ to 50%). Because of the highly nonuniform plasma conditions and nonuniform illumination during the shock spike, the measurement of the scattered light through a few lines of sight cannot be used to infer the total absorbed fraction. In the pessimistic case where the predicted

absorbed energy is reduced by the backscattered fraction, this can be remedied by an increase in spike power.

In conclusion, shock-ignition laser-plasma experiments in spherical geometry have been performed with nominal laser intensities of up to $\sim 8 \times 10^{15}$ W/cm². This was achieved by low-adiabat compression of warm plastic shells filled with D₂ gas by 40 beams and tightly focusing 20 beams on the compressed core. The additional 20 high-intensity beams enhanced the neutron yields by up to a factor of ~ 20 , indicating a good coupling of the shock-beam energy to the core. A significant amount of backscattered laser energy from the high-intensity beams of up to 36% was measured at the highest laser intensity and about 20% at $\sim 5 \times 10^{15}$ W/cm². At high intensities, the back-reflection was dominated by SRS with some contribution from SBS but no significant contribution from TPD. About 10% of the high-intensity beam energy was converted into hot electrons. A hot-electron-energy distribution was generated with temperatures between ~ 40 and 45 keV, independent of laser intensity. This is beneficial for shock ignition since these electrons are stopped in a thin outer layer of the imploding target, augmenting the strong hydrodynamic shock. The reduction in driver energy caused by backscattering losses might be compensated by increasing the incident laser energy without the danger of preheating the target.

ACKNOWLEDGMENT

This work was supported by the U.S. Department of Energy Office of Inertial Confinement Fusion under Cooperative Agreement No. DE-FC52-08NA28302, the OFES Fusion Science Center grant No. DE-FC02-04ER54789, the OFES ACE FI grant No. DE-FG02-05ER54839, the University of Rochester, and the New York State Energy Research and Development Authority. The support of DOE does not constitute an endorsement by DOE of the views expressed in this article.

REFERENCES

1. R. Betti, C. D. Zhou, K. S. Anderson, L. J. Perkins, W. Theobald, and A. A. Solodov, *Phys. Rev. Lett.* **98**, 155001 (2007).
2. R. L. McCrory, D. D. Meyerhofer, R. Betti, R. S. Craxton, J. A. Delettrez, D. H. Edgell, V. Yu Glebov, V. N. Goncharov, D. R. Harding, D. W. Jacobs-Perkins, J. P. Knauer, F. J. Marshall, P. W. McKenty, P. B. Radha, S. P. Regan, T. C. Sangster, W. Seka, R. W. Short, S. Skupsky, V. A. Smalyuk, J. M. Soures, C. Stoeckl, B. Yaakobi, D. Shvarts, J. A. Frenje, C. K. Li, R. D. Petrasso, and F. H. Séguin, *Phys. Plasmas* **15**, 055503 (2008).
3. R. Betti and C. Zhou, *Phys. Plasmas* **12**, 110702 (2005).
4. X. Ribeyre *et al.*, *Plasma Phys. Control. Fusion* **50**, 025007 (2008).
5. A. J. Schmitt, J. W. Bates, S. P. Obenschain, S. T. Zalesak, D. E. Fyfe, and R. Betti, *Fusion Sci. Technol.* **56**, 377 (2009).

6. M. Tabak *et al.*, Phys. Plasmas **1**, 1626 (1994).
7. E. I. Moses, J. Phys., Conf. Ser. **112**, 012003 (2008).
8. L. J. Perkins, R. Betti, K. N. LaFortune, and W. H. Williams, Phys. Rev. Lett. **103**, 045004 (2009).
9. W. Theobald, R. Betti, C. Stoeckl, K. S. Anderson, J. A. Delettrez, V. Yu. Glebov, V. N. Goncharov, F. J. Marshall, D. N. Maywar, R. L. McCrory, D. D. Meyerhofer, P. B. Radha, T. C. Sangster, W. Seka, D. Shvarts, V. A. Smalyuk, A. A. Solodov, B. Yaakobi, C. D. Zhou, J. A. Frenje, C. K. Li, F. H. Séguin, R. D. Petrasso, and L. J. Perkins, Phys. Plasmas **15**, 056306 (2008).
10. T. R. Boehly, D. L. Brown, R. S. Craxton, R. L. Keck, J. P. Knauer, J. H. Kelly, T. J. Kessler, S. A. Kumpan, S. J. Loucks, S. A. Letzring, F. J. Marshall, R. L. McCrory, S. F. B. Morse, W. Seka, J. M. Soures, and C. P. Verdon, Opt. Commun. **133**, 495 (1997).
11. W. L. Kruer, *The Physics of Laser-Plasma Interactions*, Frontiers in Physics, Vol. 73, edited by D. Pines (Addison-Wesley, Redwood City, CA, 1988).
12. R. Betti, W. Theobald, C. D. Zhou, K. S. Anderson, P. W. McKenty, S. Skupsky, D. Shvarts, V. N. Goncharov, J. A. Delettrez, P. B. Radha, T. C. Sangster, C. Stoeckl, and D. D. Meyerhofer, J. Phys., Conf. Ser. **112**, 022024 (2008).
13. J. Delettrez, R. Epstein, M. C. Richardson, P. A. Jaanimagi, and B. L. Henke, Phys. Rev. A **36**, 3926 (1987); M. C. Richardson, P. W. McKenty, F. J. Marshall, C. P. Verdon, J. M. Soures, R. L. McCrory, O. Barnouin, R. S. Craxton, J. Delettrez, R. L. Hutchison, P. A. Jaanimagi, R. Keck, T. Kessler, H. Kim, S. A. Letzring, D. M. Roback, W. Seka, S. Skupsky, B. Yaakobi, S. M. Lane, and S. Prussin, in *Laser Interaction and Related Plasma Phenomena*, edited by H. Hora and G. H. Miley (Plenum Publishing, New York, 1986), Vol. 7, pp. 421–448.
14. C. D. Zhou, W. Theobald, R. Betti, P. B. Radha, V. A. Smalyuk, D. Shvarts, V. Yu. Glebov, C. Stoeckl, K. S. Anderson, D. D. Meyerhofer, T. C. Sangster, C. K. Li, R. D. Petrasso, J. A. Frenje, and F. H. Séguin, Phys. Rev. Lett. **98**, 025004 (2007).
15. C. D. Zhou and R. Betti, Phys. Plasmas **14**, 072703 (2007).
16. T. R. Boehly, V. A. Smalyuk, D. D. Meyerhofer, J. P. Knauer, D. K. Bradley, R. S. Craxton, M. J. Guardalben, S. Skupsky, and T. J. Kessler, J. Appl. Phys. **85**, 3444 (1999).
17. Y. Lin, T. J. Kessler, and G. N. Lawrence, Opt. Lett. **21**, 1703 (1996).
18. V. Yu. Glebov, D. D. Meyerhofer, C. Stoeckl, and J. D. Zuegel, Rev. Sci. Instrum. **72**, 824 (2001).
19. W. Seka, D. H. Edgell, J. P. Knauer, J. F. Myatt, A. V. Maximov, R. W. Short, T. C. Sangster, C. Stoeckl, R. E. Bahr, R. S. Craxton, J. A. Delettrez, V. N. Goncharov, I. V. Igumenshchev, and D. Shvarts, Phys. Plasmas **15**, 056312 (2008).
20. C. Stoeckl, R. E. Bahr, B. Yaakobi, W. Seka, S. P. Regan, R. S. Craxton, J. A. Delettrez, R. W. Short, J. Myatt, A. V. Maximov, and H. Baldis, Phys. Rev. Lett. **90**, 235002 (2003).
21. F. H. Séguin, J. A. Frenje, C. K. Li, D. G. Hicks, S. Kurebayashi, J. R. Rygg, B.-E. Schwartz, R. D. Petrasso, S. Roberts, J. M. Soures, D. D. Meyerhofer, T. C. Sangster, J. P. Knauer, C. Sorce, V. Yu. Glebov, C. Stoeckl, T. W. Phillips, R. J. Leeper, K. Fletcher, and S. Padalino, Rev. Sci. Instrum. **74**, 975 (2003).
22. V. A. Smalyuk, D. Shvarts, R. Betti, J. A. Delettrez, D. H. Edgell, V. Yu. Glebov, V. N. Goncharov, R. L. McCrory, D. D. Meyerhofer, P. B. Radha, S. P. Regan, T. C. Sangster, W. Seka, S. Skupsky, C. Stoeckl, B. Yaakobi, J. A. Frenje, C. K. Li, R. D. Petrasso, and F. H. Séguin, Phys. Rev. Lett. **100**, 185005 (2008).
23. C. Stoeckl, V. Yu. Glebov, D. D. Meyerhofer, W. Seka, B. Yaakobi, R. P. J. Town, and J. D. Zuegel, Rev. Sci. Instrum. **72**, 1197 (2001).
24. F. J. Marshall, J. A. Delettrez, R. Epstein, R. Forties, R. L. Keck, J. H. Kelly, P. W. McKenty, S. P. Regan, and L. J. Waxer, Phys. Plasmas **11**, 251 (2004).
25. J. D. Moody *et al.*, Phys. Rev. Lett. **86**, 2810 (2001).

Laser-Driven Magnetic-Flux Compression in High-Energy-Density Plasmas

In the magnetic-fusion-energy (MFE) concept, a strong magnetic field confines the plasma and reduces the electron thermal conduction to the vessel wall.¹ The magnetic pressure of typical ~ 0.1 -MG fields in MFE is higher than the total energy density of the plasma (with $\beta = 2\mu_0 p/B^2 < 1$). MFE plasmas are fully magnetized and characterized by a Hall parameter $\omega_{ce}\tau \gg 1$ since the modest gyrofrequency ω_{ce} is matched by long collision times τ . In contrast, typical inertial confinement fusion (ICF) plasmas have collision frequencies higher by 10 to 12 orders of magnitude because of their extreme density. In such systems, thermal conduction losses are a major factor in the energy balance of an implosion. While it may be more difficult, magnetizing the hot spot in ICF implosions can lead to improved gain in implosions of massive targets with relatively low implosion velocity² or to a reduction of the energy required for ignition. However, tens of MG are needed to achieve $\omega_{ce}\tau \sim 1$ in the hot spot of a typical direct-drive DT ignition target³ with a hot-spot density of ~ 30 g/cc and a temperature of ~ 7 keV. Such a field is higher than both the self-generated magnetic fields (see Ref. 4) and the external fields that can be generated by coils. Magnetic-flux compression⁵ is a viable path to generating tens-of-MG magnetic fields with adequate size.⁶ Magnetic-flux compression has been successfully achieved using the radial compression of a metallic liner driven by high explosives^{7,8} or by pulsed power. The latter approach has been pursued by the Z-pinch⁹ (including wire-array targets) and magnetized-target-fusion¹⁰ communities. The results from the first experiments on a new approach that provides very effective flux compression are reported here. The field is compressed by the ablative pressure exerted on an imploding ICF capsule by the driving laser.¹¹ This approach was proposed in the 1980s (Ref. 12) as a way to achieve record compressed fields with possible applications for fusion,¹³ but no laser experiments were performed. There are numerous advantages to this approach because the implosion velocity is high (a few 10^7 cm/s) and the hot plasma is an effective conductor that traps the embedded (seeded) initial magnetic field with minimal resistive diffusion. This approach can be used to magnetize high-energy-density plasmas for a number of applications ranging from controlled fusion to laboratory astrophysics.

Figure 119.5 describes a cylindrical implosion on OMEGA that used axial seed fields embedded in the target prior to compression.¹⁴ The target was a $20\text{-}\mu\text{m}$ -thick, 0.86-mm -diam CH cylindrical shell filled with D_2 gas. Some of the physical details of this concept are described in Refs. 11 and 15. The shock-heated and ionized D_2 fuel traps the seed magnetic field, which would otherwise diffuse much faster through the relatively cold (resistive) imploding shell. The seed field was provided by a Helmholtz-like double coil [Fig. 119.6(a); coil diameter and separation are both 4 mm], coaxial with the cylindrical target.¹⁶ The more-complicated min-B magnetic geometries used in magnetic-confinement-fusion (MCF) magnetic mirror experiments were not used here because the magnetohydrodynamic (MHD) instability must be considered more carefully. A portable capacitive discharge system¹⁶ delivers up to 80-kA current to the coils. The on-axis seed field was 50 to 90 kG at the target and 120 to 160 kG in the coil planes because of the coil separation chosen to avoid obscuring laser beams.

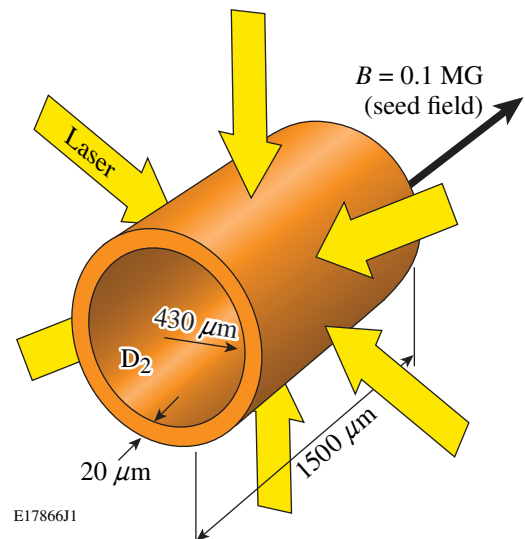


Figure 119.5
Laser-driven flux compression in a cylindrical target. A D_2 -gas fill inside the plastic shell traps the seed field after shock ionization.

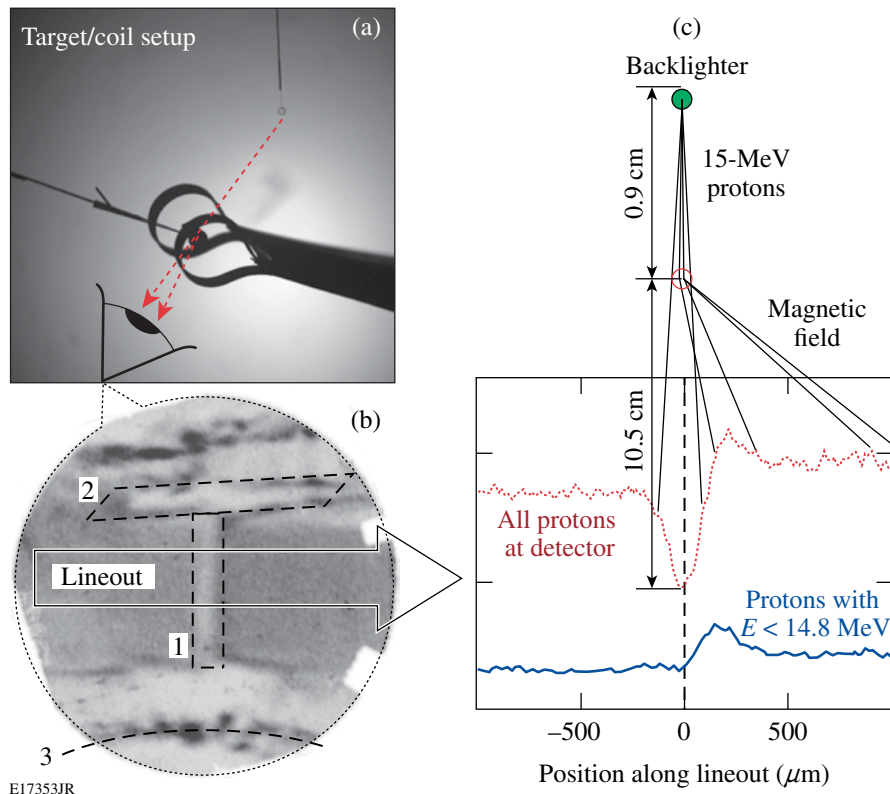


Figure 119.6

(a) Photo of the target/coil setup. (b) Proton density map for shot 51069. Darker areas represent higher fluence: (1) compressed core, (2) target plug, and (3) coil shadow. (c) Lineouts in two energy bands expose the deflected protons ($E_k < 14.8$ MeV, solid line; all protons, dotted line).

The compressed fields within the dense, optically thick ICF plasmas are difficult to measure. Proton deflectometry based on the method described in Refs. 17–19 is a viable diagnostic that has been implemented on OMEGA. A monoenergetic ($\Delta E/E \sim 0.03$), point-like (size/object distance ~ 0.01), time-gated (an ~ 150 -ps burst) proton source is provided by a glass sphere, filled with D^3He gas and driven in an exploding pusher scheme by several tightly focused OMEGA beams. The 14.7-MeV protons produced by the D^3He fusion reactions are accelerated to ~ 15.2 MeV by charging the backlighter target and recorded on a CR-39 nuclear track detector that provides both spatial and energy resolution (via the track diameter) of the particles incident on the surface.²⁰ The data [Fig. 119.6(b)] were generated as a convolution in space (source size, scattering at the object and detector) and time (finite duration) of the proton burst interacting with the field and target structure. None of the radial striations reported in Ref. 18 for spherical implosions was seen around the compressed core in these experiments, possibly because the target was imaged more than a nanosecond after the laser was

turned off. Turbulent field structure was present around the target plugs and stalk, but, while interesting, its morphology is beyond the scope of this article and will not be discussed.

A discrimination of tracks by energy (track diameter) was implemented to separate the core- (strong-field) traversing protons from the background, “free-space” particles that land in the same area of the detector. This is shown in Fig. 119.6(c), where the proton density map for shot 51069 [Fig. 119.6(b)] was used to construct two lineouts by taking a band of data and averaging over its width. The lower curve in Fig. 119.6(c) is from tracks with only energy $E_k < 14.8$ MeV caused by an additional slowdown through the magnetized target. It shows an asymmetric peak in the proton density caused by deflection in the target field. In contrast, the data from multiple “null” experiments performed to establish the particle-density pattern for implosions with no seed field retain central symmetry in the cross-core lineouts (Fig. 119.7); i.e., the low-energy peak lines up with the trough of the high-energy proton lineout.

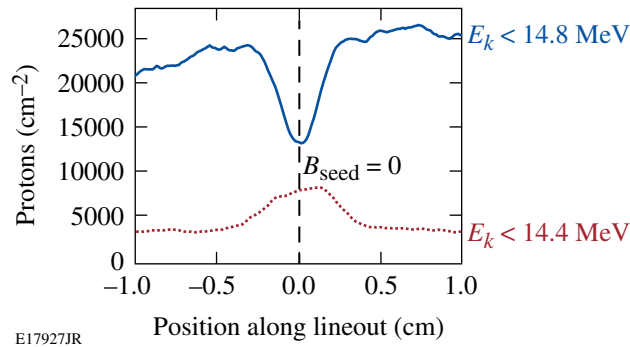


Figure 119.7

Cross-core lineouts from proton radiograph of shot 49693—an implosion with no external magnetic field—show that the core-traversing protons remained undeflected.

To predict and interpret the experimental data, a simulation package based on the Monte Carlo (MC) particle-transport framework Geant4 (Ref. 21) was developed. After including the field topology and material parameters predicted by the *LILAC*-MHD code²² for the time of proton probing, the particle-transport code computes the deflection pattern under the combined action of the field and scattering/energy-loss processes. A comparison (Fig. 119.8) of the MC simulation predictions (solid) and experimental data (dotted) for shot 49704, in which a compressed field of 13 MG was predicted by the hydrocode, shows very good agreement in both the total fluence and low-energy-band lineouts. In Fig. 119.8(b), only the protons that had an incident energy lower than 14.8 MeV were included. The target in shot 49704 had a seed field of 10 kG and was probed relatively early in the implosion. In later experiments, where the proton burst occurred at or near peak compression, the experimental lineouts at intermediate energies exhibited a double-deflection pattern with a second deflection peak farther from the center [Fig. 119.9(a), shot 51069]. This was first seen in Monte Carlo simulations [Fig. 119.9(b)] and was caused by an abrupt jump of the field in the small volume of the hot spot from much lower values in the shell (responsible for the first deflection). Early in time, at a low compressed field, these two peaks were essentially merged, as is the case with shot 49704. A comparison of the data for shot 51069, which had a 56-kG seed field, and the simulation shows good qualitative agreement, capturing the double-peak-deflection pattern. The protons that were slowed down the most (dashed–dotted curve) were those that crossed through the shell but not the hot spot, missing the peak field. From the 1.9-cm deflection of the secondary peak, one can estimate an average product $\langle R_B B_{\max} \rangle \approx 2\theta e/m_p v_p$ of 0.052 Tm, corresponding to an ~ 30 -MG hot-spot field for a predicted hot-spot size of 17 μm .

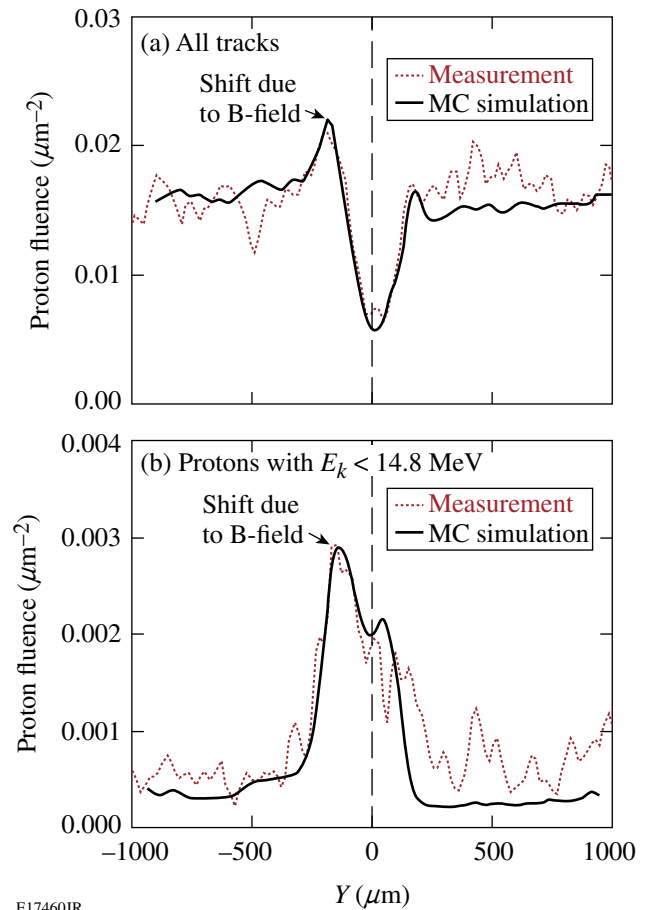
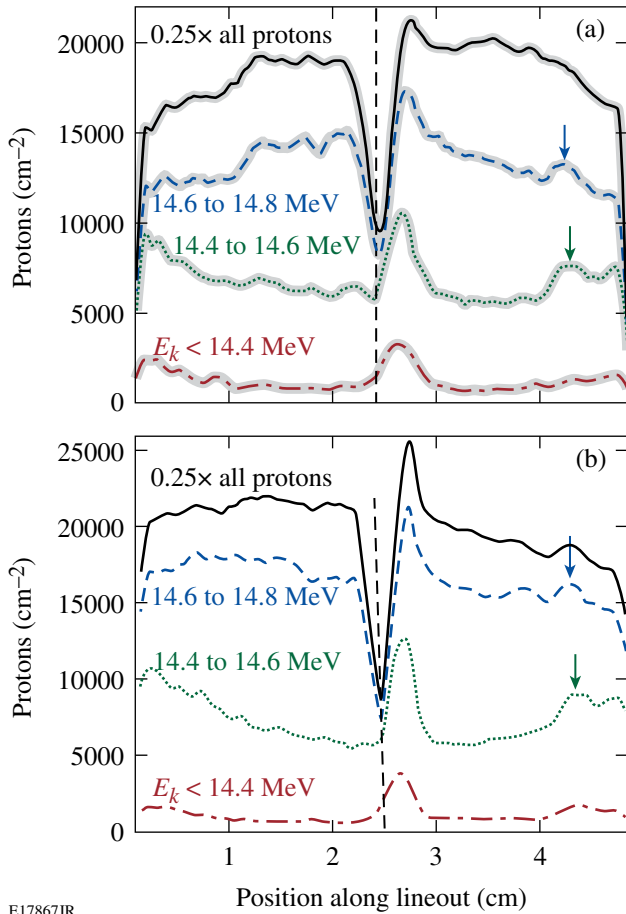


Figure 119.8

Direct comparisons of measured (dotted) and MC simulated (solid) proton-density lineouts across the core in shot 49704: (a) all protons; (b) protons intercepting the target ($E_k < 14.8$ MeV) (isolated by track diameter).

When the seed-field direction was reversed (by reversing the current in the coils), the deflection pattern (Fig. 119.10, shot 52532) reversed direction, with the deflection now away from the target stalk (a spatial reference fixed for all shots). This confirms the magnetic nature of the deflection and supports the “relocation” of the high-field deflection to the other side of the core. This is also evident in lineouts at several energies shown in Fig. 119.10(b), where, in addition to the offset peak near the center (at ~ 2.5 cm), there is again a concentration of tracks away from it (at 0.4 cm), caused by the peak of the compressed field in the hot spot. Analysis of the second peak deflection in shot 52532 revealed that the higher seed field (-62 kG), as compared to shot 51069, was amplified to at least -36 MG. The larger second peak area for Fig. 119.10(b) suggests higher hot-spot uniformity as more protons fall into these energy bands after being slowed down. The fields determined from Figs. 119.9 and 119.10 are the most conservative values, given



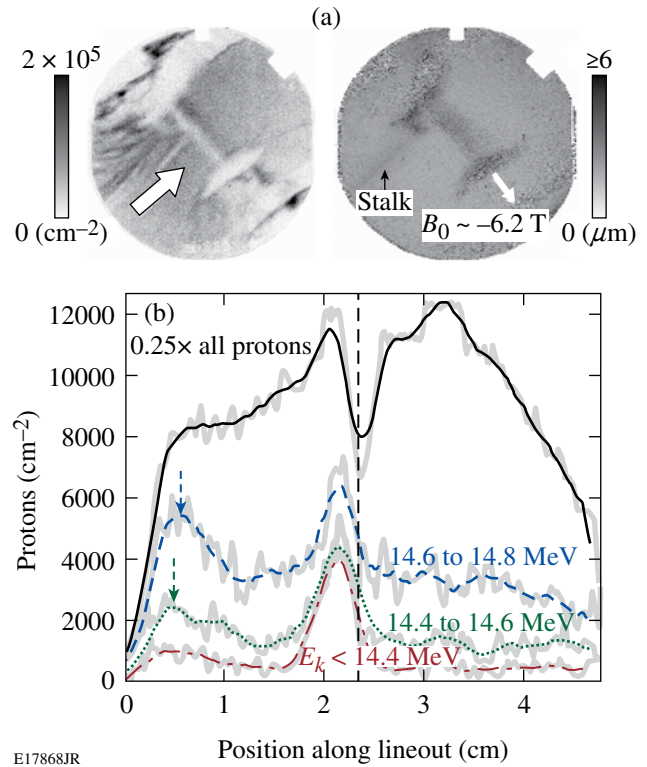
E17867JR

Figure 119.9

(a) Partitioning of the data in energy bands for shot 51069 exposed the protons that traverse the high field in the target center. (b) Partitioning in energy bands in the Monte Carlo simulation. The arrows in these plots indicate a second deflection peak at 1.9 cm from the target center.

by the lowest field B_{\max} , spread over the largest radius R_B , that can result in the observed deflection $\theta \sim \langle R_B B_{\max} \rangle$ without violating the flux conservation condition $\Phi \sim \langle R_B^2 B_{\max} \rangle \leq \Phi_0$. If the more realistic case is considered, where up to 40% of the initial magnetic flux ($\Phi_0 \approx 360 \text{ G cm}^2$) is lost as predicted by the hydro simulation, the estimated magnetic fields must be revised upward to match the observed deflections.

The effect of the amplified magnetic field on the hot-spot conditions was expected to be rather small for this experimental configuration. The 1-D hydrocode predicts a $2\times$ to $3\times$ increase in the yield caused by the temperature increase from thermal insulation in the hot spot. Note that higher temperatures are accompanied by lower hot-spot densities (Fig. 119.11, solid line) and lower plasma pressures since the total pressure (plasma + magnetic) is approximately independent of the magnetic field



E17868JR

Figure 119.10

(a) Proton track density and diameter maps for shot 52532. The stalk is on the left, and deflection is to the right (seed field reversed). (b) Smoothed total (solid) and reduced-energy-band lineouts show large deflection matching a compressed field $>36 \text{ MG}$. The arrows in (b) indicate the second deflection peak.

(the minimum volume-averaged hot-spot beta is ~ 300 , but is of the order of unity in the center). The highest neutron yield of 5.8×10^8 was measured in shot 49704 with a 10-kG seed field. With the present setup, however, and due to target parameter variations (gas pressure, orientation, positioning, and build quality), the $B_0 = 0$ yields already have variations of more than a factor of 3 (between 7.7×10^7 and 4.5×10^8). Such large shot-to-shot variations prevent an accurate assessment of the fusion yield enhancement caused by magnetic insulation. In addition, the scale of the experiment is such that the hot-spot ions most likely to undergo fusion reactions (at the Gamow peak) are essentially in the kinetic regime. This can be seen from Table 119.I, where $n_{e,\text{hs}} = 8 \times 10^{22} \text{ cm}^{-3}$, $T_{\text{hs}} = 1.5 \text{ keV}$, the Gamow peak is at 8.2 keV, and the Coulomb logarithms for the collisions of the 8-keV ions with thermal electrons and ions are $\Lambda_{ie} \approx 5$ and $\Lambda_{ii} \approx 8.6$, respectively. It is clear that the ions, having an $\sim 6\text{-}\mu\text{m}$ mean free path, will undergo only a few collisions before leaving the hot spot. The electrons are fully magnetized but are thermally decoupled from the ions since the thermal equilibration time is of the order of 100 ps.

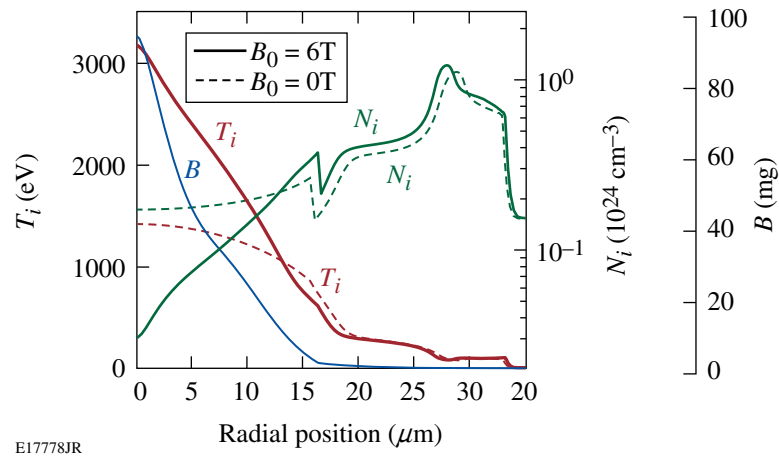


Figure 119.11

Ion temperature (T_i) and density (N_i) from *LILAC*-MHD simulations with (solid line) and without (dashed line) the magnetic field show that, along with a temperature increase caused by the magnetic field, a drop in the hot-spot density is predicted.

Table 119.I: Collision frequency (ν_{ie}, ν_{ii}), Hall parameter of ions (ω_{ci}/ν_{ii}), mean free paths, and Larmor radii for a simulated cylindrical magnetized hot spot ($R = 18$ mm) with an averaged field of 30 MG.

ν_{ie} ns ⁻¹	ν_{ii} ns ⁻¹	ω_{ci}/ν_{ii}	mfp _{ie} μm	mfp _{ii} μm	r_L , μm
5.4	147	0.97	151	5.6	5.7

The situation should improve significantly in planned spherical magnetized implosions where the hot-spot density and collisionality are significantly higher.

In summary, very high magnetic-flux compression has been achieved using the ablative pressure of the OMEGA laser to drive a cylindrical shell at high implosion velocity, trapping and compressing the embedded external field to tens of MG, high enough to magnetize the hot-spot plasma. Finding the parameter space where target performance will be most affected by the compressed magnetic field is the next step in these studies.

ACKNOWLEDGMENT

The authors thank Dr. F. Y. Thio and Dr. A. Velikovich for many illuminating discussions and for their encouragement in pursuing these novel experiments. This work was supported by the U.S. Department of Energy Office of Fusion Energy Sciences under Grants DE-FG02-04ER54768 and DE-FC02-ER54789 and by the Office of Inertial Confinement Fusion under Cooperative Agreement No. DE-FC52-08NA28302, the University of Rochester, and the New York State Energy Research and Development Authority. The support of DOE does not constitute an endorsement by DOE of the views expressed in this article.

REFERENCES

1. J. A. Wesson, *Tokamaks*, 3rd ed. (Clarendon Press, Oxford, 2004); A. H. Boozer, *Rev. Mod. Phys.* **76**, 1071 (2004).
2. R. Betti, K. Anderson, T. R. Boehly, T. J. B. Collins, R. S. Craxton, J. A. Delettrez, D. H. Edgell, R. Epstein, V. Yu. Glebov, V. N. Goncharov, D. R. Harding, R. L. Keck, J. H. Kelly, J. P. Knauer, S. J. Loucks, J. A. Marozas, F. J. Marshall, A. V. Maximov, D. N. Maywar, R. L. McCrory, P. W. McKenty, D. D. Meyerhofer, J. Myatt, P. B. Radha, S. P. Regan, C. Ren, T. C. Sangster, W. Seka, S. Skupsky, A. A. Solodov, V. A. Smalyuk, J. M. Soures, C. Stoeckl, W. Theobald, B. Yaakobi, C. Zhou, J. D. Zuegel, J. A. Frenje, C. K. Li, R. D. Petrasso, and F. H. Séguin, *Plasma Phys. Control. Fusion* **48**, B153 (2006).
3. P. W. McKenty, V. N. Goncharov, R. P. J. Town, S. Skupsky, R. Betti, and R. L. McCrory, *Phys. Plasmas* **8**, 2315 (2001).
4. J. A. Stamper, *Laser Part. Beams* **9**, 841 (1991).
5. Fields of 10^8 G have been associated with the high-current electron beams created in short-pulse laser-plasma interactions, but the small scale of these azimuthal fields precludes their use for hot-spot thermal insulation in ICF.
6. F. Herlach, *Rep. Prog. Phys.* **31**, 341 (1968); F. Herlach, *Rep. Prog. Phys.* **62**, 859 (1999).
7. C. M. Fowler, W. B. Garn, and R. S. Caird, *J. Appl. Phys.* **31**, 588 (1960).
8. A. D. Sakharov, *Sov. Phys. Usp.* **9**, 294 (1966).
9. F. S. Felber, M. A. Liberman, and A. L. Velikovich, *Phys. Fluids* **31**, 3675 (1988); F. S. Felber *et al.*, *J. Appl. Phys.* **64**, 3831 (1988).
10. R. C. Kirkpatrick, I. R. Lindemuth, and M. S. Ward, *Fusion Technol.* **27**, 201 (1995).

11. O. V. Gotchev, N. W. Jang, J. P. Knauer, M. D. Barbero, R. Betti, C. K. Li, and R. D. Petrasso, *J. Fusion Energy* **27**, 25 (2008).
12. M. A. Liberman and A. L. Velikovich, *J. Plasma Phys.* **31**, 381 (1984).
13. A. Hasegawa *et al.*, *Phys. Rev. Lett.* **56**, 139 (1986).
14. T. R. Boehly, D. L. Brown, R. S. Craxton, R. L. Keck, J. P. Knauer, J. H. Kelly, T. J. Kessler, S. A. Kumpan, S. J. Loucks, S. A. Letzring, F. J. Marshall, R. L. McCrory, S. F. B. Morse, W. Seka, J. M. Soures, and C. P. Verdon, *Opt. Commun.* **133**, 495 (1997).
15. J. P. Knauer, O. V. Gotchev, P. Chang, D. D. Meyerhofer, R. Betti, F. H. Séguin, C. K. Li, J. A. Frenje, and R. D. Petrasso, presented at the Innovative Confinement Concepts Workshop and US-Japan Workshop on Improvement in the Confinement of Compact Torus Plasmas, Reno, NV, 24–27 June 2008.
16. O. V. Gotchev, J. P. Knauer, P. Y. Chang, N. W. Jang, M. J. Shoup III, D. D. Meyerhofer, and R. Betti, *Rev. Sci. Instrum.* **80**, 043504 (2009).
17. C. K. Li, F. H. Séguin, J. A. Frenje, J. R. Rygg, R. D. Petrasso, R. P. J. Town, P. A. Amendt, S. P. Hatchett, O. L. Landen, A. J. Mackinnon, P. K. Patel, V. Smalyuk, J. P. Knauer, T. C. Sangster, and C. Stoeckl, *Rev. Sci. Instrum.* **77**, 10E725 (2006).
18. J. R. Rygg, F. H. Séguin, C. K. Li, J. A. Frenje, M. J.-E. Manuel, R. D. Petrasso, R. Betti, J. A. Delettrez, O. V. Gotchev, J. P. Knauer, D. D. Meyerhofer, F. J. Marshall, C. Stoeckl, and W. Theobald, *Science* **319**, 1223 (2008).
19. C. K. Li, F. H. Séguin, J. R. Rygg, J. A. Frenje, M. Manuel, R. D. Petrasso, R. Betti, J. Delettrez, J. P. Knauer, F. Marshall, D. D. Meyerhofer, D. Shvarts, V. A. Smalyuk, C. Stoeckl, O. L. Landen, R. P. J. Town, C. A. Back, and J. D. Kilkenny, *Phys. Rev. Lett.* **100**, 225001 (2008).
20. F. H. Séguin, J. A. Frenje, C. K. Li, D. G. Hicks, S. Kurebayashi, J. R. Rygg, B.-E. Schwartz, R. D. Petrasso, S. Roberts, J. M. Soures, D. D. Meyerhofer, T. C. Sangster, J. P. Knauer, C. Sorce, V. Yu. Glebov, C. Stoeckl, T. W. Phillips, R. J. Leeper, K. Fletcher, and S. Padalino, *Rev. Sci. Instrum.* **74**, 975 (2003).
21. S. Agostinelli *et al.*, *Nucl. Instrum. Methods Phys. Res. A* **506**, 250 (2003).
22. N. W. Jang, R. Betti, J. P. Knauer, O. Gotchev, and D. D. Meyerhofer, *Bull. Am. Phys. Soc.* **51**, 144 (2006).

Lorentz Mapping of Magnetic Fields in Hot, Dense Plasmas

Spontaneous generation of magnetic (\mathbf{B}) fields occurs pervasively in galactic^{1,2} and stellar³ settings and in numerous laboratory plasma experiments.^{2,4} For the case of the hot, dense plasmas of laser–plasma experiments^{4,5} or for scaled astrophysics experiments in the laboratory,^{2,4} self-generated magnetic and electric fields are often intertwined and inextricably coupled to the dynamics of the plasma evolution. This coupling makes the field-generation process complicated and also means that the effects of the fields can directly or indirectly act back on the plasma itself. Measuring local, self-generated fields, and distinguishing between electric (\mathbf{E}) and magnetic fields, is a formidable task.⁶

This article describes a monoenergetic proton radiography method that, when used in combination with Lorentz force mapping, allows one to precisely measure plasma field strengths as well as unequivocally discriminate between electric and magnetic fields. Electromagnetic fields in a high-energy-density plasma can be measured by passing monoenergetic protons through the plasma and observing how their trajectories are deflected by the fields. Any trajectory bending is due to the Lorentz force

$$\mathbf{F} = q\left(\mathbf{E} + \frac{\mathbf{v} \times \mathbf{B}}{c}\right), \quad (1)$$

where q is the proton charge and \mathbf{v} is the proton velocity, acting over a path length ℓ characteristic of the fields' spatial extent. For true quantitative analysis of data it is critical that \mathbf{v} be known accurately. If it is known in advance whether a field is \mathbf{B} or \mathbf{E} , Eq. (1) can be used directly to relate any observed trajectory bending to field strength. If bending is observed but there is no absolute knowledge of which field is present, the individual contributions of \mathbf{E} and \mathbf{B} can be determined by making two independent measurements. This discrimination can be accomplished by three methods, although practical implementation is often challenging: The first method measures the same plasma in the same way but with the direction of \mathbf{v} reversed; the second measures the same plasma but with protons of two discrete values of $|\mathbf{v}|$; and the third measures two plasmas that are identical except for the reversal of any \mathbf{B} field.

The experiment reported here utilized the third method to resolve ambiguities of field identity and field strength. The experimental setup used monoenergetic proton radiography, as illustrated in Fig. 119.12(a). A pulse of 14.9-MeV protons was generated from fusion reactions of deuterium (D) and helium-3 (${}^3\text{He}$) in a D_2 - ${}^3\text{He}$ -filled, glass-shell capsule driven by 17 OMEGA⁷ laser beams. This proton source was completely characterized using spectral,⁸ spatial,⁹ and temporal¹⁰ diagnostics; it had a mean energy of 14.9 ± 0.1 MeV, a spectral half-width $< 1.5\%$ (or half-width in the proton velocity distribution $< 0.75\%$), an emission region FWHM of $45 \mu\text{m}$, and a duration of 130 ps. The protons were used to image two identical, expanding plasma bubbles, formed on opposite sides of a $5\text{-}\mu\text{m}$ -thick plastic (CH) foil by two 1-ns-long laser interaction beams. Both beams had spot diameters of $850 \mu\text{m}$ and intensities of $8 \times 10^{13} \text{ W/cm}^2$; they were fired simultaneously and incident at 23.5° from the normal to the foil. To break the nearly isotropic proton fluence into “beamlets” (~ 1000 protons each) whose deflections could easily be observed and quantified, $150\text{-}\mu\text{m}$ -period nickel meshes were placed on opposite sides of the foil. Figure 119.12(b) is the resulting radiograph, recorded on a CR-39 nuclear track detector,⁸ with laser timing adjusted so that the bubbles were recorded 1.36 ns after the onset of the interaction beams.

The top bubble image in Fig. 119.12(b) is a type that we have recently begun studying^{11,12} and contrasting to predictions of the 2-D radiation–hydrodynamic code LASNEX.¹³ The simulations indicated that proton deflections are purely a result of a toroidal \mathbf{B} , parallel to the foil, arising from the $\nabla n_e \times \nabla T_e$ magnetic-field source term (where n_e and T_e are the electron number density and temperature).^{14,15} While the data and simulations were qualitatively similar, there was a consistent, quantitative mismatch between them throughout the bubble evolution (predicted apparent bubble sizes were $\sim 25\%$ smaller than observed;^{16,17} predicted field strengths were larger overall than observed; and field morphology details differed). This discrepancy effectively precluded use of the simulations to justify any *a priori* assumption that observed proton deflections were caused exclusively by a \mathbf{B} field and not by any component \mathbf{E}_{\parallel} (parallel to the foil) of an \mathbf{E} field.

To provide direct experimental identification of the field type as well as strength, the current experiment was designed so the second bubble reversed the sign of any \mathbf{B} relative to the first bubble (as seen from the detector) while leaving any E_{\parallel} unchanged. If the \mathbf{B} reversal had no effect on deflections of the monoenergetic protons used to image the plasma, any deflections would necessarily have been dominated by E_{\parallel} . If the reversal resulted in equal but oppositely directed deflections of the monoenergetic protons, it would demonstrate the clear dominance of \mathbf{B} . Qualitatively, the latter is what is seen in the image: the bubble on the front side of the foil (top of image) appears expanded, while the bubble on the back side appears contracted.

Figure 119.12(c) shows the absolute values of the beamlet deflection angles θ as a function of position at the foil; θ is calculated from the apparent displacement of a beamlet in an image relative to where it would be without deflection. The peak θ values occur at the foil on two circles of the same radius, and the amplitudes are the same for both circles. This is seen

quantitatively in Fig. 119.13(a), which shows θ as a function of radius measured from each bubble's center. Because of Eq. (1) and the fact that \mathbf{B} is reversed between the bubbles while E is not, it follows that we can decompose the total deflections $\theta_{\text{top}}(r)$ and $\theta_{\text{bottom}}(r)$ for the top and bottom bubbles into parts due only to \mathbf{B} and E by assuming the two bubbles are otherwise equivalent. Then

$$\theta_{\text{top}}(r) = \theta_E(r) + \theta_{\mathbf{B},\text{top}}(r), \quad (2)$$

$$\theta_{\text{bottom}}(r) = \theta_E(r) - \theta_{\mathbf{B},\text{top}}(r), \quad (3)$$

from which it follows that

$$\theta_E(r) = [\theta_{\text{top}}(r) + \theta_{\text{bottom}}(r)]/2, \quad (4)$$

$$\theta_{\mathbf{B}}(r) = [\theta_{\text{top}}(r) - \theta_{\text{bottom}}(r)]/2. \quad (5)$$

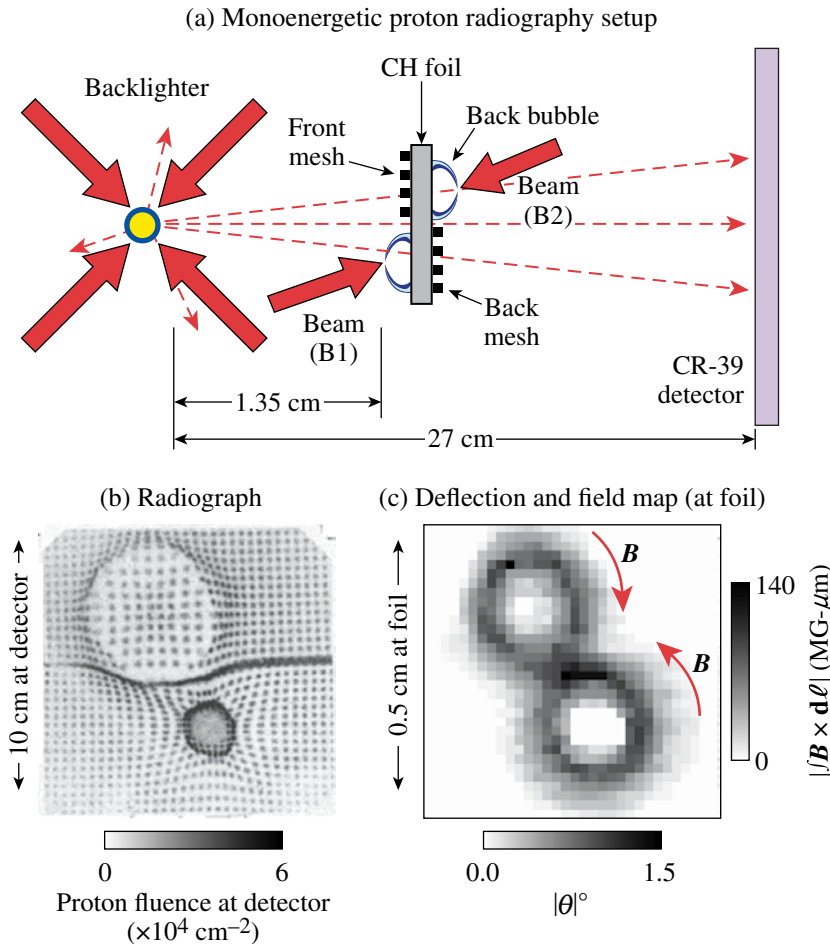


Figure 119.12

(a) Proton radiography setup, (b) proton radiograph of two laser-generated plasma bubbles, and (c) spatial map of proton beamlet deflection angle (or equivalently the magnetic field strength) as a function of position on the foil. Note in Fig. 119.13(b) that the deflections are associated almost exclusively with a \mathbf{B} field near the foil, meaning that (c) can also be viewed as a magnetic field map. Part (c) shows that the two bubbles were actually the same size, even though the apparent sizes are different in the radiograph. Orientation of the images is as seen from behind the detector, looking toward the backlighter. The radiograph was acquired during OMEGA shot 46535.

E18117JR

The results are shown in Fig. 119.13(b) after converting $\theta_B(r)$ and $\theta_E(r)$ to $\int \mathbf{B} \times d\boldsymbol{\ell}$ and $\int \mathbf{E}_{\parallel} \times d\boldsymbol{\ell}$ using Eq. (1). The vertical display scales for \mathbf{E} and \mathbf{B} were selected so the relative amplitudes of the curves indicate the relative amounts of proton deflection. The effect of \mathbf{B} greatly dominates the effect of \mathbf{E}_{\parallel} , whose measured amplitude is smaller than measurement uncertainties.¹⁸

Figure 119.12(c) reveals a toroidal topology for the \mathbf{B} field, with a shell thickness of about $400 \mu\text{m}$. An estimate of the maximum local $|\mathbf{B}|$ is then $100 \text{ MG} \cdot \mu\text{m} / 400 \mu\text{m} \sim 0.3 \text{ MG}$. For this field, the Hall parameter $\omega_{ce}\tau$ (where ω_{ce} is the electron gyrofrequency and τ is the electron-ion collision time^{14,15}) is of order 1. Since thermal conductivity is proportional to $1/[1 + (\omega_{ce}\tau)^2]$ (Refs. 14 and 19), it follows that field-induced inhibition of thermal transport across the plasma bubble boundary will occur.

Interestingly, this may provide insight as to why the simulations, while correctly predicting that a toroidal \mathbf{B} field was the primary cause of the deflections, could overestimate the field and underestimate the bubble size. Thomson-scattering²⁰ measurements indicated that the actual electron temperature T_e was $\sim 40\%$ lower than the value predicted by LASNEX ($450 \mu\text{m}$ away from the foil and $600 \mu\text{m}$ from the central axis of a bubble, the measured T_e was 470 eV while the predicted value was 780 eV). With the predicted plasma temperature too high, the predicted magnetic diffusivity would be too low [since it is proportional to $T^{-3/2}$ (Ref. 14)] and the predicted \mathbf{B} field would dissipate too slowly, leading to higher field strengths, higher $\omega_{ce}\tau$, and an even more slowly decaying electron temperature. Such considerations and more detailed data/simulation comparisons will be important for advancing our basic understanding and our predictive capabilities with various codes.

The absolute experimental determination here that the fields responsible for the structure of Fig. 119.12(b) are magnetic allows us to revisit the images of Refs. 11 and 12 (showing radiographs of similar plasma bubbles on one side of the foil only) with confidence that they also reflect magnetic fields. Reference 11 shows images that represent the complete time evolution of bubble structure throughout the 1-ns laser pulse and for an additional 2 ns afterward. Those images were recorded with the same integration time ($\sim 130 \text{ ps}$) as used here and show the temporal evolution of the plasma bubble radius and field magnitude. In addition, a breakdown in azimuthal symmetry was observed at times slightly later than that of Fig. 119.12(b) here.

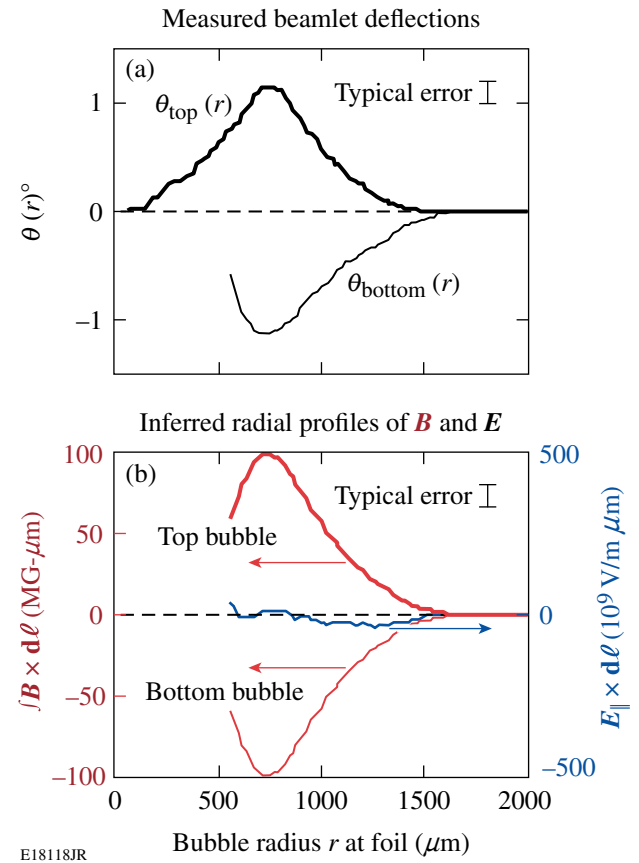


Figure 119.13

Measured beamlet deflection angles θ as a function of radius r in the top and bottom bubbles of Fig. 119.12(b) (positive is away from the bubble center), and inferred radial profiles of $\int \mathbf{B} \times d\boldsymbol{\ell}$ and $\int \mathbf{E}_{\parallel} \times d\boldsymbol{\ell}$ in the two bubbles. In (b), the vector $\int \mathbf{B} \times d\boldsymbol{\ell}$ is plotted as a positive number for a toroidal \mathbf{B} field in the clockwise direction of Fig. 119.12(c), while $\int \mathbf{E}_{\parallel} \times d\boldsymbol{\ell}$ is plotted as positive for an \mathbf{E} field pointing away from the bubble center. \mathbf{B} has opposite directions in the two bubbles, while \mathbf{E} has the same direction. Note that the absence of information about θ_{bottom} for $r < \sim 500 \mu\text{m}$ reflects the overlap of beamlets in the center of the bottom bubble image in Fig. 119.12(b), which prevented beamlet deflection measurements in that region.

Essential to the successful implementation of the technique of field discrimination and quantification are the isotropic and monoenergetic characteristics of the protons (the velocity uncertainty was $< 1\%$ over the imaged plasma). Other recent important methods of ion generation from intense laser-plasma interactions,^{21–23} while useful in different radiographic settings, would be compromised in the present context because of the energy spread and anisotropy of the ion fluences. In addition, other techniques of single-point field measurement at extremely high laser intensities ($\sim 10^{20} \text{ W/cm}^2$, Ref. 24) do not generate global field maps that show the entire laser-plasma morphology, a prerequisite to understanding plasma dynamics.

Variations of this monoenergetic proton radiography are now being applied to other important plasma/field problems in high-energy-density physics. For example, recent work in inertial confinement fusion^{25,26} showed, through single-sided monoenergetic proton radiography, the presence of strong striated fields around an imploding capsule.⁶ Unresolved in this work was the issue of whether the fields were magnetic or electric; yet the identification of field type is of paramount importance because different fields would involve different generation mechanisms and would have a significantly different impact on plasma evolution (through such processes as thermal transport modification). By simultaneously irradiating a subject implosion from two different directions, the methodology described above can unambiguously discern whether these fields are magnetic or electric. If magnetic, it is quite possible that the striations are a result of an electrothermal instability,²⁷ potentially leading to the seeding of Rayleigh–Taylor instabilities²⁷ that could deleteriously impact implosion dynamics.²⁸

In another experiment involving accelerating, rippled plasma foils,²⁹ B fields are suspected—as a consequence of the Rayleigh–Taylor instability²⁸—to cause the monoenergetic proton deflections seen when the foil was irradiated from a single side.³⁰ However, unique field and instability identification could be established by proton backlighting, from one direction, of a foil with ripples on both sides [in a fashion similar to that depicted for the two plasma bubbles in Fig. 119.12(a)]. (In such an experiment, the mesh would be removed.) In general, applying these field-mapping radiographs to a large class of high-energy-density plasmas will lead to quantifying the nature, the physical extent, and the evolution of embedded, spontaneous fields. By inference, this should also lead to new insights into the origin and dynamics of the pervasive fields of stellar jets³¹ and nebulae,³² a major goal of laboratory astrophysics.^{2,33}

ACKNOWLEDGMENT

This work was supported by the Fusion Science Center (FSC) at the University of Rochester (grant no. DE-FG03-03NA00058), the National Laser Users' Facility (DE-FG52-07NA28059), the Office of Defense Programs (DE-FG52-06NA26203), Lawrence Livermore National Laboratory (subcontract Grant No. B5504974), and the Laboratory for Laser Energetics at the University of Rochester (subcontract Grant No. 412160-001G)—all through the U.S. Department of Energy. J.R.R. also acknowledges the FSC for his postdoctoral appointment. In addition, the authors express their gratitude to General Atomics and the Laboratory for Laser Energetics (LLE) for target fabrication and to LLE's laser operations team.

REFERENCES

1. W. Baumjohann and R. A. Treumann, *Basic Space Plasma Physics* (Imperial College Press, London, 1996).
2. B. A. Remington *et al.*, *Science* **284**, 1488 (1999).
3. E. N. Parker, *Astrophys. J.* **128**, 664 (1958).
4. R. P. Drake, *High-Energy-Density Physics: Fundamentals, Inertial Fusion, and Experimental Astrophysics*, Shock Wave and High Pressure Phenomena (Springer, Berlin, 2006).
5. W. L. Kruer, *The Physics of Laser Plasma Interactions*, Frontiers in Physics (Westview Press, Boulder, CO, 2003).
6. J. R. Rygg, F. H. Séguin, C. K. Li, J. A. Frenje, M. J.-E. Manuel, R. D. Petrasso, R. Betti, J. A. Delettrez, O. V. Gotchev, J. P. Knauer, D. D. Meyerhofer, F. J. Marshall, C. Stoeckl, and W. Theobald, *Science* **319**, 1223 (2008).
7. J. M. Soures, R. L. McCrory, C. P. Verdon, A. Babushkin, R. E. Bahr, T. R. Boehly, R. Boni, D. K. Bradley, D. L. Brown, R. S. Craxton, J. A. Delettrez, W. R. Donaldson, R. Epstein, P. A. Jaanimagi, S. D. Jacobs, K. Kearney, R. L. Keck, J. H. Kelly, T. J. Kessler, R. L. Kremens, J. P. Knauer, S. A. Kumpan, S. A. Letzring, D. J. Lonobile, S. J. Loucks, L. D. Lund, F. J. Marshall, P. W. McKenty, D. D. Meyerhofer, S. F. B. Morse, A. Okishev, S. Papernov, G. Pien, W. Seka, R. Short, M. J. Shoup III, M. Skeldon, S. Skupsky, A. W. Schmid, D. J. Smith, S. Swales, M. Wittman, and B. Yaakobi, *Phys. Plasmas* **3**, 2108 (1996).
8. F. H. Séguin, J. A. Frenje, C. K. Li, D. G. Hicks, S. Kurebayashi, J. R. Rygg, B.-E. Schwartz, R. D. Petrasso, S. Roberts, J. M. Soures, D. D. Meyerhofer, T. C. Sangster, J. P. Knauer, C. Sorce, V. Yu. Glebov, C. Stoeckl, T. W. Phillips, R. J. Leeper, K. Fletcher, and S. Padalino, *Rev. Sci. Instrum.* **74**, 975 (2003).
9. F. H. Séguin, J. L. DeCiantis, J. A. Frenje, C. K. Li, J. R. Rygg, C. D. Chen, R. D. Petrasso, J. A. Delettrez, S. P. Regan, V. A. Smalyuk, V. Yu. Glebov, J. P. Knauer, F. J. Marshall, D. D. Meyerhofer, S. Roberts, T. C. Sangster, C. Stoeckl, K. Mikaelian, H. S. Park, H. F. Robey, and R. E. Tipton, *Phys. Plasmas* **13**, 082704 (2006).
10. J. A. Frenje, C. K. Li, F. H. Séguin, J. DeCiantis, S. Kurebayashi, J. R. Rygg, R. D. Petrasso, J. Delettrez, V. Yu. Glebov, C. Stoeckl, F. J. Marshall, D. D. Meyerhofer, T. C. Sangster, V. A. Smalyuk, and J. M. Soures, *Phys. Plasmas* **11**, 2798 (2004).
11. C. K. Li, F. H. Séguin, J. A. Frenje, J. R. Rygg, R. D. Petrasso, R. P. J. Town, P. A. Amendt, S. P. Hatchett, O. L. Landen, A. J. Mackinnon, P. K. Patel, M. Tabak, J. P. Knauer, T. C. Sangster, and V. A. Smalyuk, *Phys. Rev. Lett.* **99**, 015001 (2007).
12. C. K. Li, F. H. Séguin, J. A. Frenje, J. R. Rygg, R. D. Petrasso, R. P. J. Town, O. L. Landen, J. P. Knauer, and V. A. Smalyuk, *Phys. Rev. Lett.* **99**, 055001 (2007).

13. G. B. Zimmerman and W. L. Kruer, *Comments Plasma Phys. Control. Fusion* **2**, 51 (1975).
14. S. I. Braginskii, in *Reviews of Plasma Physics*, edited by Acad. M. A. Leontovich (Consultants Bureau, New York, 1965), Vol. 1.
15. M. G. Haines, *Phys. Rev. Lett.* **47**, 917 (1981).
16. The disagreement between experiment and LASNEX simulation appeared to be less pronounced than this in an earlier publication,¹⁷ but that was because the simulation utilized slightly incorrect imaging system dimensions.
17. C. K. Li, F. H. Séguin, J. A. Frenje, J. R. Rygg, R. D. Petrasso, R. P. J. Town, P. A. Amendt, S. P. Hatchett, O. L. Landen, A. J. Mackinnon, P. K. Patel, V. A. Smalyuk, T. C. Sangster, and J. P. Knauer, *Phys. Rev. Lett.* **97**, 135003 (2006).
18. Measurement of electric fields perpendicular to the foil in a single-bubble experiment was presented in C. K. Li, F. H. Séguin, J. A. Frenje, J. R. Rygg, R. D. Petrasso, R. P. J. Town, P. A. Amendt, S. P. Hatchett, O. L. Landen, A. J. Mackinnon, P. K. Patel, V. Smalyuk, J. P. Knauer, T. C. Sangster, and C. Stoeckl, *Rev. Sci. Instrum.* **77**, 10E725 (2006).
19. D. S. Montgomery *et al.*, *Phys. Rev. Lett.* **73**, 2055 (1994).
20. D. H. Froula *et al.*, *Rev. Sci. Instrum.* **77**, 10E522 (2006).
21. B. M. Hegelich *et al.*, *Nature* **439**, 441 (2006).
22. M. Borghesi *et al.*, *Phys. Rev. Lett.* **81**, 112 (1998).
23. A. J. Mackinnon *et al.*, *Phys. Rev. Lett.* **97**, 045001 (2006).
24. M. Tatarakis *et al.*, *Nature* **415**, 280 (2002).
25. J. Nuckolls *et al.*, *Nature* **239**, 139 (1972).
26. S. Atzeni and J. Meyer-ter-Vehn, *The Physics of Inertial Fusion: Beam Plasma Interaction, Hydrodynamics, Hot Dense Matter*, International Series of Monographs on Physics (Clarendon Press, Oxford, 2004).
27. M. G. Haines, *Can. J. Phys.* **64**, 912 (1986).
28. A. Nishiguchi, *Jpn. J. Appl. Phys.* **41**, 326 (2002).
29. V. A. Smalyuk, S. X. Hu, V. N. Goncharov, D. D. Meyerhofer, T. C. Sangster, D. Shvarts, C. Stoeckl, B. Yaakobi, J. A. Frenje, and R. D. Petrasso, *Phys. Rev. Lett.* **101**, 025002 (2008).
30. R. Petrasso, *Bull. Am. Phys. Soc.* **52**, 97 (2007).
31. P. Hartigan *et al.*, *Astrophys. J.* **661**, 910 (2007).
32. J. J. Hester *et al.*, *Astrophys. J.* **456**, 225 (1996).
33. D. D. Ryutov *et al.*, *Phys. Plasmas* **8**, 1804 (2001).

Characterization and Optimization of Yb-Doped Photonic-Crystal Fiber Rod Amplifiers Using Spatially Resolved Spectral Interferometry

Introduction

New Yb-doped photonic-crystal fibers (PCF's) have enabled fiber-based chirped-pulse-amplification (CPA) systems to produce millijoule-level pulses, compressible to femtosecond pulse widths.^{1,2} Rigid double-clad fiber rods are commercially available with large effective areas ($>2300 \mu\text{m}^2$) and high pump absorption ($\sim 30 \text{ dB/m}$ at 976 nm) for efficient amplification in less than a meter of fiber. The combination of large effective areas and short amplifier lengths limits the suppression of higher-order modes (HOM's), however, and these fibers may support several modes in addition to the fundamental. The rigid rod construction reduces the coupling between the weakly guided fundamental and other modes in the fiber. HOM's may be excited when the signal is injected, which is typically done by focusing a free-space beam into the core. Relatively small amounts of HOM that are co-polarized with the fundamental mode can significantly degrade the beam quality and pointing stability because they interfere coherently.^{3,4}

This article reports the first application of a recently proposed technique, S^2 imaging,^{5,6} to measure the modes of a Yb-doped PCF amplifier at full power. The technique, based on spatially resolved spectral interferometry, can detect small amounts of HOM that beat with the fundamental mode. S^2 imaging measures HOM fields relative to the fundamental mode without requiring *a priori* knowledge of the design of the fiber or its mode content. S^2 imaging provides feedback when optimizing signal injection and is more sensitive than measuring the amplifier gain.

S^2 Imaging

S^2 imaging detects HOM content from fringes in the spatially resolved spectra that are sampled across the beam profile. Nicholson *et al.* showed that an HOM's profile and its intensity and phase relative to the fundamental mode can be directly calculated from the spatially dependent fringe visibility.⁵ Consider two modes defined by the spectral fields $E_1(x,y,\omega)$ and $E_2(x,y,\omega)$, where E_1 is assumed to be the fundamental mode (such as the LP_{01}) and E_2 is an HOM that is coherent

and co-polarized with E_1 . As $|E_1|$ is nonzero across the beam, E_2 can be expressed as

$$E_2(x,y,\omega) = \alpha(x,y,\omega)E_1(x,y,\omega), \quad (1)$$

where $\alpha(x,y,\omega)$ is the relative field amplitude of the HOM at a given position in the beam. It is a complex function: $|\alpha| \exp(i\phi_\alpha)$. After propagation with relative group delay, $\Delta\tau_G$, the mode fields are related by

$$E_2(x,y,\omega) = \alpha(x,y,\omega)E_1(x,y,\omega) \exp(-i\omega\Delta\tau_G). \quad (2)$$

Spectral interference between the two fields produces a combined spectral intensity of the form

$$\begin{aligned} I(x,y,\omega) &= |E_1(x,y,\omega) + E_2(x,y,\omega)|^2 \\ &= I_1(x,y,\omega) \left[1 + |\alpha|^2 + 2|\alpha| \cos(\omega\Delta\tau_G - \phi_\alpha) \right]. \end{aligned} \quad (3)$$

The spectrum contains fringes because of the relative group delay between the modes. Assuming that α and $\Delta\tau_G$ are slowly varying functions of frequency and there are several fringes across the spectrum, standard Fourier analysis is used to extract the relative powers of the two modes. The ac sidebands produced by the modal interference have an amplitude relative to the dc peak that is given by

$$f(x,y) = \frac{2|\bar{\alpha}| \exp(-i\phi_\alpha)}{1 + |\alpha|^2}, \quad (4)$$

where $\bar{\alpha}(x,y)$ is the spectral average of $\alpha(x,y,\omega)$ that can be calculated directly from $f(x,y)$:

$$\bar{\alpha}(x,y) = \frac{1 - \sqrt{1 - 4|f(x,y)|^2}}{2f(x,y)}. \quad (5)$$

The relative power of the HOM to the fundamental is obtained from $\bar{\alpha}(x,y)$ and the total intensity integrated over the entire spectrum, $I_T(x,y)$:

$$\begin{aligned} P_2/P_1 &= \iint I_2(x,y)dx dy / \iint I_1(x,y)dx dy \\ &= \frac{\iint I_T |\bar{\alpha}|^2 / (1 + |\bar{\alpha}|^2) dx dy}{\iint I_T / (1 + |\bar{\alpha}|^2) dx dy}. \end{aligned} \quad (6)$$

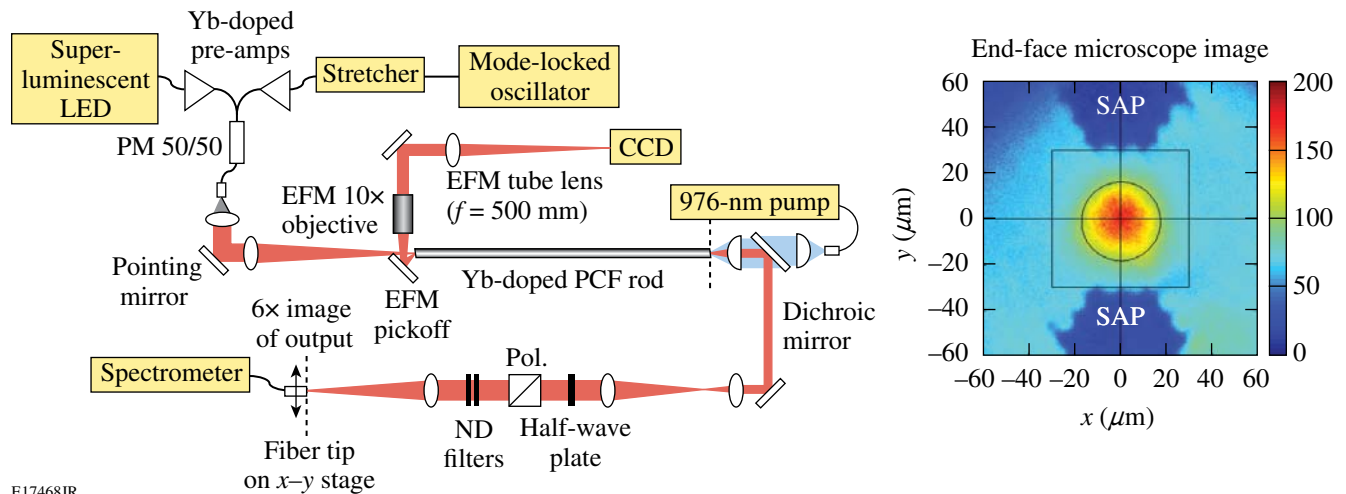
Since the S^2 technique is fundamentally interferometric in nature, the relative phase between the modes at a given position in the beam is encoded on the phase of the spectral oscillations at that position. Equation (4) shows that the phase between the modes across the beam, $\phi_\alpha(x,y)$, is given by the phase of $f(x,y)$. The phase of the fundamental mode does not vary across the beam, so $\phi_\alpha(x,y)$ represents the phase variation across the HOM. An LP_{11} mode, for example, has two lobes with a π -phase shift between them, which can be measured using S^2 imaging.⁵ Although only one HOM was considered here, multiple HOM's can be imaged simultaneously providing the relative group delays between each HOM and the fundamental mode are sufficiently different that the sidebands are clearly resolved. Reference 6 extends this analysis to cases where (1) the excitation of the HOM's is distributed along the fiber device and (2) the coupling between the modes and their relative group delays is frequency dependent. While this alternate method of analysis is more general, it requires that each HOM

is weak compared to the fundamental mode (relative power less than -15 dB) to ensure S^2 imaging does not underestimate the HOM power.

Experimental Setup

The experimental setup is shown in Fig. 119.14. The Yb-doped PCF fiber (DC-200/70-PM-Yb-ROD from Crystal Fibre A/S) was a rigid rod ($0.8\text{-m} \times 1.7\text{-mm}$ diameter) with angle-cleaved end faces (4°). The signal core, formed by a hexagonal matrix of air holes, has an effective area of $2300 \mu\text{m}^2$, corresponding to a mode-field diameter (MFD) = $55 \mu\text{m}$ and a numerical aperture (N.A.) ≈ 0.015 . Boron-doped stress-applying parts (SAP's) limit propagation to a single linear polarization in the signal wavelength range.² The amplifier was pumped at 976 nm using multimode pigtailed diodes. An output power of 16 W at 1055 nm with 16.6 dB of gain was obtained for $\sim 50 \text{ W}$ of absorbed pump power.

The amplifier output was sampled using a single-mode fiber probe (MFD = $6 \mu\text{m}$, N.A. = 0.14) and a fiber-coupled spectrometer (Ocean Optics HR2000+). The beam was attenuated using three uncoated reflections and neutral-density (ND) filters. The PCF end face was imaged onto the fiber probe with $6\times$ magnification so that the MFD of the probe fiber was less than $1/50$ of the beam's diameter ($1/e^2$). High-speed actuators (Newport LTA) were used to translate the fiber probe across the beam and the spectrum was measured at each point. The total acquisition time for a scan (32×32) was approximately 6 min . The half-wave plate was set to either align the amplifier output with the polarizer or rotate the polarization by 45° . In the first



E17468JR

Figure 119.14
Experimental setup. The EFM image shows signal beam at injection, aligned between the two SAP regions that are backlit by the pump.

case, fringes were produced by HOM's that were co-polarized with the fundamental mode. In the second, fringes could potentially be produced by HOM's that were orthogonally polarized to the fundamental. Thus, the relative polarization state of the HOM to the fundamental was determined by comparing the fringe visibility for both wave-plate settings.

One challenge in applying S^2 imaging to short amplifiers is that the relative group delay between modes is short, resulting in spectral fringes with a long period. A combination of stretched Yb oscillator pulses at 1055 nm and output from a superluminescent light-emitting diode (SLED) at 1035 nm was injected to provide at least four fringes across the spectrum. Each spatially resolved spectrum was first normalized by the spectrum integrated over the beam before Fourier analysis so that the entire wavelength range (1020 to 1060 nm) could be used.

Independent measurements of the signal beam offset at injection were provided using an end-face microscope (EFM) to image the input end of the PCF amplifier. The EFM used a pickoff mirror located a few millimeters from the fiber end and a microscope objective to capture the signal reflection from the angle-cleaved fiber face. In addition, the EFM collected part of the residual pump light exiting the fiber at large angles. Figure 119.14 shows a typical EFM image with signal and pump light present. The pickoff angle exceeded the numerical aperture of pump light guided in the two trapezoidal SAP's; therefore, they appear as dark regions that indicate the location of the signal core. Using standard image-processing techniques, this simple setup can measure signal-to-core overlap at the end face with micron-level precision.

Experimental Results of S^2 Imaging Measurements

Figure 119.15(a) shows the amplified spectrum integrated over the entire beam for the SLED and mode-locked oscillator (ML OSC). Figure 119.15(b) shows two examples of spatially resolved spectra, measured at positions of low- and high-fringe visibility, after normalization by the integrated spectrum. The corresponding Fourier magnitudes are plotted versus group delay in Fig. 119.15(c) and show an interference peak at a group delay of 420 fs/m.

Mode images were extracted using the spatial dependence of 420-fs/m peak. The images are shown in Fig. 119.16 along with a direct charge-coupled-device (CCD) measurement of the beam. The dimensions for all images correspond to the amplifier output before the 6 \times magnification in front of the fiber probe. The modes are the fundamental LP₀₁ mode and the LP₁₁ mode, which is aligned with the SAP axis. The LP₁₁ mode was determined to be co-polarized with the LP₀₁ mode by rotating the half-wave plate before the polarizer and noting that the fringe visibility remained constant. In principle, S^2 imaging can detect many HOM's from a single scan. In this case only one clear mode was observed, corresponding to the generation of the LP₁₁ mode at injection into the amplifier. Other modes could be present, such as HOM's generated from scattering from inhomogeneities distributed along the amplifier length. The relative group delay depends on the scattering position, and, therefore, fringes are produced with a range of periods from a minimum value set by the total length of the amplifier to larger values. Detecting HOM's from such distributed coupling is possible⁴ but was not feasible given the signal-to-noise ratio of the data.

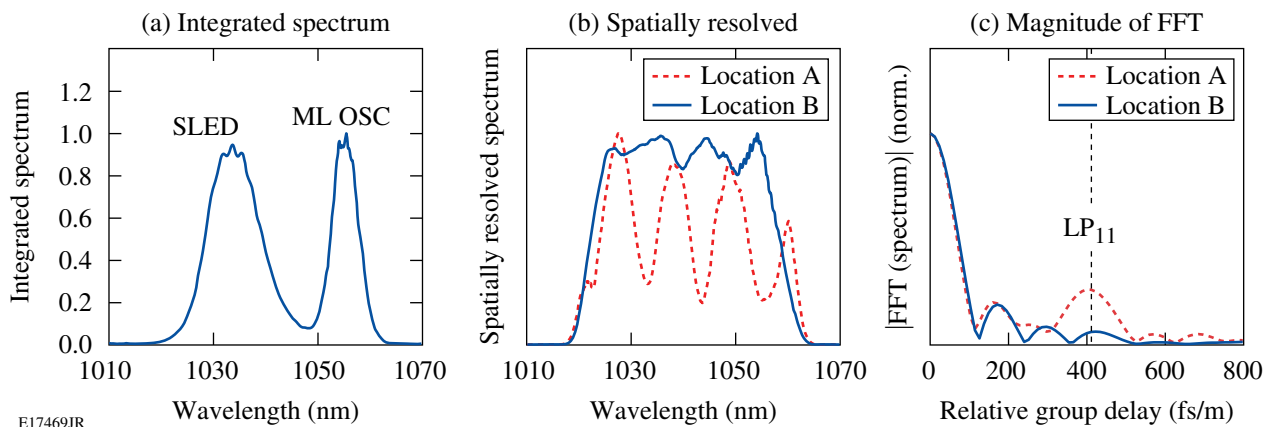


Figure 119.15

(a) Integrated amplified spectrum. (b) Spatially resolved spectra, after normalization with the integrated spectrum, at locations of low- and high-fringe visibility (solid and dashed, respectively). (c) Corresponding Fourier transform magnitudes, with dashed line showing the location of LP₁₁ signal.

S^2 imaging provides a direct measurement of the beam profile at a given wavelength. This method of viewing the data is presented as a sequence of images in Fig. 119.17. The relative

LP_{11} power in this case was -13 dB. As the wavelength changes, the beam centroid moves vertically in the y direction, along the LP_{11} axis (see Fig. 119.18). This beam motion is a direct

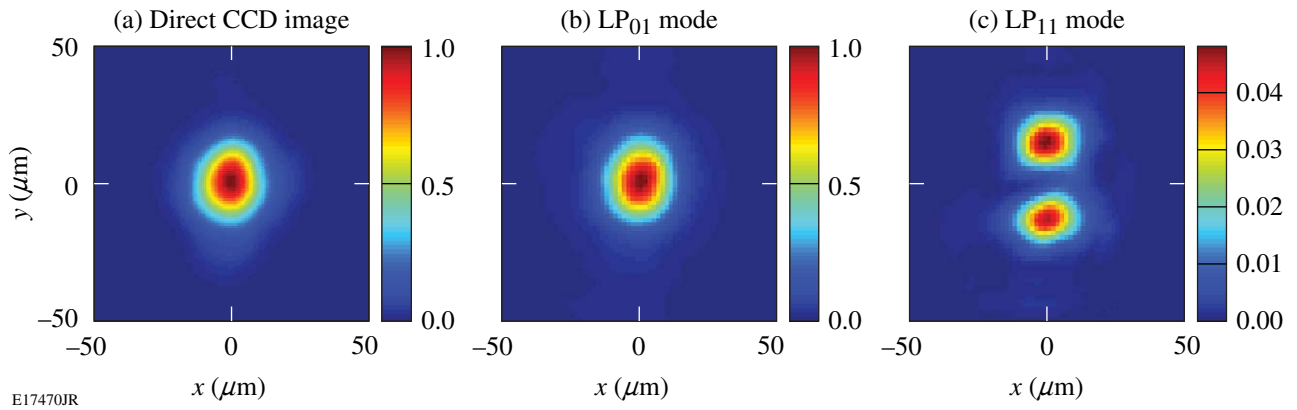


Figure 119.16
 (a) Output beam as measured using a 12-bit CCD. [(b), (c)] Modes reconstructed using the S^2 technique.

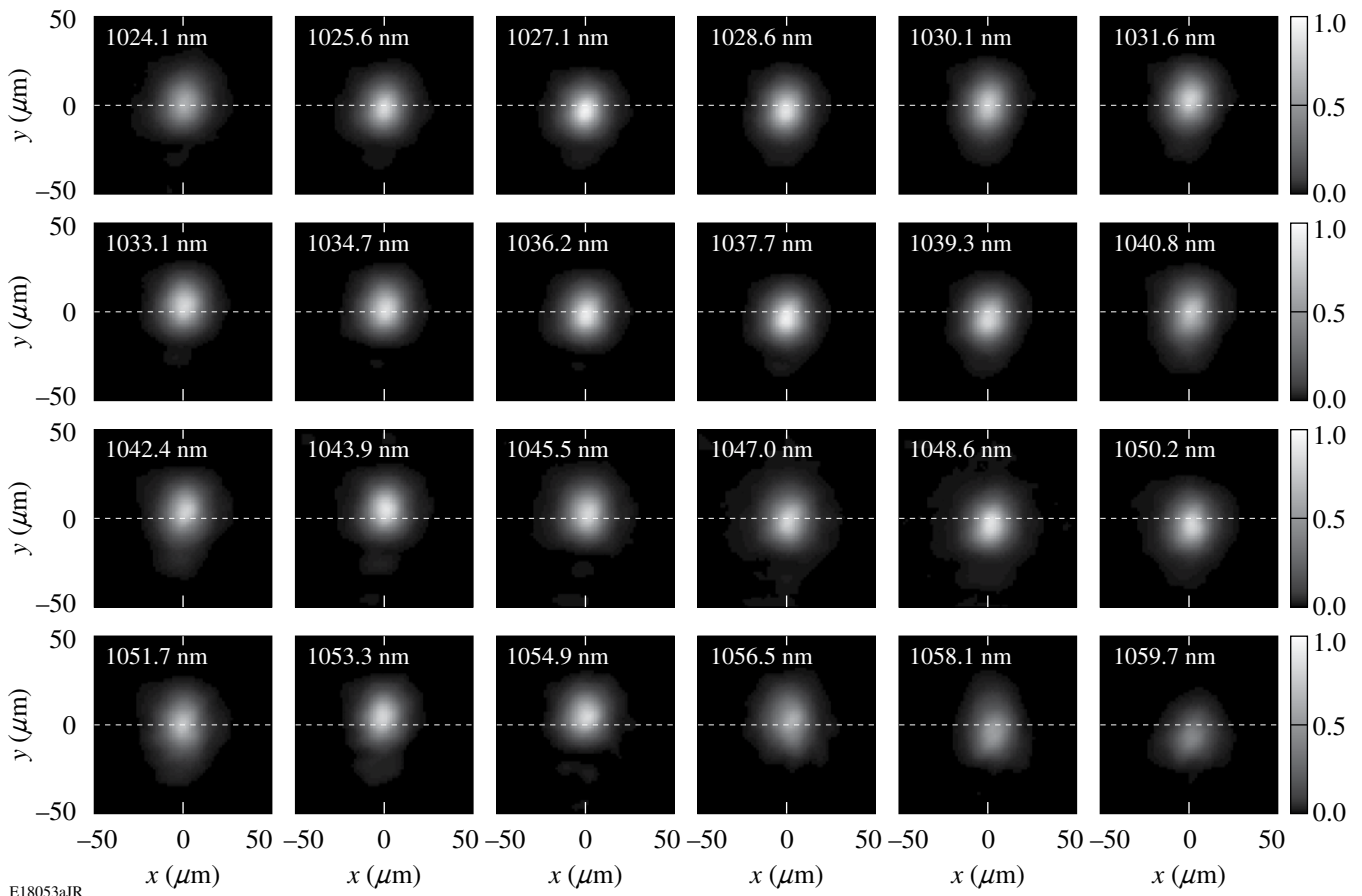
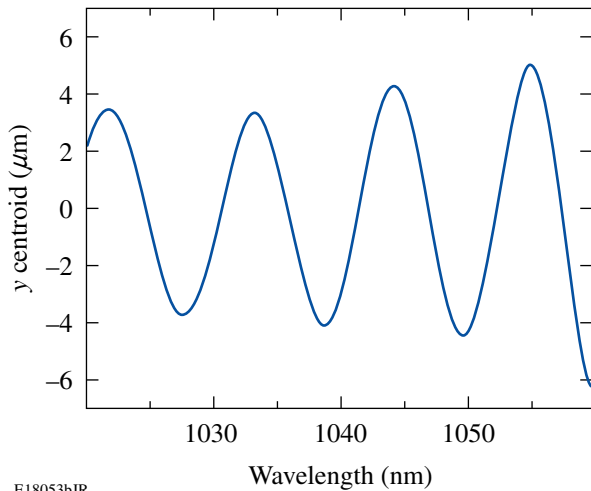


Figure 119.17
 Spectrally resolved images that are measured by the S^2 technique. The oscillation of the beam with wavelength in the y direction is due to the wavelength dependence of the phase between the LP_{01} and LP_{11} modes. [Click here for animation](#)

consequence of the coherence and co-polarization of the two modes. At wavelengths corresponding to a positive y centroid, the upper lobe of the LP_{11} mode interferes constructively with the LP_{01} mode, and the lower lobe interferes destructively. This oscillation would not be seen if the modes were incoherent or orthogonally polarized.



E18053bJR

Figure 119.18
The beam centroid in the y direction as a function of wavelength.

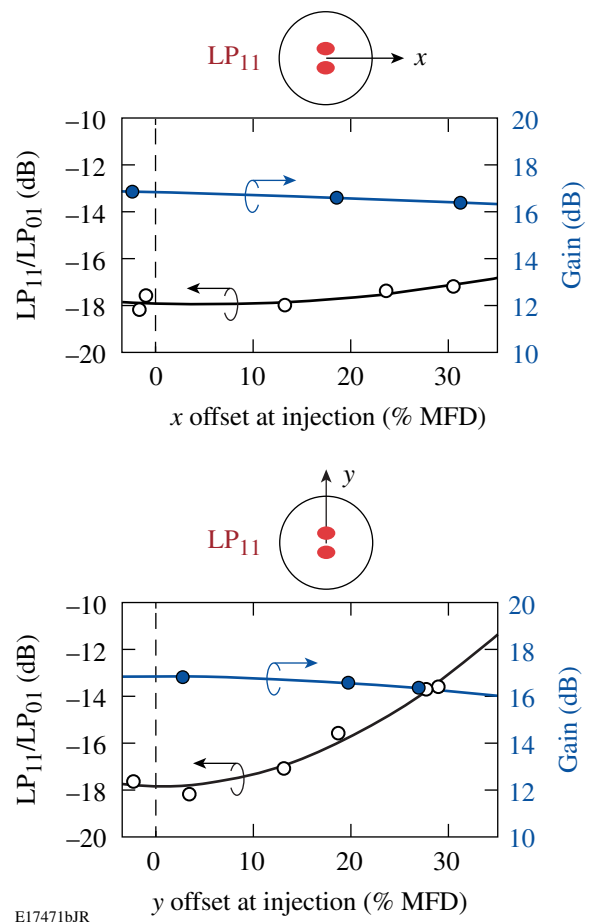
These observations raise important questions about the impact of HOM's in broadband amplifiers. When the signal bandwidth is much larger than the fringe period, deflection of the beam centroid at each wavelength will average to zero over the full spectrum. Although the integrated beam profile is broadened along the HOM axis, it is relatively insensitive to phase fluctuations between the modes. If the signal bandwidth is less than the fringe period, phase fluctuations significantly alter the integrated beam profile since there is insufficient bandwidth to average out the beam variations at each spectral component. For this amplifier, a Gaussian signal bandwidth equal to single fringe period (FWHM = 11 nm) corresponds to a 150-fs transform-limited pulse. The relative phase of the modes was stable during the S^2 scan (several minutes), in part because the fundamental mode and the HOM propagate along the same length of fiber. Long-term stability will depend on the details of the amplifier's thermal environment and stability of signal injection, so no general conclusions can be drawn from these data.

Impact of Misalignment at Signal Injection on HOM Content

The impact of misalignment at injection was evaluated by offsetting the beam with the pointing mirror (see Fig. 119.14),

using the EFM to quantify the amount of offset at signal injection, and the S^2 measurements to measure the resulting HOM content. The results are shown in Fig. 119.19. Significant amounts of LP_{11} were excited when injection was misaligned along the axis of the LP_{11} mode (the y axis). This offset direction increases the mode overlap between the input signal beam and one of the lobes of the LP_{11} mode, producing a larger fraction of the LP_{11} mode at injection. The power in LP_{11} was only -13 dB below that for LP_{01} for a $15\text{-}\mu\text{m}$ offset ($\sim 30\%$ of the MFD). The large misalignment reduced the amplifier gain by only ~ 0.5 dB.

Simulations using a simple step-index model predict that these levels of LP_{11} can have a small but measurable impact on the amplifier beam's quality. The fiber parameters were chosen to match the MFD and N.A. of the amplifier (core radius $a =$



E17471bJR

Figure 119.19
Relative power in LP_{11} mode versus injection offset. Offset along the (a) x direction (across SAP axis) and (b) the y direction (along SAP axis). Also shown is the gain in dB as a function of offset.

28 μm ; index difference $\Delta = 5.3 \times 10^{-5}$) and to set the LP₁₁ mode close to cutoff ($V = 2.50$). While these calculations did not include the full model for the PCF design or birefringence, some qualitative conclusions can be reached. Figure 119.20 shows the simulated values of beam quality (M^2) in the x and y directions plotted as a function of the ratio of LP₁₁ to LP₀₁ powers, where the LP₁₁ mode is aligned with the y axis as in Fig. 119.16(c). This orientation of LP₁₁ produces degradation of M^2 that is more severe in the y direction. The value of M_y^2 depends on the relative phase between the modes.³

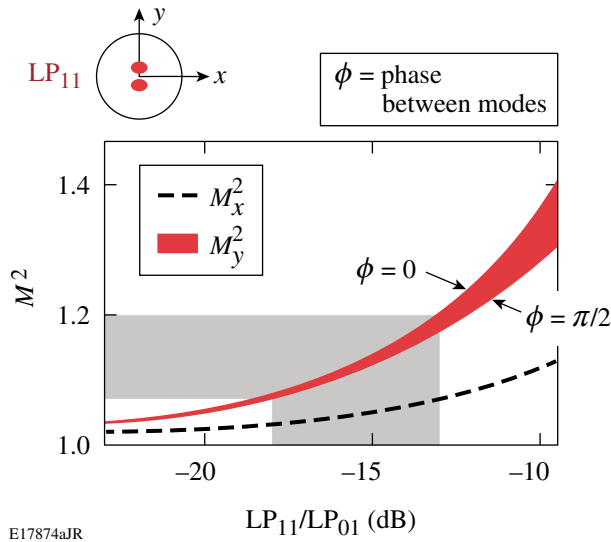


Figure 119.20 Simulations using a simple step-index model showing the impact LP₁₁ content can have on the beam quality M^2 . Results are shown along both x and y directions as a function of relative power of LP₁₁ and LP₀₁ modes. The M^2 degradation is more severe along the y direction (the axis of the LP₁₁ mode) and depends on the relative phase ϕ between the modes. The grey region shows the range of LP₁₁ content measured in the PCF amplifier and the corresponding range of M^2 values predicted by this simple model.

Measurements of M^2 show degradation when the amount of LP₁₁ is increased by misaligning the signal at injection (see Fig. 119.21). The largest increase occurs in M_y^2 (as predicted by the simulations) and when the injection offset is along the y axis (as predicted by the S^2 measurements). This is consistent with the fact that this offset direction produces the largest amount of LP₁₁. M^2 degradation from x -axis offsets cannot be explained by the level of LP₁₁ alone. It is likely that other higher-order leaky modes or spatially incoherent scattering within the amplifier that is not resolved in the S^2 measurements but can degrade M^2 are responsible.

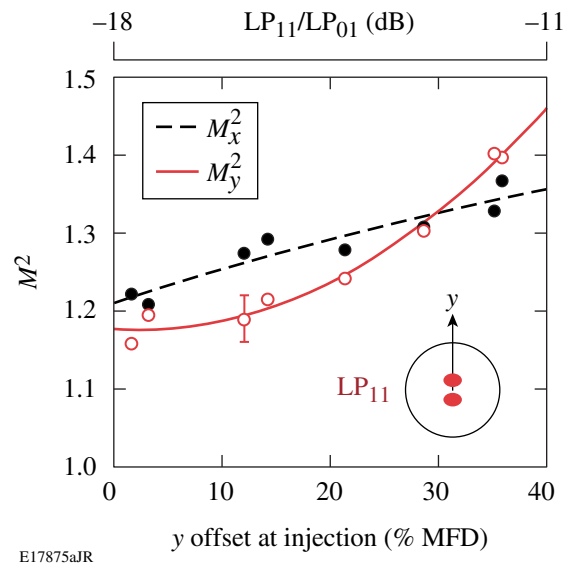
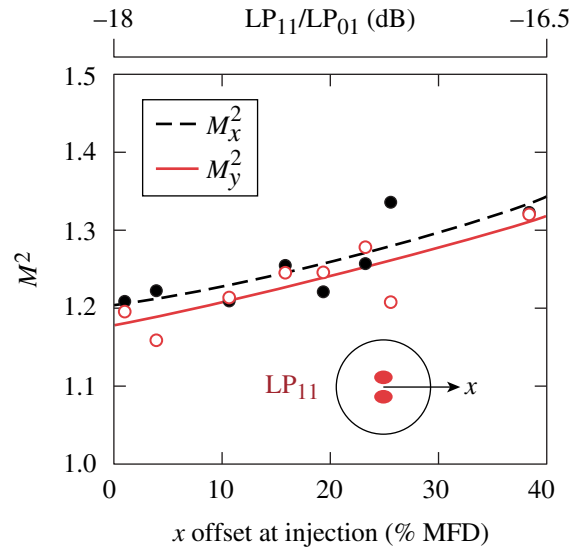


Figure 119.21 Measured M^2 for injection offsets. Offset in the (a) x direction and (b) y direction. Inset shows the offset direction relative to the orientation of the LP₁₁ mode.

In conclusion, S^2 imaging has been used for the first time to measure higher-order mode content of a large-mode-area amplifier at full power. Minor modifications to the technique were necessary to accommodate the short amplifier length and small relative group delay. An HOM corresponding to the co-polarized LP₁₁ mode was clearly observed with an axis aligned to the birefringent axis of the polarizing amplifier. The power in the LP₁₁ mode relative to the fundamental LP₀₁ mode depended on the alignment of the signal at injection. A relative power of

-18 dB was measured when optimally aligned. LP_{11} content increased when the injected beam was offset, particularly when the offset direction was toward one of the LP_{11} lobes. An offset of ~30% of the 55- μm MFD increased the LP_{11} content to -13 dB while only decreasing the amplifier gain by ~0.5 dB.

ACKNOWLEDGMENT

The authors thank Jeff Nicholson, Ingmar Hartl, and Martin Fermann for helpful discussions. This work was supported by the U.S. Department of Energy Office of Inertial Confinement Fusion under Cooperative Agreement No. DE-FC52-08NA28302, the University of Rochester, and the New York State Energy Research and Development Authority. The support of DOE does not constitute an endorsement by DOE of the views expressed in this article.

REFERENCES

1. F. Röser *et al.*, *Opt. Lett.* **32**, 3495 (2007).
2. O. Schmidt *et al.*, *Opt. Express* **16**, 3918 (2008).
3. H. Yoda, P. Polynkin, and M. Mansuripur, *J. Lightwave Technol.* **24**, 1350 (2006).
4. S. Wielandy, *Opt. Express* **15**, 15,402 (2007).
5. J. W. Nicholson *et al.*, *Opt. Express* **16**, 7233 (2008).
6. J. W. Nicholson *et al.*, *IEEE J. Sel. Top. Quantum Electron.* **15**, 61 (2009).

Optical Differentiation and Multimillijoule ~ 150 -ps Pulse Generation in a Regenerative Amplifier with a Temperature-Tuned Intracavity Volume Bragg Grating

Introduction

Optical differentiators have recently received considerable attention based on their potential application in all-optical signal-processing circuits¹ and optical pulse shaping.^{2–4} In Ref. 4 an ultrafast optical differentiator based on long-period fiber grating with subpicosecond temporal resolution was demonstrated. An ultrafast optical differentiator based on an asymmetric Mach–Zehnder interferometer was proposed in Ref. 5. An optical-differentiator operation using a GaAs/AlAs short-period super lattice near an optical absorption band edge was demonstrated in Ref. 6.

Holographic volume Bragg gratings (VBG's) represent a new class of robust, highly efficient, and spectrally selective optical elements that are recorded in photo-thermo-refractive glass.⁷ VBG's have spectral and angular dispersions that are higher than any dispersive elements previously used. VBG's are stable at elevated temperatures, have an optical damage threshold similar to that of bulk glass materials, and have high diffraction efficiency and low losses that enable one to use them in laser resonators.

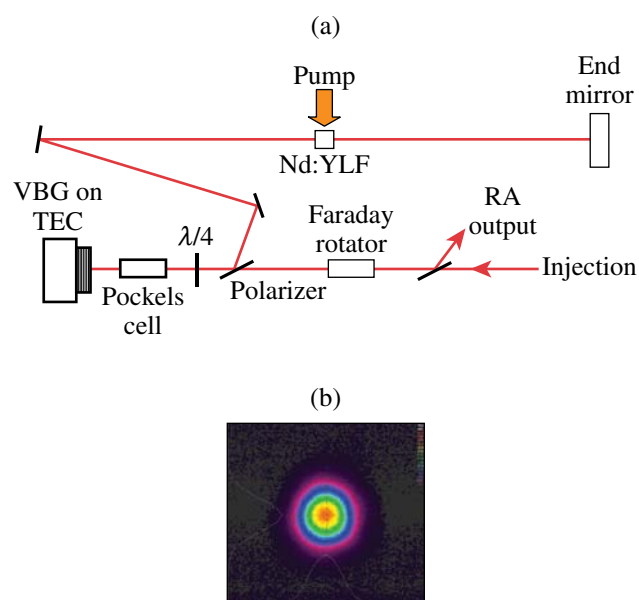
An optical differentiation in a regenerative amplifier (RA) with a temperature-tuned VBG as an intracavity spectral filter is reported for the first time. Using an RA with a VBG as a spectral filter greatly improves optical differentiator performance because of multiple passes through the filter and significant RA gain that increases differentiator efficiency and makes its practical application possible.

One of the appealing applications of an RA in differentiation mode is producing multimillijoule ~ 150 -ps pulses—important for laser–matter interaction studies and laser micromachining. Producing these pulses usually requires a mode-locked oscillator in combination with a regenerative amplifier⁸ or a Q -switched microchip laser⁹ that requires an additional amplifier because of low, <1 - μJ output-pulse energy. In this article a simple and reliable multimillijoule ~ 150 -ps laser system based on an RA operating in differentiation mode with

a temperature-tuned VBG as a resonator spectrally selective mirror is demonstrated for the first time.

Experimental Setup

The Nd:YLF diode-pumped RA shown in Fig. 119.22(a) is almost identical to the one described in Ref. 10 except that it has a longer cavity length. The RA has a folded linear cavity with a round-trip time of 21 ns, which makes it possible to amplify pulses as long as 13-ns FWHM in duration. The Nd:YLF active element was oriented for a 1053-nm operational wavelength. It was pumped by a 150-W, fiber-coupled laser diode array (Apollo Instruments, Irvine, CA), which was operated in a pulsed mode, producing 1-ms pump pulses at 805 nm with a 5-Hz repetition rate. The RA intracavity Pockels cell driven by fast electrical circuitry makes it possible to inject and cav-



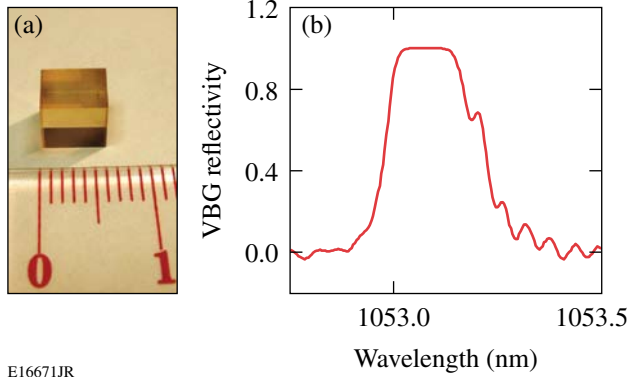
E16467aJR

Figure 119.22

(a) A Nd:YLF diode-pumped regenerative amplifier (RA) with a temperature-tuned VBG as a resonator end mirror has been demonstrated. (b) The RA output beam profile corresponds to the TEM_{00} resonator mode. TEC: thermo-electric cooler

ity dump the amplified pulse. The injected pulse was mode matched to the RA resonator and, after a certain number of round-trips, reached its maximum energy and was dumped from the RA cavity. An AR-coated, temperature-tuned VBG (OptiGrate, Orlando, FL) at a 0° angle of incidence was used [Fig. 119.23(a)]. Introducing a VBG as an RA spectrally selec-

tive mirror did not alter RA performance, owing to the VBG's high-diffraction efficiency (up to 99.7%). The VBG's high optical quality ensured RA performance in the TEM_{00} resonator mode [Fig. 119.22(b)]. The VBG bandwidth was 240-pm FWHM. The wavelength dependence of the VBG reflectivity is shown in Fig. 119.23(b). The VBG reflectivity maximum can be temperature tuned at an ~ 10 -pm/ $^\circ\text{C}$ rate. The VBG temperature was maintained with 0.1°C accuracy.



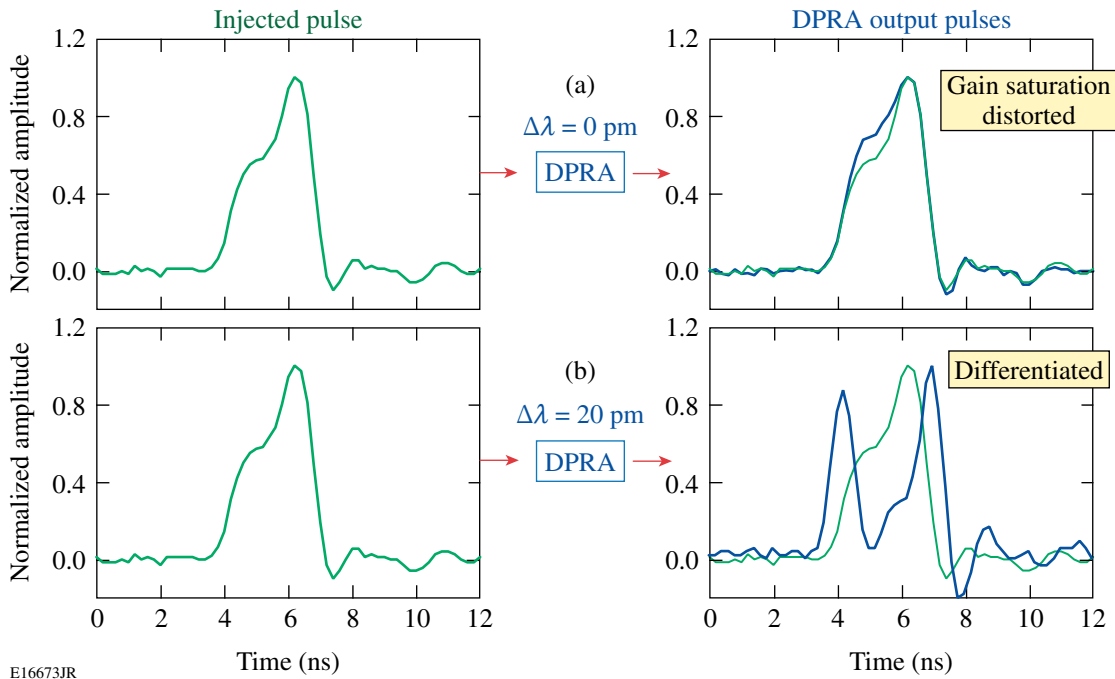
E16671JR

Figure 119.23

(a) VBG's are robust, spectrally selective optical elements that are recorded in photo-thermo-refractive glass. (b) Reflectivity of the VBG used in this experiment was 99.7% with a 240-pm FWHM bandwidth centered at 1053.08 nm.

Optical Differentiation in the RA

The 2.4-ns FWHM precompensated square pulse described in Ref. 11, which is obtained using a system that contains a stabilized single-frequency fiber laser, integrated-optic modulators, and fiber amplifier,¹² is injected into the cavity. If the VBG in the RA is tuned to the maximum of the injected pulse spectrum (shortest RA buildup time), the injected pulse is amplified, maintaining its shape with a slight distortion caused by gain saturation in the RA [see Fig. 119.24(a)]. When the VBG reflectivity is detuned by ~ 20 pm, positive feedback in the RA resonator is formed for injected pulse broadband components, and the RA performs as an optical differentiator, amplifying only rising and falling edges [Fig. 119.24(b)]. VBG peak-reflectivity detuning by 20 pm provides $\sim 0.3\%$ loss dif-

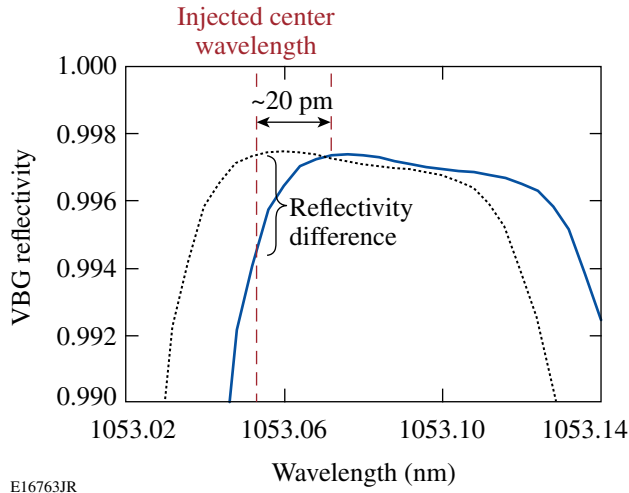


E16673JR

Figure 119.24

(a) The RA shows no peculiarities when VBG is tuned to the injected-pulse central wavelength. (b) The RA works as an optical differentiator when the VBG temperature is detuned from the injected pulse's center wavelength. Note that the gray lines in the right side output pulse are the original normalized injected pulse shape.

ference per round-trip for the injected pulse central wavelength (Fig. 119.25). The total number of round-trips in the RA is 50, which, combined with very high $\sim 10^8$ RA gross gain, causes enough discrimination that the center wavelength is not amplified, making the RA an optical differentiator.



E16763JR

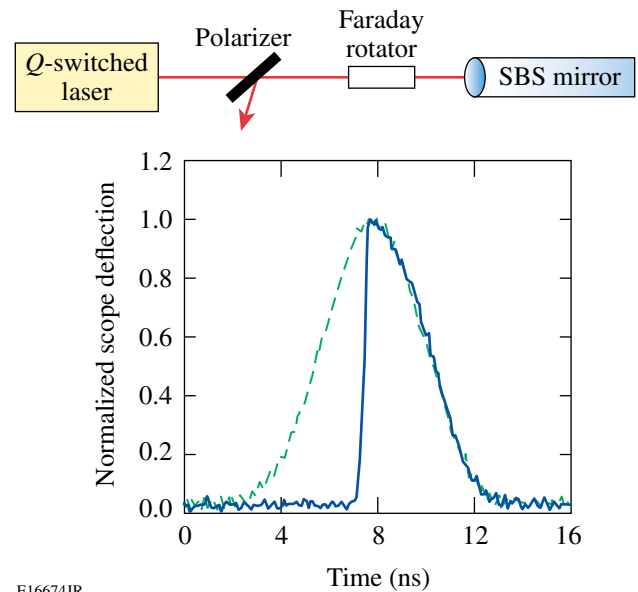
Figure 119.25
Wavelength detuning by 20 pm, which leads to a VBG reflectivity difference of $\sim 0.3\%$ per round-trip, is enough to provide differentiation in the DPR.

Generation of a Multimillijoule Picosecond Pulse in an RA in Differentiation Mode

One application of an RA as an optical differentiator is generating energetic short pulses without mode-locking. In Ref. 2 it is shown that the generation of an optical pulse with an arbitrary shape may be reduced to the problem of producing an arbitrary spectral filter. An optical differentiator is required as a spectral filter to produce a δ -function pulse. This type of filter with a quarter-wave antireflection coating in reflection mode was proposed in Ref. 2. The efficiency of this device is very low. Using an RA as an optical differentiator provides high efficiency in generating short pulses, owing to significant RA gain and multiple round-trips.

Injecting a step-like pulse is required for producing short pulses out of an RA. The output pulse width is defined by the sharp-edge duration of the injected pulse. A step-like pulse can be produced by using an air breakdown,² a fast pulse-shaping system,¹² or a stimulated Brillouin scattering (SBS) mirror.¹³ In this article, a system that consisted of a single-frequency Q -switched laser, an SBS mirror, and an RA with a VBG was used. The Q -switched laser produced 4.9-ns-

FWHM, 3-mJ TEM_{00} pulses at 1053 nm with a 5-Hz repetition rate. Output pulses were focused into an SBS cell filled with liquid carbon tetrachloride using a 60-mm-focal-length achromat (Fig. 119.26). The 3-ns-FWHM SBS-cell output pulses shown in Fig. 119.26 had a steep 300-ps leading edge, which can be made even shorter (<100 ps) by optimizing SBS cell performance.¹³ The SBS cell reflectivity was $\sim 50\%$ when the incoming pulse energy was 2.8 mJ, which was set using a half-wave plate and polarizer combination. After attenuation, an SBS-steepened pulse was launched into a single-mode, polarization-maintaining fiber and injected into the RA with a VBG. The injected pulse energy was 250 nJ.



E16674JR

Figure 119.26
A step-like pulse shape with a sharp 300-ps leading edge was produced with an SBS mirror. The dashed line is the input pulse and the solid line is the output pulse from the SBS cell.

When the maximum of the VBG reflectivity curve is tuned to the maximum of the injected pulse spectrum, the RA works in regular regime, producing the amplified up-to-12-mJ pulses shown in Fig. 119.27(a). Pulse shortening from 3-ns to 1.25-ns FWHM occurs as a result of gain saturation in the RA and the sharp leading edge of the injected pulse. When the VBG is detuned from the central wavelength by 25 pm, the RA operates as an optical differentiator and amplifies the leading-edge portion of the injected pulse, producing a 150-ps-FWHM, 12-mJ TEM_{00} pulse at 1053 nm with a 5-Hz repetition rate [Fig. 119.27(b)].

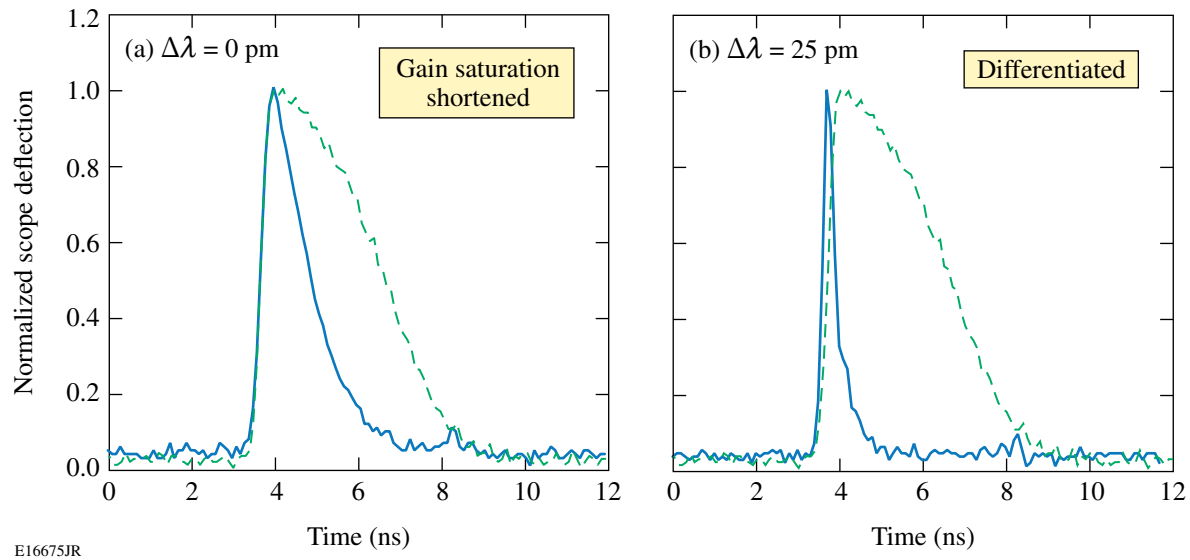


Figure 119.27

(a) The RA with a VBG tuned to the injection central wavelength produced shortened nanosecond pulses as a result of gain saturation of the step-like pulse. (b) When a VBG is temperature detuned, the RA produces 150-ps FWHM multimillijoule pulses after differentiation of a step-like pulse. The dashed line is the input pulse to the RA and the solid line is the RA output pulse shape.

Conclusion

It has been demonstrated for the first time that a regenerative amplifier with a temperature-tuned volume Bragg grating as a spectrally selective resonator mirror works as an optical differentiator when the VBG reflection peak is detuned from the central laser wavelength. A simple, reliable laser system that produces multimillijoule ~ 150 -ps pulses without mode-locking using an RA with a VBG as an optical differentiator has been realized.

ACKNOWLEDGMENT

This work was supported by the U.S. Department of Energy Office of Inertial Confinement Fusion under Cooperative Agreement No. DE-FC52-08NA28302 and the University of Rochester. The support of DOE does not constitute an endorsement by DOE of the views expressed in this article.

REFERENCES

1. N. Q. Ngo *et al.*, *Opt. Commun.* **230**, 115 (2004).
2. E. Yablonovitch, *IEEE J. Quantum Electron.* **11**, 789 (1975).
3. M. Kulishov and J. Azaña, *Opt. Lett.* **30**, 2700 (2005).
4. R. Slavík *et al.*, *Opt. Express* **14**, 10,699 (2006).
5. Z. Li *et al.*, in *Proceedings Symposium IEEE/LEOS Benelux Chapter*, edited by A. M. J. Koonen *et al.* (IEEE, Eindhoven, The Netherlands, 2006), pp. 173–176.
6. M. Hosoda *et al.*, *Appl. Phys. Lett.* **65**, 2913 (1994).
7. L. B. Glebov *et al.*, in *Laser Weapons Technology III*, edited by W. E. Thompson and P. H. Merritt (SPIE, Bellingham, WA, 2002), Vol. 4724, pp. 101–109.
8. W. Koechner, *Solid-State Laser Engineering*, 4th rev. ed., Springer Series in Optical Sciences, Vol. 1 (Springer, Berlin, 1996).
9. G. J. Spühler *et al.*, *J. Opt. Soc. Am. B* **16**, 376 (1999).
10. A. V. Okishev and J. D. Zuegel, *Appl. Opt.* **43**, 6180 (2004).
11. A. V. Okishev, C. Dorrer, V. I. Smirnov, L. B. Glebov, and J. D. Zuegel, *Opt. Express* **15**, 8197 (2007).
12. J. R. Marciante and J. D. Zuegel, *Appl. Opt.* **45**, 6798 (2006).
13. M. D. Skeldon, A. Okishev, A. Babushkin, and W. Seka, in *First Annual International Conference on Solid State Lasers for Application to Inertial Confinement Fusion*, edited by M. André and H. T. Powell (SPIE, Bellingham, WA, 1995), Vol. 2633, pp. 422–429.

Slow Crack Growth During Radiative Cooling of LHG8 and BK7 Plates

Introduction

Because of their low resistance to fracture and low thermal conductivity, many ceramics and glasses are susceptible to thermal shock. A common thermal shock configuration consists of a component at an initially uniform high temperature suddenly exposed to a cooling medium at a lower temperature. The more-rapid temperature decrease at the surface induces a tensile stress, while the component's interior is in a state of compression. Kingery^{1,2} has discussed in detail the effects of material and cooling medium properties on thermal shock. The relevant figures of merit governing thermal shock have been reviewed by Hasselman³ and Wang and Singh.⁴

Depending on the thermal conductivity of the component, its dimensions, and the heat transfer coefficient induced by the cooling medium, there may exist a state of "severe" thermal shock (where the tensile thermal stresses at the component surface depend only on the material's thermomechanical properties) or "mild" thermal shock (where the surface tensile stresses depend on the material's thermomechanical properties and the Biot number, involving the cooling heat transfer coefficient, specimen size, and component thermal conductivity). The heat transfer coefficient itself depends on the flow between the component and the cooling medium (forced or natural), the dimensions of the component, and the cooling medium's thermophysical properties (viscosity, density, and thermal diffusivity). The conditions for severe or mild thermal shock along with an extensive discussion of the contributions of the thermomechanical properties can be found in Refs. 5–7.

Since the Biot number is an important factor in determining the severity of thermal shock, ceramics and glasses behave differently under thermal shock conditions. Ceramics have higher thermal conductivity and, therefore, lower Biot numbers, leading to conditions prone to mild thermal shock. Glasses, on the other hand, have a low thermal conductivity and are thus liable to severe thermal shock. A large amount of work exists in the literature on thermal shock of ceramics^{3–9} but less on thermal shock of glasses.¹⁰

This article discusses the radiative cooling of two optical glasses: the borosilicate crown BK7 and the phosphate LHG8. Under radiative cooling conditions, the usual thermal shock analysis does not apply because the surrounding temperature continuously changes with time as does the heat transfer coefficient (and thus the Biot number). We determine the relevant thermal and stress fields numerically using finite elements and then use these results to study crack growth at the heaviest stressed locations. We discuss fracture in terms of strength, fracture toughness, and slow crack growth under transient temperature and stress fields.

Material Properties

The two materials investigated here are the borosilicate crown glass BK7, a commonly used optical glass, and the phosphate glass LHG8 often used in laser applications. The glass properties are listed in Table 119.II.

We observe that LHG8 is about twice as brittle in terms of fracture toughness K_c as BK7, while it is also twice as soft. In Table 119.II, we have also calculated the fracture strength for these glasses, assuming different sizes of initial flaw size into the surface. Table 119.II gives a range for the fracture toughness of LHG8. The higher value ($0.51 \text{ MPa}\sqrt{\text{m}}$) is cited in Campbell *et al.*,¹¹ while the lower value ($0.43 \text{ MPa}\sqrt{\text{m}}$) is cited in DeGroote *et al.*¹² Notice, however, that a typical uncertainty in K_c is $\pm 10\%$. In this sense, these measurements agree.

Suratwala *et al.*¹³ have measured the slow crack growth in LHG8 using the double-cleavage-drilled-compression method. They showed that the rate of crack growth v depends on the amount of OH concentration in the glass. They reported data in the temperature range of 25°C to 300°C and water vapor pressure in the range of 2 to 92 mmHg. These data can be fitted by

$$v = \frac{v_I v_{II}}{v_I + v_{II}} \quad (1)$$

Table 119.II: Material properties of the two glasses studied.

Property and Units	BK7	LHG8
Density ρ , kg/m ³	2510	2830
Heat capacity cp, J/kg.K	858	750
Thermal conductivity k , W/m.K	1.114	0.58
Thermal diffusivity D , m ² /s	5.2×10^{-7}	2.7×10^{-7}
Young's modulus E , GPa	82	50
Poisson ratio ν	0.21	0.26
CTE α , K ⁻¹	8.3×10^{-6}	12.7×10^{-6}
Fracture toughness K_{Ic} , MPa \sqrt{m}	0.82	0.43 to 0.51
Fracture strength, MPa (assumes scratch a is 50 μ m deep)	59	31 to 36
Fracture strength, MPa (assumes scratch a is 500 μ m deep)	19	10 to 12
Fracture strength, MPa (assumes scratch a is 1000 μ m deep)	13	7 to 8
Hardness, GPa	6.8 \pm 0.3	3.4

with

$$v_I = v_0 \left(\frac{p_{H_2O}}{p_0} \right)^m \exp \left(\frac{K_{app} b - Q_I}{RT} \right), \tag{2}$$

$$v_{II} = C \frac{p_{H_2O}}{p_0} \exp \left(\frac{-Q_{II}}{RT} \right),$$

where p_0 is the atmospheric pressure 760 mmHg. The parameters are listed in Table 119.III. The subscripts I and II correspond to region I (stress controlled) and region II (diffusion controlled) crack growth.^{13,14} The harmonic mean in Eq. (1) essentially selects the lower of v_I , v_{II} . Notice that the applied stress intensity factor K_{app} affects the crack growth rate v_I (but not v_{II}).

For the case of a quarter circular crack at the edge of a plate under tension, the applied stress intensity factor is

$$K_{app} = \Omega \sigma_{app} \sqrt{\pi a}, \tag{3}$$

where Ω is a geometrical factor (~ 0.80), σ_{app} is the applied tension, and a is the crack depth (see Lambropoulos *et al.*¹⁵ for the geometrical factor Ω describing a quarter circular crack along an edge).

For the case of BK7, we used the data of Wiederhorn and Roberts,¹⁴ who measured slow crack growth in BK7 and other glasses with a double cantilever beam technique. They reported data for BK7 at temperatures of 23°C, 104°C, 154°C, and 226°C under vacuum (10^{-5} Torr), as well as for BK7 in air and RT under 100% RH.

Table 119.III: Data for slow crack growth in LHG8 from Suratwala *et al.*¹³

Parameter	Units	LHG8-L (128-ppmw OH)	LHG8-H (773-ppmw OH)
v_0	10 ⁶ m/s	7.3	7.3
m	dimensionless	1.20	1.20
Q_I	kJ/mol	253	239
b	m ^{5/2} /mol	0.48	0.48
C	m/s	180	180
Q_{II}	kJ/mol	26	26

For numerical computation, we have fitted the data at the crack growth rates of 10^{-5} m/s, 10^{-6} m/s, and 10^{-7} m/s for these four temperatures. We fitted these data to the form

$$v_I = v_0 \exp\left(\frac{K_{app} b - Q}{RT}\right) \quad (4)$$

by a numerical procedure that minimized the error, defined as

$$\%error(v_0, b, Q) = 100 \times \frac{\sum_1^{12} [\ln v(v_0, b, Q) - \ln v_i]^2}{\sum_1^{12} (\ln v_i)^2} \quad (5)$$

The best fit gave a minimum error of 0.62% and corresponded to the parameters

$$\begin{aligned} \ln v_0 &= 10.10, \\ b &= 0.21 \text{ m}^{5/2}/\text{mol}, \\ Q &= 227.5 \text{ kJ/mol}, \end{aligned} \quad (6)$$

describing the slow crack growth of BK7 at “vacuum” conditions. These data will be used to predict crack growth in BK7 under vacuum conditions.

Finite Element Analysis: Temperature and Stress

Both materials modeled are in the form of rectangular plates with an areal extent of $800 \times 400 \text{ mm}^2$. The BK7 plates are 80 mm thick; the LHG8 plates are 40 mm thick. These dimensions will be consistent throughout the remainder of our work. The BK7 and LHG8 thicknesses are different because thermal stress is known to scale with thickness, while LHG8 is less strong than BK7. In a sense, therefore, the stronger BK7 plates are more severely stressed than the thinner LHG8.

The plate was initially placed in an oven at a uniform high temperature. The oven temperature slowly diminished with time, so that all six sides of the plate underwent radiative cooling into an ambient whose temperature changed with time. In both cases of LHG8 and BK7, it was assumed that the initial temperature was uniform and equal to a high value of 200°C . The surroundings’ (ambient) temperature decayed exponentially with a time constant τ that may vary from minutes to hours to days. The eventual temperature was room temperature, again taken as uniform (see Fig. 119.28).

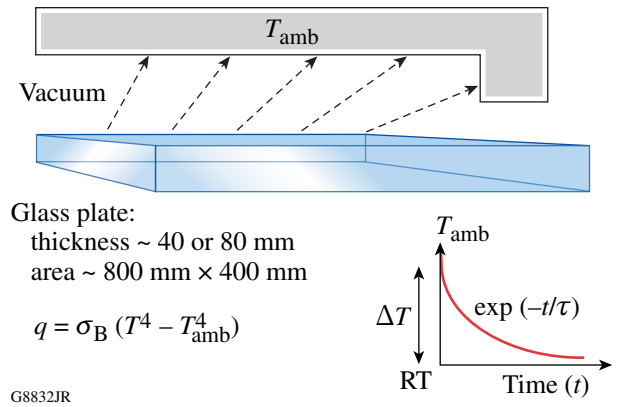


Figure 119.28 The geometry of a thin plate cooled by radiation. The ambient temperature decayed exponentially from the initial temperature of 200°C to the final temperature (RT) with a time constant τ .

The coordinate system was centered at the plate’s center, with $-400 \text{ mm} < y < 400 \text{ mm}$, $-200 \text{ mm} < x < 200 \text{ mm}$, and the coordinate z varying $-20 \text{ mm} < z < 20 \text{ mm}$ for LHG8 or $-40 \text{ mm} < z < 40 \text{ mm}$ for BK7.

The boundary condition on all six edges of the glass plate was taken as radiating into a medium of ambient temperature $T_{amb}(t)$, i.e.,

$$q \left[\text{W}/\text{m}^2 \right] = \sigma_B (T^4 - T_{amb}^4), \quad (7)$$

where σ_B is the Boltzmann constant $5.67 \times 10^{-8} \text{ W}/(\text{m}^2 \cdot \text{K}^4)$, T is the absolute temperature at the glass surface, and T_{amb} is the (time-dependent) temperature of the surroundings (ambient), taken to vary as

$$T_{amb}(t) = 293 + 180 \exp(-t/\tau), \quad (8)$$

where the time constant τ models the rate at which the surroundings temperature decays with time. The ambient temperature drops from 200°C to 86°C in time τ and to 29°C in time 3τ . The initial condition is

$$T(x, y, z, t = 0) = 473 \text{ K}. \quad (9)$$

The temperature $T(x, y, z, t)$ is governed by the time-dependent, 3-D heat conduction equation. A typical temperature evolution is shown in Fig. 119.29.

Once the temperature was determined, the stresses were calculated by using COMSOL® (version 3.4).¹⁶ We note some

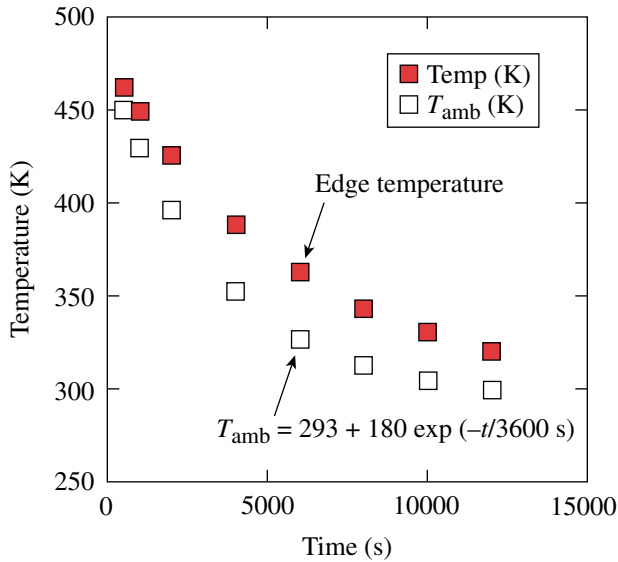


Figure 119.29
Temperature evolution along the edge center of the long edge in a 40-mm-thick LHG8 plate. The temperature relaxation constant $\tau = 1$ h. The ambient temperature is also shown.

features of the resulting stress distribution: At early times, the temperature was high but mostly uniform; therefore the thermal stress was very small. At long times, the temperature was low and again mostly uniform; therefore the thermal stress was also low. As a result, the thermal stress became largest at some intermediate time. An example of stress evolution along the center of the long edge is shown in Fig. 119.30.

We also observed that the Biot number was neither small nor very large. To extract an applicable heat transfer coefficient h_{eff} , we linearized the surface-cooling constitutive law to read

$$q[\text{W}/\text{m}^2] = 4\sigma_B T_{\text{amb}}^3 (T - T_{\text{amb}}) = h_{\text{eff}} (T - T_{\text{amb}}). \quad (10)$$

Evaluating h_{eff} at $T_{\text{amb}} = 473$ K or at 300 K, we found that h_{eff} was in the range of 24 to 26 W/m².K, so that the Biot number

$$\text{Bi} = h_{\text{eff}} L/k \quad (11)$$

(with $2L$ as the plate thickness) was in the range of 0.2 to 0.8 for LHG8 and 0.2 to 0.9 for BK7. We concluded that the temperature gradients in the plate cannot be neglected and indeed must explicitly be accounted for.

Notice that if h_{eff} were very large (i.e., if $\text{Bi} \gg 1$, corresponding to very rapid quenching by ΔT), the surface thermal stress would be

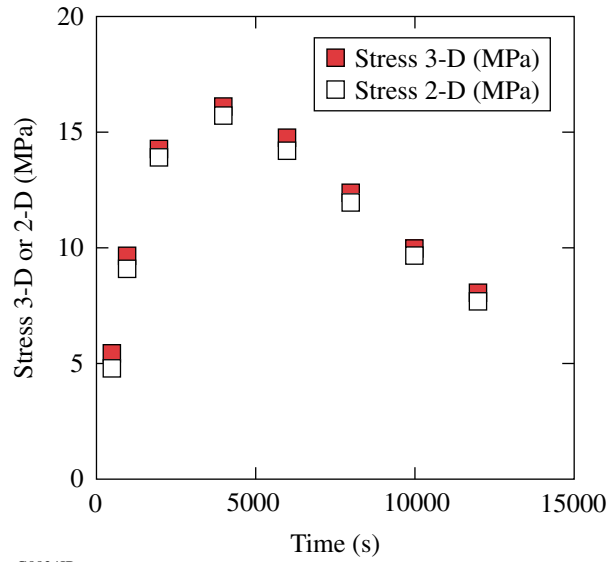


Figure 119.30
Thermal stress evolution along the edge center of the long edge in a 40-mm-thick LHG8 plate. The temperature relaxation constant $\tau = 1$ h. For short times, the temperature was high and uniform, so the thermal stress was low. These results show the thermal stress calculated via 3-D or 2-D (plane-strain) approaches. Both approaches give similar stress levels.

$$\sigma_{\text{max}} = \frac{\alpha E \Delta T}{1 - \nu} \quad (12)$$

with ΔT representing the temperature drop (here 180°C), α the coefficient of thermal expansion, and E the Young's modulus. This estimate would give a stress of about 150 MPa for either BK7 or LHG8, i.e., a stress significantly higher than the strength of the glass (see Table 119.II). The fact, however, that the applicable Biot number Bi is of the order of 1 means that such estimates of stress as in Eq. (12) are not applicable and stresses must be explicitly computed.

Figure 119.31 shows the stress distribution in LHG8 cooled at the rate $\tau = 4$ h. The long and intermediate edges of the plate were the most highly stressed. Figure 119.32 compares directly the evolution of temperature and stress at the center of the long edge for a plate of LHG8 and a plate of BK7. Strong size effects (i.e., increasing stresses with increasing plate thickness) and rate effects (i.e., stresses increasing with more-rapid cooling), from extensive stress calculations by finite element methods, are shown for LHG8 in Fig. 119.33.

We will next determine how a surface flaw in the most heavily stressed area (the center of the long edges) will grow as the temperature and stress evolve at that point. To examine

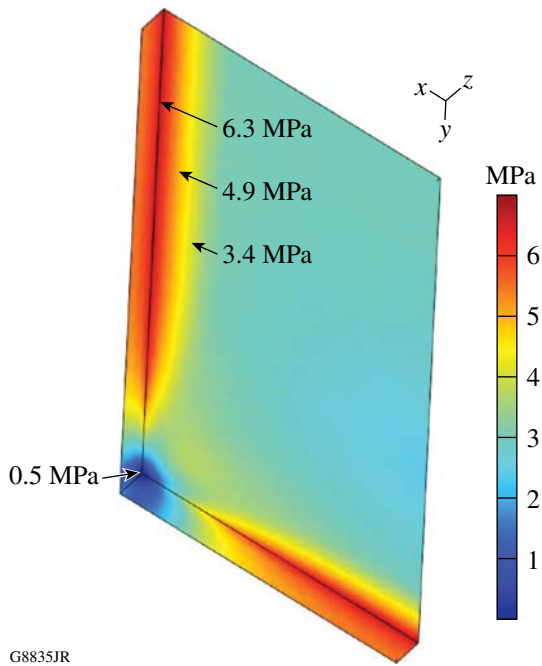
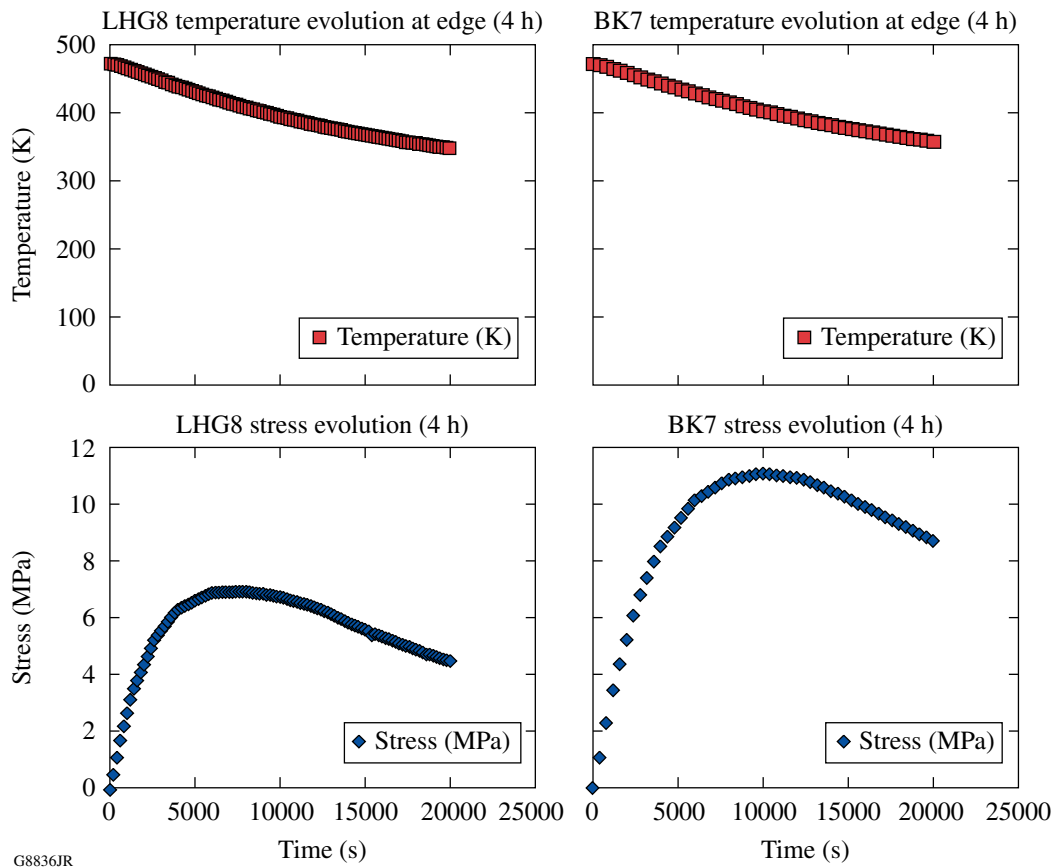


Figure 119.31
 Thermal stress distribution at time $t = 8000$ s (about 2.2 h) in a 40-mm-thick LHG8 plate. Only 1/8 of the plate is shown. The plot shows the maximum principal stress, at a time when the thermal stress at the edge was close to maximum. The temperature relaxation constant $\tau = 4$ h. The long edges at $x = \pm 200$ mm, $y, z = \pm 20$ mm and intermediate edges at $x, y = \pm 400$ mm, $z = \pm 20$ mm were in a state of tension of magnitude 6.9 MPa. The plate's long edges and intermediate edges were similarly stressed and the stresses at these locations were the highest.

G8835JR



G8836JR

Figure 119.32
 The evolution of temperature at the center of the long edge and the stress at the same point for plates of LHG8 (40 mm thick) and BK7 (80 mm thick). In both cases, the time constant for the oven temperature decay was $\tau = 4$ h.

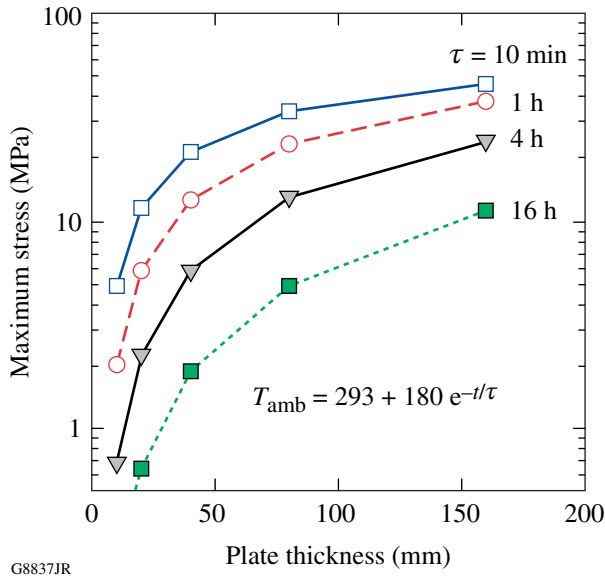


Figure 119.33 The maximum thermal stress (occurring at the center of the long plate edges) depends on the plate thickness and the rate at which the ambient temperature decays. These results are for the case of LHG8 glass plates. Thicker plates lead to larger stresses, as do more-rapid temperature cooling rates.

crack growth we need two auxiliary results: first, the depth of the initial flaw in the glass long edge (a figure to be estimated from the abrasive size used to finish that edge); second, a way of describing crack growth, from that initial crack depth value, as temperature and stress evolve with time.

It is important here to keep distinct the terminology of the various types of cracks resulting from finishing the plate surfaces. By subsurface damage (SSD) we mean the average flaw depth, a quantity that can be estimated from the abrasive used to finish that edge or from the peak-to-valley roughness at that point. This is different from the deepest flaw size $\langle c \rangle_{\max}$, which will control the strength at that point.

We have shown in previous work on glasses and crystals¹⁷ that the subsurface damage can be estimated from the abrasive used to finish a surface by

$$SSD \sim 2 \times (\text{abrasive size}). \quad (13)$$

On the other hand, Suratwala *et al.*¹⁸ have shown that the maximum flaw depth in fused silica is about 8× the average flaw depth:

$$\langle c \rangle_{\max} \sim 8 \langle c \rangle_{\text{av}}. \quad (14)$$

By identifying the average crack depth $\langle c \rangle_{\text{av}}$ with the subsurface damage SSD, we arrive at

$$\langle c \rangle_{\max} \sim 16 \times (\text{abrasive size}). \quad (15)$$

For example, when finishing with 15- μm abrasives, one would expect a 240- μm flaw depth into the glass surface.

Notice here that the relation between average and deepest flaw size in Eq. (14) was measured¹⁸ for the case of fused silica and its applicability to LHG8 and BK7 is not known. On the other hand, these estimates are for finishing flat surfaces. Given the fact that the area most heavily stressed is the edge of the plate (i.e., the intersection of two flat surfaces), it is again not entirely clear how to extend Eqs. (13)–(15) to our case. In any case, we must keep these caveats in mind while estimating the deepest flaw at the edge by Eq. (15).

Cracking in LHG8 Versus BK7

For fracture in radiatively cooled BK7 and LHG8 plates, we adopted several different approaches. In the strength approach, fracture was taken to occur when the applied stress σ_{app} reached the fracture strength of the glass σ_F . Therefore, for safe operation, we required

$$\sigma_{\text{app}} < \sigma_F \Rightarrow \text{safe}. \quad (16)$$

For a typical glass, the figure of merit for strength is about 50 MPa. As shown in Table 119.II, the strength of LHG8 is 10 MPa, while the strength of BK7 is 20 MPa. The applied stresses are shown in Fig. 119.32. For LHG8 the maximum stress is 7 MPa, while for BK7 it is 11 MPa. The conclusion is that, based on the strength approach, both LHG8 and BK7 are safe under these cooling conditions.

The main drawback of this approach is that the strength of a glass surface is not a well-described quantity. This drawback is addressed by using the fracture toughness approach.

In the fracture toughness approach, cracking will occur when the applied stress intensity factor K_{app} reaches the material's fracture toughness for a given flaw size. The applied stress intensity is given by Eq. (3). Therefore, for safe operation, we require

$$K_{\text{app}} = \Omega \sigma_{\text{app}} \sqrt{(\pi a)} < K_c, \quad \text{or } a < \frac{1}{\pi} \left(\frac{K_c}{\Omega \sigma_{\text{app}}} \right)^2. \quad (17)$$

For a quarter circular crack along an edge, $\Omega = 0.80$ (Ref. 15). Using $K_c = 0.43$ to $0.51 \text{ MPa}\sqrt{\text{m}}$ for LHG8 and $\sigma_{\text{app}} = 7 \text{ MPa}$ (from Fig. 119.32), we conclude that any flaw size more shallow than 1.9 to 2.7 mm is safe. Repeating for BK7 with $\sigma_{\text{app}} = 11 \text{ MPa}$ from Fig. 119.32, we find that any flaw size $a < 2.8 \text{ mm}$ is safe.

The drawback of the fracture toughness approach is that it assumes that the fracture toughness is a property that is independent of temperature.

For the slow crack growth approach, crack growth evolves according to

$$\frac{da}{dt} = F\{K_{\text{app}}[a(t)], T(t)\}, \quad (18)$$

$$K_{\text{app}}(t) = \Omega \sigma_{\text{app}}(t) \sqrt{\pi a(t)}, \quad (19)$$

where the function F is given by Eq. (1) or (4), and the stress $\sigma_{\text{app}}(t)$ and temperature $T(t)$ are shown in Fig. 119.32.

The data for LHG8 were modeled with the following parameters (see **Material Properties**, p. 145):

$$\begin{aligned} v_0 &= 7.3 \times 10^6 \text{ m/s}, \\ b &= 0.48 \text{ m}^{5/2}/\text{mol}, \\ Q_1 &= 239 \text{ kJ/mol} \end{aligned} \quad (20)$$

(corresponding to LHG8 with higher OH concentration and, therefore, greater propensity for cracking). It is also important here to note that although the fit in Eq. (2) is for any pressure and the pressure in the oven is “vacuum,” we have used the slowest experimental data reported,¹⁴ i.e., we have taken $p_{\text{H}_2\text{O}} = 2 \text{ mmHg}$.

For the case of BK7, we repeat the procedure for F given by Eq. (4) with

$$\begin{aligned} v_0 &= 2.4 \times 10^4 \text{ m/s}, \\ b &= 0.21 \text{ m}^{5/2}/\text{mol}, \\ Q_1 &= 227.5 \text{ kJ/mol}. \end{aligned} \quad (21)$$

In both cases, the crack growth rate depends on the depth of the initial flaw size. If the initial crack depth is too deep, the crack will grow catastrophically at some time, leading to a complete fracture of the plate. We have numerically determined an initial flaw size that is just below this critical condition.

Figure 119.34 shows the critical growth condition for LHG8. The initial crack size was about $970 \mu\text{m}$. Any crack size deeper than this will lead to catastrophic failure of the plate. It is seen that crack growth has three regions: For early times, there is little growth because the thermal stress is low. For very long times, crack growth is also low because the temperature is low. For intermediate times, however, crack growth is appreciable because both stress and temperature are sufficiently high. For the case of LHG8, the final crack size will be about $1200 \mu\text{m}$, but the plate will not fail catastrophically.

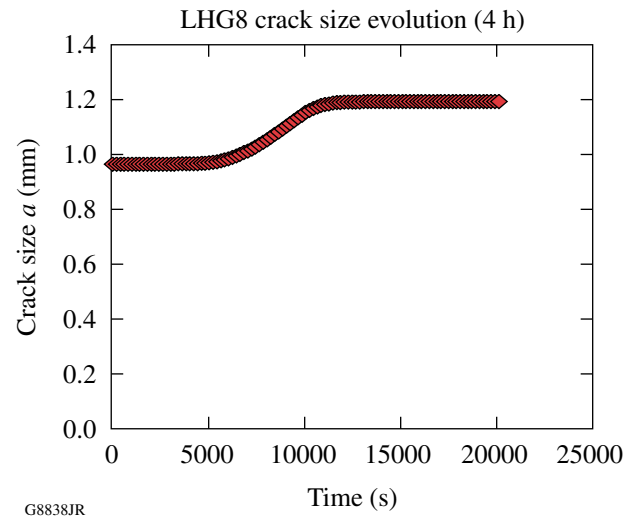


Figure 119.34 Crack growth in the center of the long edge of a 40-mm-thick LHG8 plate. The initial flaw size was $970 \mu\text{m}$. Any flaw size deeper than this will lead to catastrophic failure.

A similar analysis for the BK7 plate leads to the conclusion that for BK7 the critical initial flaw depth was $1650 \mu\text{m}$.

The predicted crack growth rate for LHG8 is shown in Fig. 119.35. Notice that there is an initial incubation period (temperature was high but stresses were low) and a final period at which crack growth stopped (the temperature was too low). The crack growth rate was largest, about 50 to 60 nm/s, for intermediate times where both temperature and stresses were significant; indeed, this was slow crack growth.

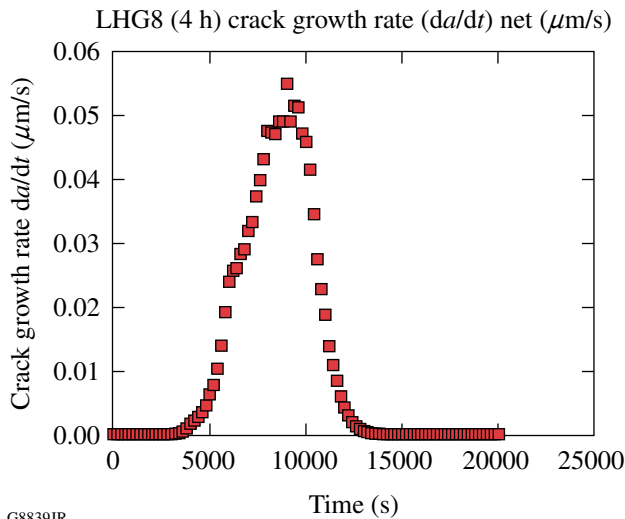


Figure 119.35
 Predicted crack growth rate at the midpoint of the long edge of a 40-mm-thick LHG8 plate. The initial flaw size was 970 μm . Any flaw size deeper than this will lead to catastrophic failure.

We observe that although BK7, being twice as thick as LHG8, has higher thermal stresses, it has slower crack growth behavior and can tolerate cracks up to 1650 μm along the center of its long edge. LHG8 can tolerate cracks only up to 970 μm .

The slow crack growth approach incorporates crack growth as a function of temperature and applied stress; in other words, the material properties' dependence on temperature.

Conclusions

Several conclusions may be drawn from our work. First, 40-mm-thick LHG8 plates are inherently weaker than 80-mm-thick BK7 plates. This is a non-obvious conclusion because, in general, thicker plates are subjected to higher stresses.

Second, for both LHG8 and BK7, the most adversely stressed areas are the midpoints of the long edges, and there are strong size and rate effects in the buildup of thermal stress during radiative cooling. If all edges have similar crack distributions following finishing, the midpoints of these long edges would then be critical areas of crack growth because they are the most highly stressed.

The third conclusion concerns the choice of the fracture approach. The strength approach is inadequate because strength of a glass surface, let alone of a glass edge, is a parameter that depends on many finishing parameters so that it can hardly be

seen as a material property. Even if one could identify a strength value, the case study in the previous section shows that the strength approach would predict that both the LHG8 and BK7 plates would be safe. If anything, the fracture toughness and slow crack growth approaches show that this is not the case.

The fracture toughness approach is a "liberal" criterion, predicting that the worst allowable flaw size in LHG8 would be in the range of 1.9 to 2.7 mm and for BK7 about 2.8 mm.

The slow crack growth criterion is more conservative. It predicts that for LHG8 the worst allowable initial flaw is 0.97 mm deep, while for BK7 it is 1.65 mm.

ACKNOWLEDGMENT

This work was supported by the U.S. Department of Energy Office of Inertial Confinement Fusion under Cooperative Agreement No. DE-FC52-08NA28302, the University of Rochester, and the New York State Energy Research and Development Authority. The support of DOE does not constitute an endorsement by DOE of the views expressed in this article.

REFERENCES

1. W. D. Kingery, *J. Am. Ceram. Soc.* **38**, 3 (1955).
2. W. D. Kingery, H. K. Bowen, and D. R. Uhlmann, *Introduction to Ceramics*, 2nd ed., Wiley Series on the Science and Technology of Materials (Wiley, New York, 1976), Secs. 16.1–16.3.
3. D. P. H. Hasselman, *Ceram. Bull.* **49**, 1033 (1970).
4. H. Wang and R. N. Singh, *Int. Mater. Rev.* **39**, 228 (1994).
5. D. P. H. Hasselman, *J. Am. Ceram. Soc.* **52**, 600 (2006).
6. J. P. Singh, J. R. Thomas, and D. P. H. Hasselman, *J. Am. Ceram. Soc.* **63**, 140 (2006).
7. H. Hencke, J. R. Thomas Jr., and D. P. H. Hasselman, *J. Am. Ceram. Soc.* **67**, 393 (2006).
8. A. G. Tomba-Martinez and A. L. Cavalieri, *J. Am. Ceram. Soc.* **85**, 921 (2002).
9. A. G. Tomba-Martinez and A. L. Cavalieri, *J. Eur. Ceram. Soc.* **21**, 1205 (2001).
10. O. Peitel and E. D. Zanotto, *J. Non-Cryst. Solids* **247**, 39 (1999).
11. J. H. Campbell and T. I. Suratwala, *J. Non-Cryst. Solids* **263 & 264**, 318 (2000).
12. J. E. DeGroot, A. E. Marino, J. P. Wilson, A. L. Bishop, J. C. Lambropoulos, and S. D. Jacobs, *Appl. Opt.* **46**, 7927 (2007).
13. T. I. Suratwala *et al.*, *J. Non-Cryst. Solids* **263 & 264**, 213 (2000).

14. S. M. Wiederhorn and D. E. Roberts, Institute for Materials Research, National Bureau of Standards, Washington, DC, NBS Report 10892, NASA PR 1-168-022, T-5330A (1972).
15. J. C. Lambropoulos, H. Liu, and Y. Wu, "Thermal Shock and Post-Quench Strength of Lapped Borosilicate Optical Glass," to be published in the *Journal of Non-Crystalline Solids*. See also: Y. Zhang, Y. Wu, H. Liu, and J. C. Lambropoulos, in *Optical Manufacturing and Testing VII*, edited by J. H. Burge, O. W. Faehnle, and R. Williamson (SPIE, Bellingham, WA, 2007), Vol. 6671, p. 66710H.
16. COMSOL® and COMSOL Multiphysics® are registered trademarks of COMSOL AB, Tegnérgatan 23, SE-111 40 Stockholm, Sweden.
17. J. A. Randi, J. C. Lambropoulos, and S. D. Jacobs, *Appl. Opt.* **44**, 2241 (2005).
18. T. Suratwala *et al.*, *J. Non-Cryst. Solids* **352**, 5601 (2006), see p. 5615, Fig. 15.

Finite Element Simulation of Metal–Semiconductor–Metal Photodetector

Introduction

Low-temperature-grown GaAs (LT-GaAs), deposited by molecular beam epitaxy, has been known for its ultrashort, subpicosecond photocarrier lifetime and relatively high carrier mobility. Therefore, in recent years LT-GaAs has been the material of choice for the fabrication of photonic devices such as photoconductive switches,^{1,2} both of the metal–semiconductor–metal (MSM)³ and freestanding types,⁴ for the generation of subpicosecond electrical pulses for ultrafast device characterization,⁵ THz time-domain spectroscopy,⁶ antennas for the generation and detection of THz radiation,⁷ as well as for optical photomixers.^{8,9}

Much effort has gone into achieving high efficiency for LT-GaAs material and the design of optimal geometries for the device structures; however, further performance improvement of LT-GaAs-based photonic devices is expected by optimizing the device contacts. Historically, LT-GaAs MSM's have been constructed with electrodes consisting of surface-contact metallization such as, e.g., Ni-Au, Ti-Au, or Ti-Pd-Au.¹⁰ For decades the properties of metal contacts to III–V semiconductors have been intensively studied.^{11,12} From these studies it is well known that a contact metallization that creates Schottky contacts on conventional *n*-doped GaAs shows ohmic behavior on LT-GaAs, even without annealing.¹⁰ The annealing of contacts to LT-GaAs is restricted to temperatures below 600°C since higher temperatures lead to a drastic change in the properties of the LT-GaAs material itself. The speed of response for the ohmic-type MSM photodetector is generally limited by the carrier lifetime, which in the case of LT-GaAs is so short (~150 fs) that the device capacitance sets the practical limit. Unfortunately, the ultrashort carrier lifetime translates into relatively low mobility of the LT-GaAs material, resulting in low-efficiency LT-GaAs devices, as compared to other photodetectors, such as *p-i-n* diodes.¹³ Recently, however, MSM devices with alloyed^{12,14} and recessed^{9,15} electrodes have been found to exhibit improved performance through optimization of the device contacts. Reference 14 reported a twofold improvement in efficiency using alloyed contacts based on Au-Ge eutectic, and Ref. 15 reported a 25% increase in sensitivity using recessed surface contacts.

This article presents a finite element model to analyze the photoresponse of two types of LT-GaAs MSM's, both of the same device geometry, but one with non-alloyed surface contacts and the other with alloyed contacts. Based on experimental work,¹⁴ the simulated photodetectors consist of interdigitated conductors, patterned on a 1.5- μm -thick LT-GaAs layer, grown by molecular beam epitaxy at 250°C, followed by *in-situ* isothermal annealing at 600°C. We can, therefore, directly correlate our simulations with the experimental results and understand the physical reasons for the improved photoresponse efficiency of the alloyed-contact LT-GaAs MSM's without sacrificing the response times. We demonstrate that indeed the latter devices have better-than-twice the sensitivity of the surface-contact structures and better-than-50% improvement in response time. We further use our model to propose the configuration of optimized devices.

Finite Element Model

The finite element simulations presented here were created with the COMSOL Multiphysics® Finite Element Analysis (FEA) software package¹⁶ using the generalized electrostatics mode. In this mode, the equation of continuity is combined with Gauss's law, and the partial differential equation to be solved is

$$-\nabla \cdot \left[(\sigma + \epsilon_0 \epsilon_r / T) \nabla V - \mathbf{J}^e \right] = \rho_0 / T, \quad (1)$$

where σ and ϵ_r , ϵ_0 are the material's conductivity and permittivity, respectively, V is the electric potential, \mathbf{J}^e is an externally sourced current density, ρ_0 is the given space-charge density at $t = 0$, and T is a time constant chosen to be large relative to the maximum charge relaxation time of the system. For the simulations presented here, \mathbf{J}^e and ρ_0 are set to zero and T was chosen to be 10^{-2} s. Increasing T above 10^{-2} s had no effect on the results; making it too large, however, could result in an ill-conditioned FEA formulation.

The model geometry is a two-dimensional cross section of one of the photoconductive LT-GaAs channels plus the electrodes. The results of the simulation are given per meter, and the result is multiplied by the overall length of the channel, which

is $147\ \mu\text{m}$. Figure 119.36 shows a schematic of the MSM top view and cross section used for simulation. The model boundary condition is electrical insulation everywhere, except for the small spans, where the electrode intersects the boundary and the condition is a fixed electrical potential. The actual fabricated device¹⁴ had an area of $400\ \mu\text{m}^2$ and an electrode finger width and spacing of $1\ \mu\text{m}$ and $1.5\ \mu\text{m}$, respectively. The alloyed-electrode MSM consisted of a Ni-Au/Ge-Ni-Au layer stack with 5-, 90-, 25-, and 50-nm thickness, respectively, alloyed at 420°C for 90 s. The surface-contact device had a Ni-Au layer with a thickness of 10 to 160 nm.

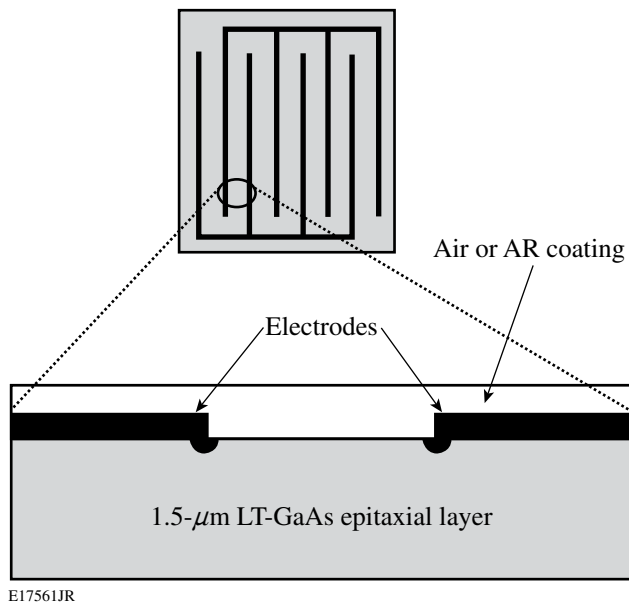


Figure 119.36
Schematic top view of an MSM device and side view of one photoconductive channel, with electrodes on each side.

Figures 119.37 and 119.38 show arrow plots of the electric field and current density, created with COMSOL Multiphysics®. The simulation results in Fig. 119.37 are for the alloyed-electrode device, illuminated by 850-nm-wavelength light, with a nominal alloy depth of $L = 200\ \text{nm}$. The simulation results in Fig. 119.38 are for the surface-contact device, with identical illumination conditions. The length of the arrows is scaled according to the magnitude of the quantity they represent. We note in Fig. 119.37 that for the alloyed device, the electric field is uniformly distributed in the photoconductive region, and the current density in this region decays as does the intensity of the incident light. On the other hand, the surface contact device in Fig. 119.38 shows a very different electric field distribution, and the current is channeled entirely through the corner insets of the electrodes.

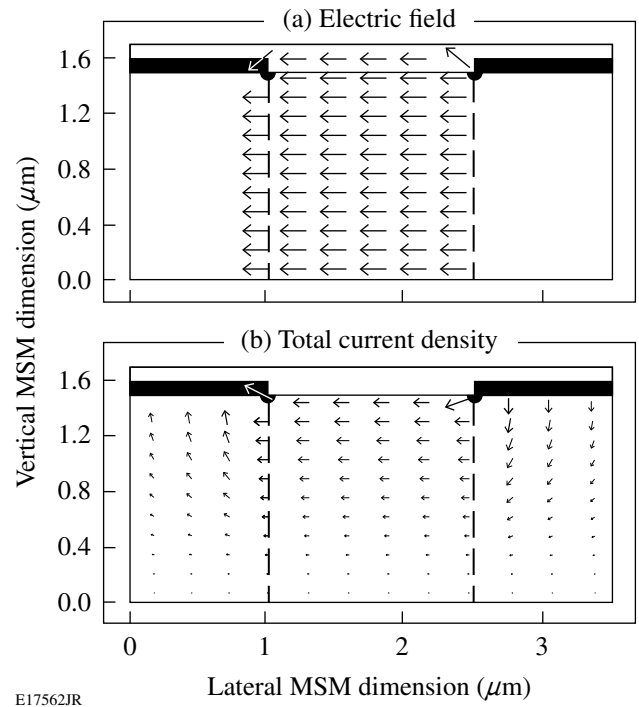


Figure 119.37
Arrow plots of the (a) electric field and (b) current density for the alloyed-contact device with $L = 200\ \text{nm}$. These plots were created using COMSOL Multiphysics®.¹⁶

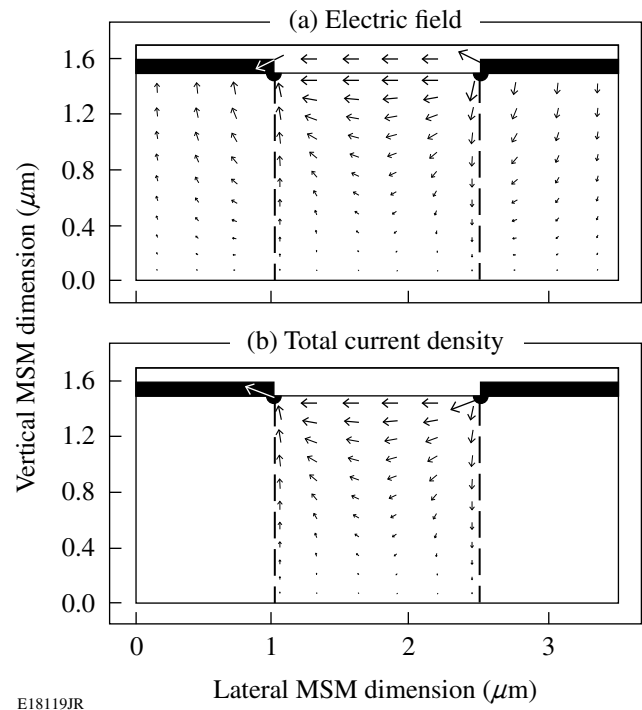


Figure 119.38
Arrow plots of the (a) electric field and (b) current density for the surface-contact device. These plots were created using COMSOL Multiphysics®.¹⁶

For the FEA model, each device was divided into five sub-domains, consisting of the two electrodes, the photoconductive region, and the two LT-GaAs regions under the electrodes. For simplicity, the two electrodes were assigned a conductivity $\sigma = 45.6 \times 10^6$ S/m, typical for Au. The conductivity profile of the photoconductive region was calculated based on illumination with 160 μ W of continuous-wave light, consistent with the experimental setup in Ref. 14. The transmission coefficient was calculated as 43%, based on the LT-GaAs refractive index of 3.64 at 850 nm (Ref. 17), and the internal quantum efficiency (QE) was taken as 1. These factors, in addition to 40% loss of input power as a result of the reflectivity of the metal electrodes, give $G = 1.77 \times 10^{14}$ s⁻¹, the overall (volume) carrier-generation rate. By assuming that the carrier generation decays in the same manner as incident 850-nm light with a penetration depth $l = 1$ μ m, and integrating over the photoconductive volume, the carrier generation at the surface was calculated to be $G_S = 9.47 \times 10^{23}$ (s \cdot cm³)⁻¹.

To relate G_S to σ , it is necessary to compute the resulting steady-state carrier density. This was done by setting the generation equal to the Shockley–Read–Hall recombination rate, simplified by assuming that the recombination centers are located at the bandgap. The electron and hole concentrations at the surface, n_s and p_s , respectively, can then be calculated as

$$n_s = p_s = n_i + 2 \cdot G_S \cdot \tau, \quad (2)$$

where n_i is the intrinsic GaAs carrier concentration and τ is the carrier lifetime. Taking for LT-GaAs at 300 K, $n_i = 1.8 \times 10^6$ cm⁻³, $\tau = 150$ fs (Ref. 5), and the mobility for photogenerated carriers to be $\mu \approx 200$ cm²/(V \cdot s) (Ref. 1), we may then compute the surface conductivity $\sigma_s = 2n_s\mu = 1.8$ mS/m, and, subsequently, the conductivity profile

$$\sigma = \sigma_s \cdot \exp\left(\frac{-z}{l}\right), \quad (3)$$

where z is the distance from the LT-GaAs surface.

So far everything said about our MSM FEA model applies to both the alloyed and non-alloyed devices. The difference between the two is the conductivity profile under the contacts. In the case of the non-alloyed device, the conductivity of the region under the contact is simply that of LT-GaAs, which is essentially an insulator. In the case of the alloyed device, a Ni-AuGe-Ni-Au layer stack forms the electrode. Subsequent alloying at 420°C for 90 s causes Ge atoms to migrate into the

LT-GaAs, with an expected penetration depth of $L = 200$ nm (Ref. 18). As a result, the conductivity at the interface between the contact metallization and the alloyed LT-GaAs is that of Ge and decays exponentially to the conductivity of LT-GaAs under the contact. The σ profile under the alloyed contact is therefore

$$\sigma_{ac} = (\sigma_{Ge} - \sigma_{LT}) \cdot \exp\left(\frac{-z}{L}\right) + \sigma_{LT}, \quad (4)$$

where $\sigma_{Ge} = 2.2$ S/m and $\sigma_{LT} = 1.15 \times 10^{-8}$ S/m are the conductivities of Ge and LT-GaAs, respectively.

One additional feature that requires some explanation is the semicircular inset at the inside corner of each electrode shown in Fig. 119.36. In the case of the alloyed-contact MSM, this feature has no effect on results; it is, however, essential for modeling the surface-electrode device since without it there would be no lateral path for current. Figure 119.36 is not to scale and the corner insets are exaggerated for clarity. The actual radius used in our modeling was only 50 nm, based on the simple estimation that the carriers generated near the edge of the surface electrode may drift/diffuse into the insulating region toward the electrode on the scale of the carrier mean free path, equal in our case to ~ 66 nm, for a Fermi velocity of 4.4×10^5 m/s (Ref. 12) and $\tau = 150$ fs. A change of $\pm 50\%$ in this radius did not impact results of the model.

Results

1. Responsivity

For the alloyed-contact device, the responsivity predicted by the model was 8.6×10^{-4} A/W, while the actual measured value in Ref. 14 was 13.7×10^{-4} A/W. For the surface-electrode MSM, the corresponding simulation and experimental values were 3.7×10^{-4} A/W and 6.2×10^{-4} A/W, respectively. Considering the approximations involved, the results of the FEA model can be considered reasonably close to measured. The responsivity is dependent on μ , quantum efficiency, transmission coefficient of LT-GaAs, alloy depth, and the contact resistance. If we, for example, used a carrier mobility of only $\mu \approx 320$ cm²/(V \cdot s), instead of 200 cm²/(V \cdot s), we would get full agreement between our model and the experiment. We note here that although the relatively low values of μ for LT-GaAs have been well documented,⁸ some sources have reported μ 's as high as 2000 cm²/(V \cdot s) (Refs. 19 and 20), depending on the sample processing. For QE the range of numbers in the literature spans from 1 (Ref. 21) to 0.07 (Ref. 5). We assumed the ideal case of QE = 1. Our transmission coefficient was calculated to be 43%, based on the refractive index of GaAs at

850 nm, and, finally, the depth of alloying under the contacts was taken to be 200 nm based on the expected (but not measured) depth stated in Ref. 14.

In view of the above, the responsivity ratio of MSM's with alloyed to non-alloyed contacts is of particular interest. The FEA model yielded a ratio of 2.3, while the experimental value in Ref. 14 was 2.2. Therefore, we may conclude that our model does a good job of predicting the improvement in responsivity obtained using photodetectors with alloyed contacts.

2. Capacitance and Transient Response

Typically, photoconductive devices turn on much faster than they turn off since the rising part of the photoresponse limits how fast optical energy is delivered to the photocarriers and simply corresponds to the integral of the optical-pulse intensity. The turn-off time, on the other hand, depends on the mechanism of carrier sweep (Schottky type) or on the carrier lifetime in the photoconductive region. In the case of LT-GaAs devices exhibiting ohmic contacts, the latter is true; however, since τ is in the femtosecond range, the actual device turn-off time is limited by stored charge and the equivalent lumped-element resistive-capacitive (RC) time constant.

Table 119.IV shows the capacitance of the alloyed- and surface-electrode devices in both the light-ON and light-OFF states, as predicted by the FEA model. The higher capacitance of the alloyed-contact MSM is expected from the device configuration and suggests that its photoresponse signal should be slower. However, the photoresponse measurements performed in Ref. 14 actually indicate that alloyed devices exhibit somewhat faster turn-offs, while in both cases, the turn-on time is about the same. The photoresponse transients in Ref. 14 show a turn-off time constant of the alloyed device to be 1.8 ps and 2.8 ps for the non-alloyed structure. In terms of our model, an improvement of the turn-off time in the alloyed-electrode MSM's can be understood if one considers the accumulated charge at the boundary between the LT-GaAs photoconductive region and either the alloyed or non-alloyed region under the

Table 119.IV: MSM device capacitance in the OFF and ON states, with or without an AR coating.

	Surface contact	Alloyed contact
OFF, no AR	10.2 (fF)	17.0 (fF)
OFF, with AR	10.7 (fF)	17.5 (fF)
ON, no AR	10.4 (fF)	15.6 (fF)
ON, with AR	10.5 (fF)	16.0 (fF)

electrode surface. In the ON state, both devices have a significant charge, accumulated at this boundary. In the case of the surface-contact MSM, however, this boundary effectively goes away when the device turns off, leaving the charge to dissipate through the volume of the very highly resistive LT-GaAs. On the other hand, in the alloyed-contact MSM case, the relatively high conductance of the alloyed-contact volume makes possible a much more efficient discharge of the equivalent capacitor. Based on the ratio of sensitivities of the two devices, the effective ON-state resistance of the alloyed device is $2.2\times$ lower than that of the non-alloyed device. Thus, including the capacitances listed in Table 119.IV, the ratio of the corresponding RC time constants is 1.47 and should be the same as the ratio of the fall times of the respective photoresponse transients. Note that the experimentally measured ratio in Ref. 14 is 1.56, in excellent agreement with the prediction of our model. As a result, despite the larger geometrical capacitance, the alloyed-contact MSM is actually faster than the surface-electrode structure, as indeed was experimentally observed.

3. Device Optimization

The results of the FEA model are well correlated to experimental values; therefore, the model may be used to predict the effect of various parameters on MSM photoresponse performance. In this section, we look at how such technological parameters as the depth of the alloyed contacts, electrode spacing, or additional antireflection (AR) coating, influence the device's performance.

Figure 119.39 shows the responsivity as a function of alloy penetration depth L , which is the exponential spatial decay constant of σ under the alloyed contact [see Eq. (4)]. As the L

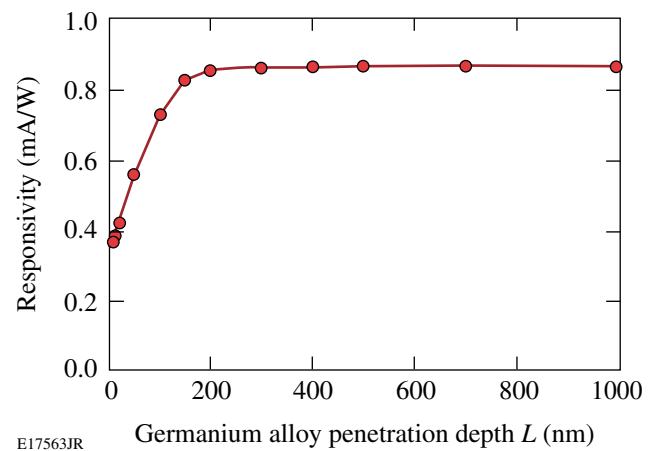


Figure 119.39 Responsivity versus the alloy penetration depth for an alloyed-contact MSM.

value decreases to zero, approximating the surface-type contact, the point where the responsivity curve intersects the y axis approaches the responsivity of the surface-electrode MSM. We observe in Fig. 119.39 that for $L > 200$ nm the curve flattens, so increasing L beyond 200 nm results in very little improvement. The latter is fully understandable looking at Fig. 119.37(a) and noting that at $L = 200$ nm the electric field is already fairly uniform down through the photoconductive region. The electric potential between the boundaries of the photoconductive region is also uniform and equal to the applied electrode potential, so current is strictly limited by the photoconductance.

Figure 119.40 shows the responsivity as a function of electrode spacing, for both an alloyed- and a surface-contact MSM. For the alloyed device, the relationship can be easily and precisely explained because the resistance of the photoconductive channel is proportional to its length. Therefore, the responsivity is proportional to current and, consequently, inversely proportional to the channel length. For the surface-electrode MSM, the relationship is not as simple due to the concentration of current at the corner insets of the electrodes, as seen in Fig. 119.38. The corner insert will come into play only when the spacing approximately equals the radius. As the spacing decreases for the surface-electrode device, the electric field gets pulled toward the surface. Therefore, carriers generated far below the surface do not contribute to the sensitivity.

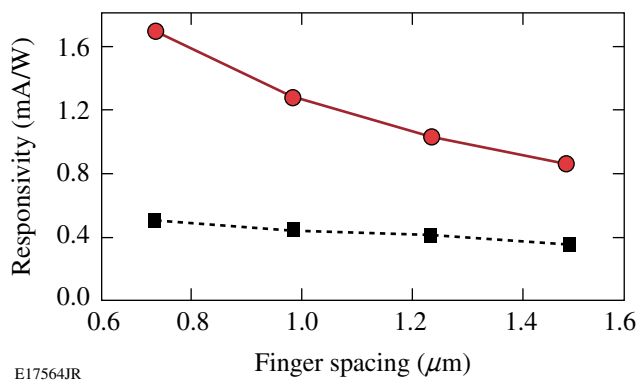


Figure 119.40
Responsivity versus the electrode finger spacing for an alloyed-contact (solid line) and surface-contact (dashed) MSM.

Finally, our FEA model predicts that an AR coating should obviously improve the device responsivity by decreasing the amount of reflected light, but, at the same time, the additional dielectric material deposited on top of the photodetector increases its capacitance. We observe a typical trade-off

between the responsivity and speed. However, in the case of the alloyed-contact structures our simulations show (see Table 119.IV) that the actual increase in the capacitance is less than 5%. As a result, a well-designed AR coating in such structures clearly leads to an overall improvement in the photodetector's performance by increasing the responsivity without significant degradation in speed.

Conclusion

A simple FEA model, using the COMSOL Multiphysics® software package,¹⁶ has been developed to simulate the photo-response of the MSM photodetector. The two experimentally most-viable cases, namely devices with either alloyed- or non-alloyed-surface contacts, have been studied and have demonstrated that in both cases, both the photodetector responsivity and the time-domain response can be very accurately simulated. This approach also allows one to optimize the MSM design, indicating that deposition on the photodetector surface of an AR coating, while substantially increasing its responsivity, only marginally affects the photoresponse time constant.

ACKNOWLEDGMENT

This work is supported by the NSF NIRT Grant No. ECS-0609140. Additional support was provided by the U.S. Department of Energy Office of Inertial Confinement Fusion under Cooperative Agreement No. DE-FC52-08NA28302, the University of Rochester, and the New York State Energy Research and Development Authority. The support of DOE does not constitute an endorsement by DOE of the views expressed in this article.

REFERENCES

1. F. W. Smith, in *Low Temperature (LT) GaAs and Related Materials*, edited by G. L. Witt *et al.*, Mat. Res. Soc. Symp. Proc. Vol. 241 (Materials Research Society, Pittsburgh, PA, 1992), pp. 3–12.
2. S. Gupta, J. F. Whitaker, and G. A. Mourou, *IEEE J. Quantum Electron.* **28**, 2464 (1992).
3. S. Y. Chou, Y. Liu, and W. Khalil, *Appl. Phys. Lett.* **61**, 819 (1992).
4. M. Marso, M. Mikulics, R. Adam, S. Wu, X. Zheng, I. Camara, F. Siebe, A. Forster, R. Gusten, P. Kordoš, and R. Sobolewski, *Acta Phys. Pol. A* **107**, 109 (2005).
5. X. Zheng, Y. Xu, R. Sobolewski, R. Adam, M. Mikulics, M. Siegel, and P. Kordoš, *Appl. Opt.* **42**, 1726 (2003).
6. S. Kono *et al.*, *Appl. Phys. Lett.* **77**, 4104 (2000).
7. X.-C. Zhang, *J. Lumin.* **66 & 67**, 488 (1996).
8. S. Verghese, K. A. McIntosh, and E. R. Brown, *Appl. Phys. Lett.* **71**, 2743 (1997).
9. M. Mikulics *et al.*, *Appl. Phys. Lett.* **88**, 041118 (2006).

10. H. Yamamoto, Z-Q. Fang, and D. C. Look, *Appl. Phys. Lett.* **57**, 1537 (1990).
11. N. Braslau, J. B. Gunn, and J. L. Staples, *Solid State Commun.* **10**, 381 (1967).
12. N. Vieweg *et al.*, *Opt. Express* **16**, 19,695 (2008).
13. S. Collin, F. Pardo, and J-L. Pelouard, *Appl. Phys. Lett.* **83**, 1521 (2003).
14. M. Mikulics, M. Marso, S. Wu, A. Fox, M. Lepsa, D. Grützmacher, R. Sobolewski, and P. Kordoš, *IEEE Photon. Technol. Lett.* **20**, 1054 (2008).
15. M. Mikulics, S. Wu, M. Marso, R. Adam, A. Förster, A. van der Hart, P. Kordoš, H. Lüth, and R. Sobolewski, *IEEE Photonics Technol. Lett.* **18**, 820 (2006).
16. COMSOL® and COMSOL Multiphysics® are registered trademarks of COMSOL AB, Tegnérgatan 23, SE-111 40 Stockholm, Sweden.
17. J. S. Blakemore, *J. Appl. Phys.* **53**, R123 (1982).
18. M. Ogawa, *J. Appl. Phys.* **51**, 406 (1980).
19. K. Xie and C. R. Wie, in *Low Temperature (LT) GaAs and Related Materials Symposium*, edited by G. L. Witt *et al.*, *Mat. Res. Soc. Symp. Proc.* Vol. 241 (Materials Research Society, Pittsburgh, PA, 1992), pp. 33–38.
20. A. C. Warren *et al.*, in *Low Temperature (LT) GaAs and Related Materials Symposium*, edited by G. L. Witt *et al.*, *Mat. Res. Soc. Symp. Proc.* Vol. 241 (Materials Research Society, Pittsburgh, PA, 1992), pp. 15–25.
21. Electrical Properties of Gallium Arsenide, IOFFE-Physico Technical Institute, St. Petersburg 194021, Russia, <http://www.ioffe.ru/SVA/NSM/Semicond/GaAs/electrical.html>.

Publications and Conference Presentations

Publications

- T. R. Boehly, D. Munro, P. M. Celliers, R. E. Olson, D. G. Hicks, V. N. Goncharov, G. W. Collins, H. F. Robey, S. X. Hu, J. A. Marozas, T. C. Sangster, O. L. Landen, and D. D. Meyerhofer, "Demonstration of the Shock-Timing Technique for Ignition Targets on the National Ignition Facility," *Phys. Plasmas* **16**, 056302 (2009) (invited).
- X. L. Cross, X. Zheng, P. D. Cunningham, L. M. Hayden, Š. Chromik, M. Sojkova, V. Štrbík, P. Odier, and R. Sobolewski, "Pulsed-THz Characterization of Hg-Based, High-Temperature Superconductors," *IEEE Trans. Appl. Supercond.* **19**, 3614 (2009).
- V. N. Goncharov, "Ablative Richtmyer-Meshkov Instability: Theory and Experimental Results," in *Laser-Plasma Interactions*, Scottish Graduate Series, edited by D. A. Jaroszynski, R. Bingham, and R. A. Cairns (CRC Press, Boca Raton, FL, 2009), pp. 419–427.
- V. N. Goncharov, "Direct-Drive Inertial Fusion: Basic Concepts and Ignition Target Designing," in *Laser-Plasma Interactions*, Scottish Graduate Series, edited by D. A. Jaroszynski, R. Bingham, and R. A. Cairns (CRC Press, Boca Raton, FL, 2009), pp. 409–418.
- O. V. Gotchev, J. P. Knauer, P. Y. Chang, N. W. Jang, M. J. Shoup III, D. D. Meyerhofer, and R. Betti, "Seeding Magnetic Fields for Laser-Driven Flux Compression in High-Energy-Density Plasmas," *Rev. Sci. Instrum.* **80**, 043504 (2009).
- Z. Jiang and J. R. Marciante, "Comments on 'Beam Quality Factor of Higher Order Modes in a Step-Index Fiber,'" *J. Lightwave Technol.* **27**, 1236 (2009).
- J. Kitaygorsky, S. Dorenbos, E. Reiger, R. Schouten, V. Zwiller, and R. Sobolewski, "HEMT-Based Readout Technique for Dark- and Photon-Count Studies in NbN Superconducting Single-Photon Detectors," *IEEE Trans. Appl. Supercond.* **19**, 346 (2009).
- C. K. Li, F. H. Séguin, J. A. Frenje, M. Manuel, D. Casey, N. Sinenian, R. D. Petrasso, P. A. Amendt, O. L. Landen, J. R. Rygg, R. P. J. Town, R. Betti, J. Delettrez, J. P. Knauer, F. Marshall, D. D. Meyerhofer, T. C. Sangster, D. Shvarts, V. A. Smalyuk, J. M. Soures, C. A. Back, J. D. Kilkenny, and A. Nikroo, "Proton Radiography of Dynamic Electric and Magnetic Fields in Laser-Produced High-Energy-Density Plasmas," *Phys. Plasmas* **16**, 056304 (2009).
- F. J. Marshall, P. W. McKenty, J. A. Delettrez, R. Epstein, J. P. Knauer, V. A. Smalyuk, J. A. Frenje, C. K. Li, R. D. Petrasso, F. H. Séguin, and R. C. Mancini, "Plasma-Density Determination from X-Ray Radiography of Laser-Driven Spherical Implosions," *Phys. Rev. Lett.* **102**, 185004 (2009).
- C. Miao, S. N. Shafir, J. C. Lambropoulos, J. Mici, and S. D. Jacobs, "Shear Stress in Magnetorheological Finishing for Glasses," *Appl. Opt.* **48**, 2585 (2009).
- E. I. Moses, R. L. McCrory, D. D. Meyerhofer, and C. J. Keane, "A New Era for High-Energy-Density Physics," *Opt. Photonics News* **20**, 42 (2009).
- J. Myatt, J. A. Delettrez, A. V. Maximov, D. D. Meyerhofer, R. W. Short, C. Stoeckl, and M. Storm, "Optimizing Electron-Positron Pair Production on Kilojoule-Class High-Intensity Lasers for the Purpose of Pair-Plasma Creation," *Phys. Rev. E* **79**, 066409 (2009).
- G. P. Pepe, D. Pan, V. Pagliarulo, L. Parlato, N. Marrocco, C. De Lisio, G. Peluso, A. Barone, U. Scotti di Uccio, A. Casaburi, F. Tafuri, M. Khafizov, T. Taneda, and R. Sobolewski, "Ultrafast Photoresponse of Superconductor/Ferromagnet Nano-Layered Hybrids," *IEEE Trans. Appl. Supercond.* **19**, 376 (2009).
- H. Sawada, S. P. Regan, P. B. Radha, R. Epstein, D. Li, V. N. Goncharov, S. X. Hu, D. D. Meyerhofer, J. A. Delettrez, P. A. Jaanimagi, V. A. Smalyuk, T. R. Boehly, T. C. Sangster,

B. Yaakobi, and R. C. Mancini, "Al $1s-2p$ Absorption Spectroscopy of Shock-Wave Heating and Compression in Laser-Driven Planar Foil," *Phys. Plasmas* **16**, 052702 (2009).

J. E. Schoenly, W. Seka, and P. Rechmann, "Laser Ablation of Dental Calculus at 400 nm Using a Ti:Sapphire Laser," in *Lasers in Dentistry XV*, edited by R. Rechmann and D. Fried (SPIE, Bellingham, WA, 2009), Vol. 7162, Paper 71620E.

W. Seka, D. H. Edgell, J. A. Myatt, A. V. Maximov, R. W. Short, V. N. Goncharov, and H. A. Baldis, "Two-Plasmon-Decay Instability in Direct-Drive Inertial Confinement Fusion Experiments," *Phys. Plasmas* **16**, 052701 (2009).

V. A. Smalyuk, R. Betti, T. R. Boehly, R. S. Craxton, J. A. Delettrez, D. H. Edgell, V. Yu. Glebov, V. N. Goncharov, D. R. Harding, S. X. Hu, J. P. Knauer, F. J. Marshall, R. L. McCrory, P. W. McKenty, D. D. Meyerhofer, P. B. Radha, S. P. Regan, T. C. Sangster, W. Seka, R. W. Short, D. Shvarts, S. Skupsky, J. M. Soures, C. Stoeckl, B. Yaakobi, J. A. Frenje, C. K. Li, R. D. Petrasso, and F. H. Séguin, "Cryogenic-Target Performance and Implosion Physics Studies on OMEGA," *Phys. Plasmas* **16**, 056301 (2009) (invited).

A. A. Solodov, K. S. Anderson, R. Betti, V. Gotcheva, J. Myatt, J. A. Delettrez, S. Skupsky, W. Theobald, and C. Stoeckl, "Integrated Simulations of Implosion, Electron Transport, and

Heating for Direct-Drive Fast-Ignition Targets," *Phys. Plasmas* **16**, 056309 (2009).

M. Storm, A. A. Solodov, J. F. Myatt, D. D. Meyerhofer, C. Stoeckl, C. Mileham, R. Betti, P. M. Nilson, T. C. Sangster, W. Theobald, and C. Guo, "High-Current, Relativistic Electron-Beam Transport in Metals and the Role of Magnetic Collimation," *Phys. Rev. Lett.* **102**, 235004 (2009).

L. Sun, S. Jiang, J. D. Zuegel, and J. R. Marciante, "Effective Verdet Constant in a Terbium-Doped-Core Phosphate Fiber," *Opt. Lett.* **34**, 1699 (2009).

I. A. Walmsley and C. Dorrer, "Characterization of Ultrashort Electromagnetic Pulses," *Adv. Opt. Photon.* **1**, 308 (2009).

L. Zeng, F. Yan, S. K.-H. Wei, S. W. Culligan, and S. H. Chen, "Synthesis and Processing of Monodisperse Oligo(fluorene-co-bithiophene)s into Oriented Films by Thermal and Solvent Annealing," *Adv. Funct. Mater.* **19**, 1978 (2009).

J. D. Zuegel, S.-W. Bahk, J. Bromage, C. Dorrer, R. Earley, T. J. Kessler, B. J. Kruschwitz, S. F. B. Morse, D. N. Maywar, J. B. Oliver, J. Qiao, A. L. Rigatti, A. W. Schmid, M. J. Shoup III, L. J. Waxer, and J. H. Kelly, "Novel Laser and Diagnostic Technologies for the OMEGA EP High-Energy Petawatt Laser," *Rev. Laser Eng.* **37**, 437 (2009).

Forthcoming Publications

A. Belousov, S. Katrych, J. Jun, J. Karpinski, B. Batlogg, D. Günther, J. Zhang, and R. Sobolewski, "Bulk Single-Crystal Growth of the Ternary $\text{Al}_x\text{Ga}_{1-x}\text{N}$ from Solution in Gallium Under High Pressure," to be published in *Applied Physics Letters*.

J. Bromage, C. Dorrer, J. R. Marciante, M. J. Shoup III, and J. D. Zuegel, "Modal Measurement of a Large-Mode-Area Photonic-Crystal Fiber Amplifier Using Spatially Resolved Spectral Interferometry," to be published in *Solid-State Diode Laser Technology Review*.

B. Ciftcioglu, L. Zhang, J. Zhang, J. R. Marciante, J. Zuegel, R. Sobolewski, and H. Wu, "Integrated Silicon PIN Photodiodes Using Deep N-Well in a Standard 0.18- μm CMOS Technology," to be published in the *Journal of Lightwave Technology*.

W. R. Donaldson, J. R. Marciante, and R. G. Roides, "An Optical Replicator for Single-Shot Measurements at 10 GHz with a Dynamic Range of 1800:1," to be published in the *IEEE Journal of Quantum Electronics*.

C. Dorrer, "High-Damage-Threshold Beam Shaping Using Binary Phase Plates," to be published in *Optics Letters*.

E. Glowacki, C. W. Ching, and K. L. Marshall, "Photoswitchable Gas Permeation Membranes Based on Azobenzene-Doped Liquid Crystals," to be published in *Optics and Photonics* (invited).

G. Guarino, W. R. Donaldson, M. Mikulics, M. Marso, P. Kordoš, and R. Sobolewski, "Finite Element Simulation of Metal-Semiconductor-Metal Photodetector," to be published in *Solid-State Electronics*.

S. X. Hu, L. A. Collins, and B. I. Schneider, "Attosecond Photoelectron Microscopy of H_2^+ ," to be published in *Physical Review A*.

I. V. Igumenshchev, F. J. Marshall, J. A. Marozas, V. A. Smalyuk, R. Epstein, V. N. Goncharov, T. J. B. Collins, T. C. Sangster, and S. Skupsky, "The Effects of Target Mounts in Direct-Drive Implosions on OMEGA," to be published in *Physics of Plasmas*.

J. Kitaygorsky, R. Shouten, S. Dorenbos, E. Reiger, V. Zwiller, and R. Sobolewski, "Resolving Dark Pulses from Photon Pulses in NbN Superconducting Single-Photon Detectors," to be published in the *Journal of Modern Optics*.

C. Miao, J. C. Lambropoulos, S. N. Shafrir, H. Romanofsky, and S. D. Jacobs, "Contributions of Nanodiamond Abrasives and Deionized Water in Magnetorheological Finishing of Aluminum Oxynitride," to be published in *Optical Manufacturing and Testing VIII*.

C. Miao, S. N. Shafrir, J. C. Lambropoulos, and S. D. Jacobs, "Normal Force and Drag Force in Magnetorheological Finishing," to be published in *Optical Manufacturing and Testing VIII*.

A. V. Okishev, D. Westerfeld, L. Shterengas, and G. Belenky, "A Stable Mid-IR, GaSb-Based Diode Laser Source for Cryogenic Target Handling at the Omega Laser Facility," to be published in *Optics Express*.

G. P. Pepe, L. Parlato, N. Marrocco, V. Pagliarulo, G. Peluso, A. Barone, F. Tafuri, U. Scotti di Uccio, F. Miletto, M. Radovic, D. Pan, and R. Sobolewski, "Novel Superconducting Proximized Heterostructures for Ultrafast Photodetection," to be published in *Cryogenics*.

S. P. Regan, "Applied Plasma Spectroscopy I: Laser-Fusion Experiments," to be published in *High Energy Density Physics*.

J. Sanz, R. Betti, V. A. Smalyuk, M. Olazabal-Loume, V. Drean, V. Tikhonchuk, X. Ribeyre, and J. Feugeas, "Radiation Hydrodynamic Theory of Double Ablation Fronts in Direct-Drive Inertial Confinement Fusion," to be published in *Physics of Plasmas*.

S. N. Shafrir, H. J. Romanofsky, M. Skarlinski, M. Wang, C. Miao, S. Salzman, T. Chartier, J. Mici, J. C. Lambropoulos, R. Shen, H. Yang, and S. D. Jacobs, "Zirconia Coated Carbonyl Iron Particle-Based Magnetorheological Fluid for Polishing Optical Glasses and Ceramics," to be published in *Optical Manufacturing and Testing VIII*.

W. Theobald, K. S. Anderson, R. Betti, R. S. Craxton, J. A. Delettrez, J. A. Frenje, V. Yu. Glebov, O. V. Gotchev, J. H. Kelly, C. K. Li, A. J. Mackinnon, F. J. Marshall, R. L. McCrory, D. D. Meyerhofer, J. F. Myatt, P. A. Norreys, P. M. Nilson, P. K. Patel, R. D. Petrasso, P. B. Radha, C. Ren, T. C. Sangster, W. Seka, V. A. Smalyuk, A. A. Solodov, R. B. Stephens, C. Stoeckl, and B. Yaakobi, "Advanced-Ignition-Concept Exploration on OMEGA," to be published in *Plasma Physics and Controlled Fusion*.

W. Theobald, C. Stoeckl, P. A. Jaanimagi, P. M. Nilson, M. Storm, D. D. Meyerhofer, T. C. Sangster, D. Hey, A. J. MacKinnon, H.-S. Park, P. K. Patel, R. Shepherd, R. A. Snively, M. H. Key, J. A. King, B. Zhang, R. B. Stephens, K. U. Akli, K. Highbarger, R. L. Daskalova, L. Van Woerkom, R. R. Freeman, J. S. Green, G. Gregori, K. Lancaster, and P. A. Norreys, "A Dual-Channel, Curved-Crystal Spectrograph for Petawatt-Laser, X-Ray Backlighter Source Studies," to be published in *Review of Scientific Instruments*.

Conference Presentations

The following presentations were made at OMEGA Laser Facility Users' Group Workshop, Rochester, NY, 29 April–1 May 2009:

M. A. Barrios, D. E. Fratanduono, T. R. Boehly, D. D. Meyerhofer, D. G. Hicks, P. M. Celliers, and J. H. Eggert, "Precision Equation of State (EOS) Measurements Using Laser-Driven Shock Waves on the OMEGA Laser."

D. E. Fratanduono, M. A. Barrios, T. R. Boehly, D. D. Meyerhofer, J. Eggert, R. Smith, D. G. Hicks, and G. Collins, "Measurements of Strain-Induced Refractive Index Changes in Shocked LiF Using Laser-Driven Flyer Plates."

O. V. Gotchev, R. Betti, P. Y. Chang, J. P. Knauer, O. Polomarov, D. D. Meyerhofer, J. A. Frenje, C. K. Li, M. Manuel, R. D. Petrasso, and F. H. Séguin, "Embedding Strong External Magnetic Fields in OMEGA Implosions—An Experimental Reality with Applications to Fusion, Exotic Plasma States, and More. The Designer and Use Perspectives."

J. Hager, V. A. Smalyuk, I. V. Igumenshchev, D. D. Meyerhofer, and T. C. Sangster, "First Rayleigh–Taylor and Richtmyer–Meshkov Instability Measurements in Laser-Driven Planar Targets on the OMEGA EP Laser."

D. R. Harding and M. J. Bonino, "Target Fabrication: Capabilities and the Ordering Process."

S. F. B. Morse, "Omega Facility: Status and Performance."

P. M. Nilson, W. Theobald, J. F. Myatt, C. Stoeckl, P. A. Jaanimagi, J. A. Delettrez, B. Yaakobi, J. D. Zuegel, R. Betti, D. D. Meyerhofer, T. C. Sangster, P. K. Patel, A. J. Mackinnon, and K. Akli, "Characterization and Optimization of Fast-Electron Sources Using Intense, Multi-kJ Pulses on OMEGA EP."

G. Pien, "Engineering Support and Qualification Process for Interfacing New Experiments."

C. Ren, G. Li, R. Yan, J. Tonge, and W. B. Mori, "Simulations of Laser Channeling in Millimeter-Scale Underdense Plasmas for Fast Ignition."

T. C. Sangster, "Diagnostic Status on OMEGA EP"

C. Stoeckl, "Status of OMEGA EP, an Experimentalist's Perspective."

W. Theobald, K. S. Anderson, R. Betti, R. S. Craxton, J. A. Delettrez, J. A. Frenje, V. Yu. Glebov, O. V. Gotchev, A. J. Mackinnon, F. J. Marshall, R. L. McCrory, D. D. Meyerhofer, J. F. Myatt, P. A. Norreys, P. M. Nilson, P. K. Patel, R. D. Petrasso, P. B. Radha, C. Ren, T. C. Sangster, A. A. Solodov, R. B. Stephens, C. Stoeckl, M. Storm, and C. D. Zhou, "Status of Integrated Fast- and Shock-Ignition Experiments on OMEGA."

K. A. Thorp, "OMEGA Properties and Capabilities."

The following presentations were made at the Second International Conference on High Energy Density Physics, Austin, TX, 19–22 May 2009:

V. N. Goncharov, T. C. Sangster, T. R. Boehly, R. L. McCrory, D. D. Meyerhofer, P. B. Radha, V. A. Smalyuk, S. Skupsky, J. A. Frenje, and R. D. Petrasso, "Multiple-Picket, Low-Adiabatic Cryogenic Fuel Compression on OMEGA."

W. Theobald, K. S. Anderson, R. Betti, R. S. Craxton, J. A. Delettrez, B. Eichman, V. Yu. Glebov, O. V. Gotchev, S. Ivancic, F. J. Marshall, R. L. McCrory, D. D. Meyerhofer, J. F. Myatt, P. M. Nilson, P. B. Radha, C. Ren, T. C. Sangster, A. A. Solodov, C. Stoeckl, M. Storm, C. D. Zhou, J. D. Zuegel, J. A. Frenje, R. D. Petrasso, P. A. Norreys, V. M. Ovchinnikov, F. F. Freeman, L. Van Woerkom, D. Hey, M. H. Key, A. J. MacKinnon, P. K. Patel, K. Akli, R. B. Stephens, and R. Lauck, "Integrated Fast- and Shock-Ignition Experiments on OMEGA. "

The following presentations were made at CLEO/IQEC 2009, Baltimore, MD, 31 May–5 June 2009:

S.-W. Bahk and J. D. Zuegel, "A High-Resolution Amplitude and Wavefront Control System Based on a Direct Zonal Closed-Loop Approach."

I. A. Begishev, A. V. Okishev, R. G. Roides, and J. D. Zuegel, "All-Fiber Discrete Arbitrary Picket-Pulse Shaping."

J. Bromage, C. Dorrer, M. J. Shoup III, and J. D. Zuegel, "Optimizing Injection into Large-Mode-Area Photonic Crystal-Fiber Amplifiers by Spatially Resolved Spectral Interferometry."

C. Dorrer, "Near-Field Intensity Shaping with Binary Phase Plates."

C. Dorrer, "Statistical Analysis of Incoherent Pulse Shaping."

C. Dorrer and J. Bromage, "Simple High-Sensitivity, Electro-Optic Sagnac Spectral Shearing Interferometry for Short Optical Pulse Characterization."

J. R. Marciante and R. G. Roides, "Mode Control in Large-Mode-Area Fiber Lasers Via Gain Filtering."

W. Yang and C. Dorrer, "Ultrafast Pulse Characterization of Semiconductor Single-Section Fabry-Perot Mode-Locked Lasers."

The following presentations were made at ICOPS/SOFE 2009, San Diego, CA, 31 May–5 June 2009:

D. R. Harding, D. H. Edgell, L. M. Elasky, R. Q. Gram, T. B. Jones, S. J. Verbridge, A. J. Weaver, and M. D. Wittman, "Cryogenic Targets for Inertial Confinement Fusion Experiments and Future Fusion-Energy Applications."

W. T. Shmayda, G. Wainwright, and R. Janezic, "Cryogenic Tritium Operations at OMEGA."

The following presentations were made at the 39th Anomalous Absorption Conference, Bodega Bay, CA, 14–19 June 2009:

D. DuBois, D. Russell, H. Vu, and J. Myatt, " $1/2 \omega_0$ Emission from the Nonlinear Currents Generated by the Two Plasmon Decay Instability."

D. H. Edgell, W. Seka, V. N. Goncharov, I. V. Igumenshchev, R. S. Craxton, J. A. Delettrez, J. F. Myatt, A. V. Maximov, R. W. Short, R. E. Bahr, "Time-Dependent Scattered-Light Spectroscopy in Direct-Drive-Implosion Experiments."

A. V. Maximov, J. F. Myatt, R. W. Short, W. Seka, J. A. Delettrez, and C. Stoeckl, "Modeling of Two-Plasmon-Decay Instability Under Crossed-Beam Irradiation."

J. F. Myatt, A. V. Maximov, R. W. Short, J. A. Delettrez, W. Seka, D. H. Edgell, D. F. DuBois, H. X. Vu, and D. A. Russell, "Extended Zakharov Modeling of the Two-Plasmon-Decay Instability in Inhomogeneous Direct-Drive ICF-Relevant Plasma."

D. Russell, D. DuBois, H. Vu, and J. Myatt, " $3/2 \omega_0$ Emission from the LDI Langmuir Waves Excited in the Nonlinear Saturation of the Two Plasmon Decay Instability."

W. Seka, D. H. Edgell, J. F. Myatt, A. V. Maximov, R. W. Short, V. N. Goncharov, D. F. DuBois, H. X. Vu, D. A. Russell, and H. A. Baldis, "Two-Plasmon-Decay Instability Relevant to Direct-Drive Experiments."

R. W. Short, "Anisotropy of Two-Plasmon Decay for Multiple Obliquely Incident Laser Beams."

H. Vu, D. DuBois, D. Russell, and J. Myatt, "Hot Electrons Production from the Two-Plasmon Decay Instability."

The following presentations were made at the 16th APS Topical Conference in Shock Compression of Condensed Matter, Nashville, TN, 28 June–3 July 2009:

M. A. Barrios, D. E. Fratanduono, T. R. Boehly, D. D. Meyerhofer, D. G. Hicks, P. M. Celliers, and J. H. Eggert, "High-Precision Measurements of the Equation of State (EOS) of Polymers at 100 to 1000 GPa Using Laser-Driven Shock Waves."

D. E. Fratanduono, M. A. Barrios, T. R. Boehly, D. D. Meyerhofer, R. Smith, J. H. Eggert, D. G. Hicks, P. M. Celliers, and G. W. Collins, "Measurements of Strain-Induced Refractive-Index Changes in Shocked LiF Using Laser-Driven Flyer Plates."

J. Bromage, C. Dorrer, J. R. Marciante, M. J. Shoup III, and J. D. Zuegel, "Modal Measurement of a Large-Mode-Area Photonic-Crystal Fiber Amplifier Using Spatially Resolved Spectral Interferometry," 22nd Annual Solid State and Diode Laser Technology Review, Newton, MA, 29 June–1 July 2009.

W. Theobald, K. S. Anderson, R. Betti, R. S. Craxton, J. A. Delettrez, J. A. Frenje, V. Yu. Glebov, O. V. Gotchev, J. H. Kelly, C. K. Li, A. J. Mackinnon, F. J. Marshall, R. L. McCrory, D. D. Meyerhofer, J. F. Myatt, P. A. Norreys, P. M. Nilson, P. K. Patel, R. D. Petrasso, P. B. Radha, C. Ren, T. C. Sangster, W. Seka, V. A. Smalyuk, A. A. Solodov, R. B. Stephens, C. Stoeckl, and B. Yaakobi, "Advanced-Ignition-Concept Exploration on OMEGA," 36th EPS Conference on Plasma Physics, Sofia, Bulgaria, 29 June–3 July 2009.

